
Politecnico di Torino

Politecnico di Torino
Energy and Nuclear Engineering

A.A. 2025/2026

Sessione di Laurea Marzo/Aprile 2026

# Optimization of Electric Heating Elements for industrial applications: critical analysis of MoSi2 and exploration of hybrid alternatives.

Supervisors:
Monica Ferraris
Peter Rop

Candidate:
Sebastian Tonzanu

## Abstract

Decarbonizing high-temperature industrial processes through renewable energy integration requires the development of electric heating systems capable of delivering power levels one to two orders of magnitude higher than those currently available. Present high-temperature radiative heaters rely predominantly on molybdenum disilicide ($MoSi_2$) heating elements. These intermetallic compounds are characterized by a unique combination of metal-like electrical conductivity with ceramic-like robustness, enabling operation at surface temperatures up to 1800°C through the formation of a self-healing protective silica ($SiO_2$) layer. However, the transition to multi-megawatt industrial scaling is constrained by the intrinsic physical properties of $MoSi_2$, most notably its relatively low electrical resistivity. To keep the current within acceptable limits, systems must operate at high voltage, demanding heating elements with significantly increased electrical resistance. Increasing the resistance by reducing the cross-sectional area leads to mechanically fragile geometries, unsuitable for large-scale industrial implementation. In fact, $MoSi_2$-based elements suffer from room-temperature brittleness, low fracture toughness, and susceptibility to high-temperature creep and shape instability.

The objective of this thesis is to assess the scalability limits of current $MoSi_2$ technology and to identify potential material alternatives or optimization strategies. The study combines a theoretical analysis of bonding mechanisms, electrical properties and oxidation thermodynamics with a systematic benchmarking of diverse material families. Candidate materials evaluated include alternative intermetallic silicides ($WSi_2$, $NbSi_2$, $TaSi_2$), metallic resistance alloys (NiCr, FeCrAl), carbides and carbon-based materials (SiC, graphite), and ultra-high-temperature ceramics ($ZrB_2$, $HfB_2$). These materials are assessed based on a multi-criteria framework: maximum service temperature, electrical resistivity, temperature coefficient of resistance (TCR), oxidation kinetics, emissivity, and manufacturability.

Based on this evaluative framework, three main improvement routes are investigated: chemical alloying and doping; microstructural control and densification; and surface engineering approaches. Furthermore, the feasibility of novel composite systems is discussed alongside the technological and economic barriers limiting their industrial adoption. The results provide a scientific rationale for why $MoSi_2$ remains the benchmark material despite its limitations, while clearly defining the engineering challenges that must be overcome to realize the next generation high-power electric heaters essential for a carbon-neutral industrial sector.

## Table of Contents

Abstract ..... i

Table of Contents ..... ii

1. Introduction ..... 1

1.1. Renewable high temperature heat in industrial processes and current reliance on fossils and implications for CO2 emissions ..... 1

1.2. Need for electrification and current electric heaters ..... 4

2. Background and literature review ..... 9

2.1. $MoSi_2$ as state-of-the-art material ..... 9

2.2. Commercial examples ..... 15

2.3. Industrial application in a molten salts bed ..... 20

3. Theoretical framework ..... 23

3.1. Hybrid composites: metal-like conductivity vs ceramic-like robustness ..... 23

3.2. Oxydation resistance and pest phenomena ..... 26

3.3. Emissivity considerations ..... 29

4. Alternative materials ..... 32

4.1. Candidate materials families ..... 32

4.1.1. Intermetallic Silicides ..... 33

4.1.2. Metallic Alloys ..... 37

4.1.3 Carbides and Carbon-Based Materials ..... 40

4.1.3. UTHC (Ultra High Temperature Ceramics) ..... 47

4.2. Current commercial alternatives ..... 49

4.3. Comparative analysis with MoSi2 ..... 53

5. Performance improvement of MoSi2 ..... 57

5.1. Alloying / doping ..... 58

5.2. Manufacturing routes ..... 65
5.3. Surface engineering ..... 72
5.4. New compounds and composites without MoSi ..... 73
6. Conclusions ..... 77
6.1. Comparative synthesis and key findings ..... 77
6.2. Limits of the study and recommendations for further research ..... 78
References ..... 80

# 1. Introduction

## 1.1. Renewable high temperature heat in industrial processes and current reliance on fossils and implications for CO2 emissions

The research activity presented in this thesis and its results were carried out within the Product Development R&D Department of NEM Energy b.v., an energy company with an office located in Zoeterwoude, the Netherlands, where the undersigned conducted his internship and related thesis work.

NEM Energy Group stands at the forefront of the power generation sector, specializing in heat transfer technologies designed to maximize efficiency while reducing industrial emissions. Their expertise is consolidated in the development of Heat Recovery Steam Generators (HRSGs), waste heat recovery units, and specialized exhaust systems. Rather than just providing the actual technologies, the group manages the full lifecycle of these systems, from initial engineering and fabrication to long-term aftermarket support. Their activity covers several industrial sectors, including traditional power generation, oil & gas, renewables, as well as the nuclear and geothermal markets.

Central to the energy transition is the advancement of industrial electric heating. As global utilities feel the pressure to hit decarbonization milestones, switching from fossil fuel burners to electric alternatives has become a strategic necessity. By integrating these electric solutions, industries can finally capitalize on the growing availability of renewable power, marking a decisive shift toward a low-carbon operational model. The electric heaters provide an efficient and precise heating solution for both gaseous and liquid media in industrial applications. They are designed to handle process air, inert gases, and exhaust streams, as well as liquids such as water, thermal oils, and specialized process fluids.

As said high-temperature heat processes, such as steel forging and cement production, are essential for modern society and achieving net zero climate targets. However, they currently still rely on the combustion of fossil fuels for high temperatures applications (500-2000°C). As a result, industrial process heat is one of the largest and most persistent sources of $CO_2$ emissions, accounting for approximately 18% of global greenhouse gas emissions. Progress in decarbonizing this sector has been slow: in 2023, only about 12% of industrial heat demand was

supplied by renewable or low-carbon sources, compared to roughly 10% in 2015. Decarbonization relies heavily on electrification, which remains one of the most viable routes to achieving net-zero emissions. By replacing carbon-heavy fossil fuel combustion for low-carbon electricity, industries can cut greenhouse gas output at the source. Beyond the emission cuts, electrified systems are inherently more efficient; they bypass the massive thermal losses that occur when burning fuels, resulting in substantial primary energy savings.

Despite this potential, over the last ten years industrial emissions across the European Union have dipped by a mere 8%, mainly due to energy savings. Over the same period, the share of electricity in industrial final energy consumption has increased only marginally, from 31% in 2000 to 34% in 2021. Currently, just 3% of industrial process heat in the EU is electrified, even though all ambitious global climate mitigation scenarios consistently identify a substantial increase in electricity use as their core strategy. Electrification potential exists across all temperature levels. However, larger but somewhat more difficult to implement electrification potentials in the temperature ranges above 400-500°C, accounting for >40% of total industrial heat demand. [1][3][5][6]

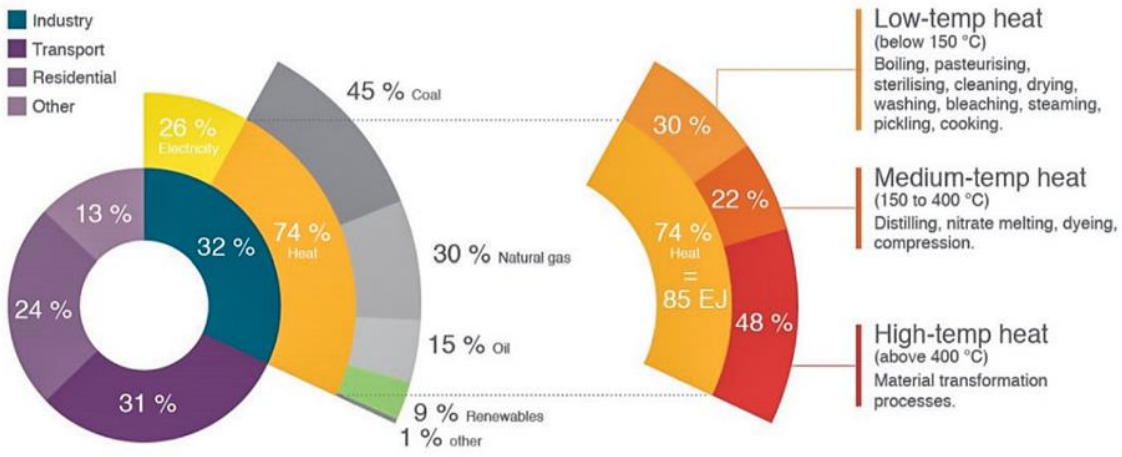


*Figure 1. Industrial heat demand share [2]*

Recent analyses indicate that approximately 78% of industrial process heat could be electrified with existing technologies. When technologies under development are included, this potential rises to over 90%. In the EU27, electrification of suitable industrial processes could reduce carbon dioxide ($CO_2$) emissions by around 117 million tons per year by 2050. Many electric heating solutions are already entering commercial deployment. While significant engineering

R&D and economic challenges remain when scaling up, no fundamental scientific breakthroughs are necessary. Several obstacles stand in the way of this transition, primarily the high cost and limited availability of clean electricity: on average, it's currently twice or even three times as expensive as natural gas. Also grid infrastructure limitations remain a major bottleneck. Expanding both the capacity and coverage of the national grid is prerequisite for lowering costs and extending electrification to more isolated sites, particularly small and medium-sized enterprises (SMEs). At the same time, continued expansion of renewable generation, supported by energy storage and dispatchable clean power, is essential. Remaining gaps and challenges are concentrated on the upper half of the temperature range (especially >1000°C). Low temperature applications up to ~165°C can be electrified relatively easily with mature and market-ready technologies such as heat pumps, electric boilers and district heating. Nevertheless, deployment has remained limited due to unfavorable electricity-to-gas price ratios (as shown in Figure 2), long grid connection lead times and the absence of clear policy frameworks. Supportive policies are only now gaining momentum, but stronger signals are still needed. [1][4][7]

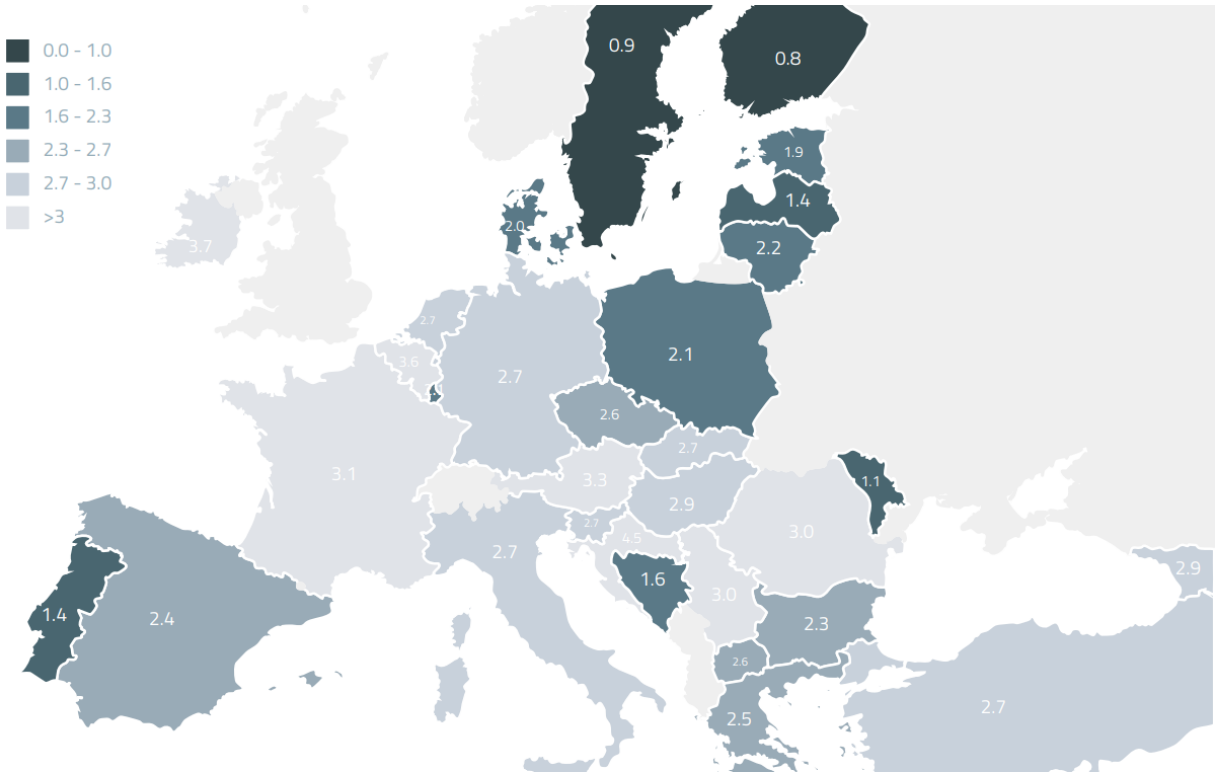


*Figure 2. Ratio of electricity to gas prices, first half of 2023 [1]*

### 1.2. Need for electrification and current electric heaters

Beyond sustainability considerations, the electrification of industrial heating also presents a strong business case.

Electric heating outperforms fossil-based systems in several key areas:

- Up to 90 percent efficiency (already mentioned): unlike combustion-based systems, which suffer from conversion and exhaust losses, electric heating converts electricity directly into heat at the point of use.
- Precise temperature control: electric heaters can maintain stability within ±1°C, improving process control, repeatability, and product quality.
- Reduced maintenance requirements: the absence of combustion residues such as soot or ash results in lower component wear, reduced maintenance needs, and decreased system downtime.
- Elimination of NOx and SOx emissions: electrification improves workplace safety and air quality while ensuring compliance with increasingly stringent environmental regulations.
- Compatibility with digitalization and automation: Electric heating integrates seamlessly with modern control architectures, enabling advanced automation and process optimization through IoT and AI-driven control systems.

It is also important to note that combustion heating typically requires additional auxiliary equipment (ex. heat exchangers, channels for gases collection), which increases system complexity. [8]

Three electric heating principles have been targeted by NEM as the most suitable for industrial process heat applications: resistive heating, inductive heating and radiative heating. These technologies were selected based on criteria such as system size, fluid handling requirements, operating conditions of fluid and technological maturity. A key design challenge is the separation of the electrics from the operating fluid: direct contact with the fluid must be avoided, and electric conductors should not penetrate pressure-retaining components. In addition, large power ratings favor operation at high voltage levels (typically above 10 kV) in order to limit current levels, cable cross sections and transformer sizes. This requires high electrical insulation strength, implying large distances between conductors and ground, as well as the use of suitable insulating supports, such as glass or ceramic materials. [11]

Resistive heating consists in the passage of an electric current through a conducting material, generating heat due to the electrical resistance. The resistance of a conductor is given by the following relation: $R = \rho \frac{l}{A}$

*Table 1. Resistivity value and max. operating temperature of different materials [9]*

| Material | Maximum operating temperature in dry air (°C) | Resistivity ($10^{-12}$ ohm m at 20°C) |
|---|---|---|
| Nickel-based alloys* | | |
| 80 Ni/20 Cr | 1200 | 110 |
| 80 Ni/20 Cr + Al | 1250 | |
| 60 Ni/15 Cr/ 25 Fe | 1100 | 110 |
| 50 Ni/18 Cr/ 32 Fe | 1075 | 110 |
| 37 Ni/18 Cr/ 33 Fe/2 Si | 1050 | |
| 54 Ni/46 Cu | 400 | 49 |
| Iron-based alloys* | | |
| 72 Fe/22 Cr/ 4 Al | 1050 | 139 |
| 72 Fe/22 Cr/ 4 Al + Co | 1375 | 145 |
| Refractory metals | | |
| Platinum | 1400 | 11 |
| Molybdenum | 1750 | 5.7 |
| Tantalum | 2500 | 12.5 |
| Tungsten | 1800 | 5.5 |
| 10% rhodium/ 90% platinum | 1600 | 19.2 |
| 40% rhodium/ 60% platinum | 1750 | 17.4 |
| Non-metals | | |
| Silicon carbide | 1600 | $10^5$ |
| Molybdenum disilicide | Up to 1800 | 40 |
| Graphite | 3000 | $10^3$ |

* Approximate compositions only

The value of resistivity (ρ) varies over about three orders of magnitude (Table 1) even for conductive materials and is strongly temperature dependent, normally increasing with temperature for most metals (but may decrease for non-metallic conductors). The resistivity central role in electric heating will be further discussed later on the next chapters of this thesis. [9]

Resistance heating may be implemented either directly, with the material to be heated itself carrying the current, or indirectly, with heat developed in a separate heating element and transferred to the workpiece receives by conduction, convection and radiation.

NEM focuses on a resistive heating technology in which a high temperature resistive wire is placed inside a tube and embedded in a thermally conductive but electrically insulating material. Current passes through the wire and it's heated up thanks to its resistance; heat is conducted to the tube wall and the process fluid flowing around the tubes is heated indirectly.

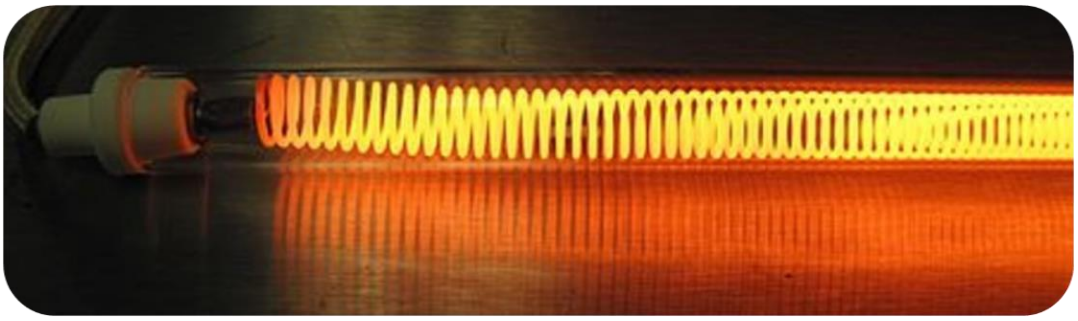

*Figure 3. Resistive heating element picture (NEM property information)*

More characteristics about this solution are:

- Max. operating fluid temperature approximately 700-750°C
- Good for modular set-up with relatively easy replacement
- Lifetime expectancy of elements is moderate
- Heat is transferred from the inside outward, which requires large pressure vessels and penetrations of the elements through pressure part walls, making the design less suitable for high pressure applications
- Max. operating voltage is limited, often necessitating transformers and increased copper usage in cabling
- Highly mature and widely proven for low power applications [11]

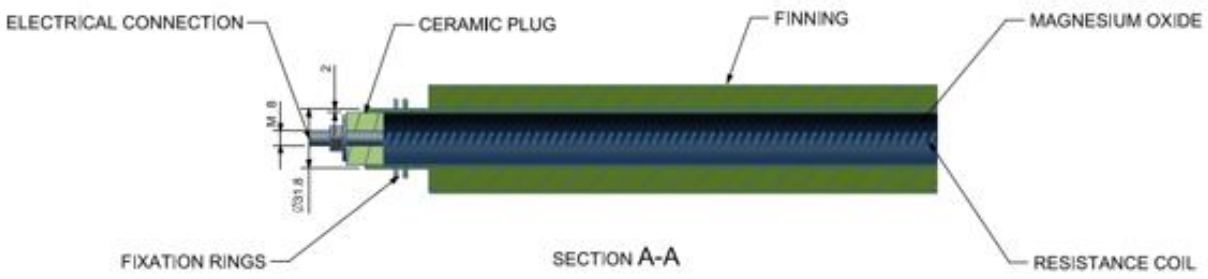


*Figure 4. Resistive heating element section (NEM property information)*

Inductive heating, on the other hand, relies on electromagnetic coupling and is widely and increasingly used for through-heating, heat treatment and melting of metals. An alternating current flowing through an induction coil generates a time varying magnetic field, which induces eddy currents in a nearby conductive workpiece in accordance with Lenz's law. The electrical resistance of the material causes these induced currents to dissipate energy as heat.

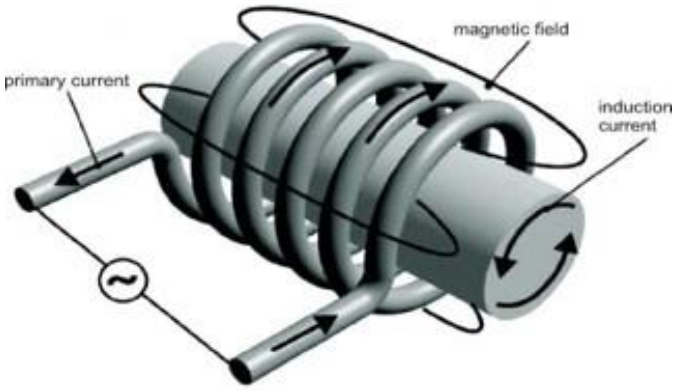


*Figure 5. Inductive heating element scheme (NEM property information)*

In the inductive heating concept developed by NEM, an electric coil is wound around a pipe or tube bundle and AC current in the coil induces eddy currents in the metallic pipe walls, which are then heated and transfer energy to the process fluid.

Some specifics about this technology:

- Max. operating fluid temperature up to 1000°C
- Well suited for high voltage <25 kV, benefiting from established generator and transformer technologies
- Heat is transferred from the outside inward, which simplifies the design
- Modularity is limited due to large specific iron core to generate an intensive magnetic field
- Component lifetime is typically long
- Active cooling of the induction coil is required, leading to additional power losses (i.e. efficiency <100%) and extra CAPEX, even though such cooling solutions are commercially available [11]

The last development vector, radiative heating which represents the focus of this study, is based on thermal radiation governed by the Stefan-Boltzmann law, according to which the radiative heat flux emitted by a body is proportional to the fourth power of the temperature of the body:

$q = \sigma A T^4$

To consider the real nature of the radiant bodies (different from ideal black body behavior), the emitted radiation is reduced by a factor known as emissivity.

In the radiative field, NEM works with high temperature heating elements made of molybdenum disilicide (or silicon carbide), electrically heated till 1700-1800°C, at which they start radiating high power density heat.

These elements, commonly used in glass furnaces and aluminum smelters, are arranged between tube bundles or membrane walls to form a radiative furnace that transfers heat to the process fluid.

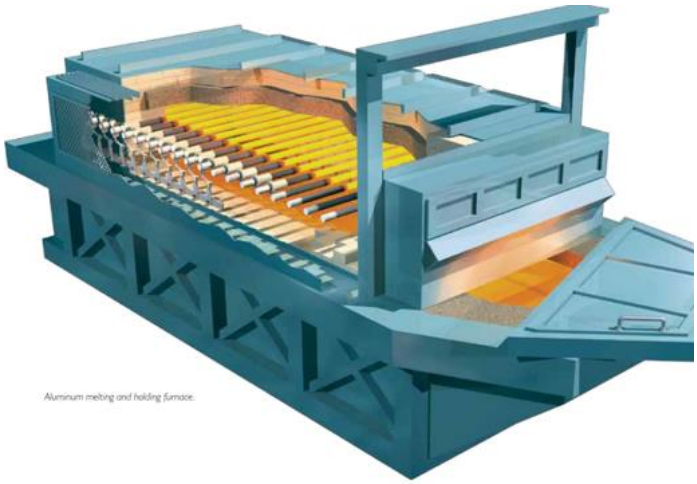


*Figure 6. Radiative heating furnace layout (NEM property information)*

Main characteristics are:

- Max. operating fluid temperature up to 1000°C
- Well suited for high voltage <25 kV
- Radiation allows for larger distances between heating elements and surrounding structures
- Heat is transferred from the outside inward, facilitating tube designs suitable for high pressure operation
- Good for modular set-up with relatively easy replacement
- Lifetime expectancy of elements is moderate
- Less uniform power distribution along the tubes than resistive heating [9][11]

In the following chapters, this technology is examined in detail to clarify why it represents the most viable commercial solution currently available for high temperature applications, why MoSi2 emerges as the most suitable material and why, to date, no market-ready alternative option has proven to offer comparable overall performance.

# 2. Background and literature review

## 2.1. $MoSi_2$ as state-of-the-art material

$MoSi_2$ (molybdenum disilicide) is an intermetallic refractory compound widely employed in high-temperature electric heating applications. In order to understand its performance and limitations, it is necessary to examine the intrinsic physical, chemical and electronic properties of its constituent elements, molybdenum and silicon.

Molybdenum (Mo) is a refractory transition metal belonging to group 6 of the periodic table. Molybdenum is defined by its remarkable thermal resilience, reaching a melting point of 2622°C, a threshold surpassed by very few pure elements. This high temperature stability is complemented by a robust thermal conductivity of approximately 139 W/(mK) at room temperature, making it indispensable in extreme environments. Its unique behavior derives from its electronic structure, specifically the $[Kr]4d^5 5s^1$ configuration. With six valence electrons available for both metallic and partially covalent bonding, the element exhibits a rare chemical flexibility. This allows molybdenum to transition through oxidation states from -4 to +6, a range that explains its immense versatility across various industrial catalysts and complex chemical applications. Electrically, it shows high conductivity (~2 x $10^7$ S/m) and correspondingly low resistivity (~5.34 μΩ·cm @ 20°C). Mechanically, molybdenum presents high strength and toughness, good corrosion resistance but brittle behavior at room temperature. Molybdenum does not occur naturally in the pure metallic form and is primarily obtained from molybdenite ($MoS_2$). It's produced and sold as a grey-black shiny powder and it crystallizes in a body-centered cubic (BCC) structure. It is usually hydrostatically compacted and sintered at high pressure and temperature and used to make alloys. Other uses for molybdenum include catalysts for the petroleum industry, inks for circuit boards, pigments and electrodes. Major mining areas include the USA, China, Chile and Peru, with a global production of about 200,000 tons per year. Market prices typically range from 25 to 150 USD/kg depending on purity and market conditions. From a chemical standpoint, molybdenum is stable in air at room temperature but oxidizes above approximately 600°C, forming volatile oxides such as $MoO_3$. For this reason, its use at high temperature is generally limited to vacuum or non-oxidizing environments. Beyond heating elements, molybdenum and its alloys are employed in radiation shields, forging dies, bearing components, sputtered layers, semiconductor interconnects, catalysts, pigments,

electrodes and so on. It is typically combined with ceramics and glass due to its thermal shock resistance and high melting point. [14][22][23][30]

Silicon (Si) is a tetravalent non-metal, often classified as a metalloid, with electronic configuration $[Ne]3s^2 3p^2$, which allows the formation of up to four covalent bonds and results in a wide range of chemical behaviors. At room temperature it is a solid material with a silvery appearance and bluish reflections on its crystalline faces. Silicon's physical structure is defined by a diamond cubic lattice, a configuration that provides significant hardness but also results in inherent brittleness. With a density of 2.33 $g/cm^3$ and a melting point of 1414°C, it occupies a unique space between structural stability and thermal resilience. From an electrochemical standpoint, silicon functions as a semiconductor with a characteristic band gap of approximately 1.11 eV. While high electrical resistivity (of the order of on the order of $10^4$-$10^5$ Ω·cm) causes high purity silicon to act as an insulator at room temperature, this conductivity scales sharply as temperatures rise. This is balanced by a relatively high thermal conductivity (~150 W/(mK)) and a low coefficient of thermal expansion (~$2.5 \times 10^{-6}$ $K^{-1}$), a combination that ensures the material maintains its dimensional integrity even under rigorous thermal cycling. Chemically, silicon is defined by its strong affinity for oxygen and a versatile range of oxidation states from -4 to +4. This reactivity is its greatest defense: upon atmospheric exposure, it immediately generates a thin, continuous silicon dioxide ($SiO_2$) passivating layer. This natural shield prevents further degradation, keeping the material stable in air up to roughly 900°C. Beyond 1400°C, however, it becomes highly reactive with oxygen, nitrogen, and halogens. Finally, its utility in photonics and energy is cemented by its optical profile. Silicon is remarkably transparent to infrared radiation, transmitting over 95% across a broad spectrum. When paired with its wide absorption range and its compatibility with anti-reflection coatings, these traits make it a suitable material for modern electronic and solar applications. [25][26]

Silicon is rarely found in elemental form in nature; it occurs mainly as silica ($SiO_2$) and silicate minerals. Industrial production of elemental silicon is achieved in electric arc furnaces by carbothermal reduction of silica. In Table 2 are summarized and compared the main properties of the two materials.

The combination of these two elements gives rise to the distinctive properties of $MoSi_2$. Molybdenum disilicide is a refractory intermetallic compound wuth density 6.26 $g \cdot cm^{-3}$ and a high melting point of approximately 2030°C, with a grey metallic appearance. It was first

investigated in 1907 as a high-temperature corrosion-resistant coating for ductile substrates. $MoSi_2$ exists in two polymorphic modifications: a stable α-phase with body- centered tetragonal crystal structure (C11b unit cell) and a metastable β-phase with hexagonal structure. The α-phase is the technologically relevant form. [20][21]

*Table 2. Mo and Si main properties*

| | Density [g·cm⁻³] | Melting point [°C] | Resistivity @ T room [μΩ·cm] | Thermal conductivity @ room T [W/(mK)] | Oxidation resistance in air | Mechanical behavior |
|---|---|---|---|---|---|---|
| **Mo** | 10.28 | 2622 | 5.34 with positive TCR | 139 | Up to 600°C | Ductile but brittle at room T |
| **Si** | 2.33 | 1414 | ~$10^{10}$ with negative TCR | 150 | Up to 900-1400°C | Brittle |

At the atomic scale, the C11b the structure is characterized by a complex coordination environment in which each molybdenum atom is surrounded by ten silicon atoms and four molybdenum atoms, while each silicon atom has five molybdenum and five silicon nearest neighbors (Figure 7a). In the (110) crystallographic planes, silicon atoms form hexagonal, graphite-like sheets with molybdenum atoms located at the centers of the hexagons (Figure 7b). Upon alloying molybdenum with silicon, a redistribution of valence charge occurs between the atoms, leading to the formation of $MoSi_2$ or other intermetallic phases in the Mo-Si system, depending on composition and temperature (Figure 8). This charge transfer or redistribution determines the bonding nature and, consequently, the crystal structure and the mechanical, thermal and electronic properties of the compound. [13][34]

The structural integrity of $MoSi_2$ is rooted in the highly directional and robust interactions between its constituent molybdenum and silicon atoms. At the atomic level, electronic structure mapping reveals a significant p-d hybridization, specifically between the Si 3p and Mo 4d orbitals. This orbital overlap facilitates a bond that is primarily covalent in nature, characterized by only a subtle charge transfer from molybdenum to silicon. Such a balanced electronic distribution is expected, given the remarkably similar Pauling electronegativities of the two

elements (2.16 for Mo vs. 1.90 for Si). Ultimately, it is this specific bonding architecture that provides the material with its exceptional chemical resilience and mechanical endurance when subjected to extreme temperatures. [12][13]

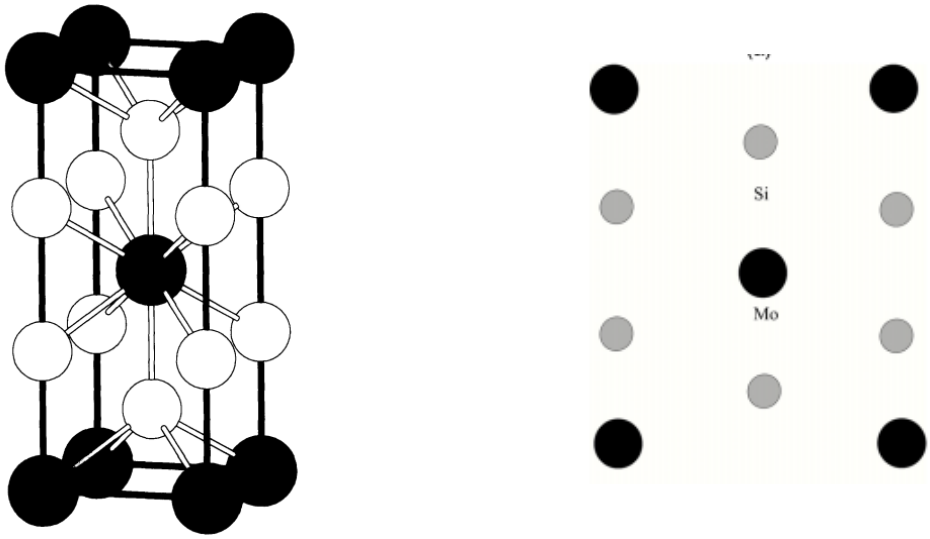


*(a)* *(b)*

*Figure 7. (a) Tetragonal C11b MoSi2 unit cell [12], (b) View of the C11b (110) plane [13]*

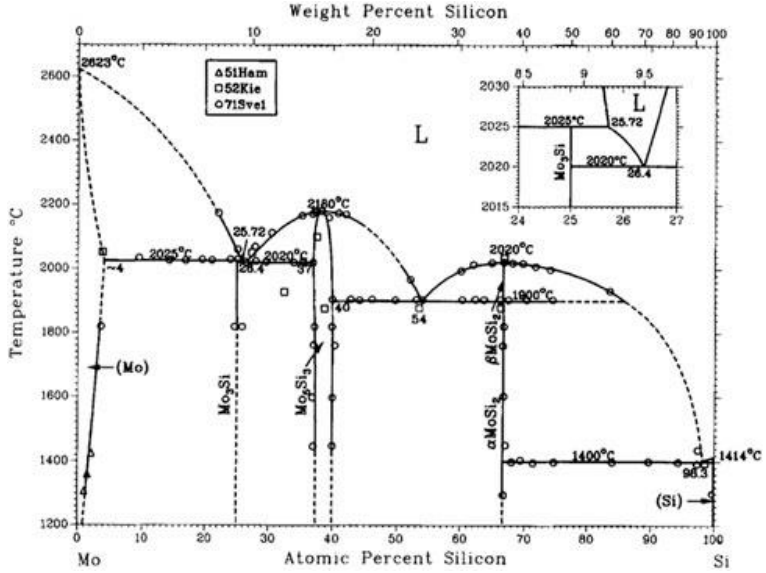


*Figure 8. Mo-Si phase diagram [34]*

$MoSi_2$ exhibits relatively high thermal conductivity of approximately 66 W/(mK) at room temperature. Its electrical resistivity lies in the range 23-27 μΩ·cm at room temperature, corresponding to an electrical conductivity of roughly 2-3 x $10^6$ S/m. These values are lower than pure metals but significantly higher than conventional ceramics, enabling efficient Joule

heating. In contrast to many of the conventional metallic heating elements, $MoSi_2$ is notably resistant to the aging effects that typically degrade resistivity over time. This stability is paired with a relatively low coefficient of thermal expansion, roughly 7-10 x $10^{-6}$ $K^{-1}$ across the 20°C to 1400°C range, which ensures the material retains its dimensional integrity during aggressive thermal cycling. Furthermore, its high emissivity makes it an efficient candidate for radiative heating systems. In oxidizing environments, when pushed to high temperatures, the material naturally develops a thin, adherent $SiO_2$ surface layer. This self-passivating barrier shields the underlying bulk material from further degradation, allowing for sustained operation in air at temperatures exceeding 1500°C. In specialized commercial applications, these elements can even push toward 1800°C without structural failure. Despite these strengths, $MoSi_2$ has its operational drawbacks. While remarkably hard, the material is inherently brittle, particularly below its brittle-to-ductile transition temperature (generally between 1273 K and 1473 K). This lack of fracture toughness and impact resistance makes the elements highly vulnerable to mechanical shocks or accidental mishandling. Furthermore, creep resistance begins to drop sharply once temperatures surpass approximately 1573 K. At these extremes, prolonged exposure can lead to structural sagging or deformation under the element's own weight, necessitating careful support in furnace design. For this reason, $MoSi_2$ heating elements are typically mechanically supported by ceramic plate holders, brackets and saddles, often made of alumina. Large thermal gradients can induce thermal shock failure, which must be considered in furnace design. Although Young's modulus is high and mechanical strength improves at elevated temperature, the low fracture toughness remains a key design constraint. [18][21][31][33]

$MoSi_2$ elements are commonly fabricated through powder-based routes such as conventional sintering, spark plasma sintering, self-propagating high-temperature synthesis and plasma spraying. This processing occurs within controlled, non-oxidizing environments, typically under a hydrogen atmosphere. Thermal cycles generally range from 1000°C to 1500°C during the initial reaction phase, with final densification requiring temperatures as high as 1500-1900°C. A critical challenge in this stage is the high reactivity of $MoSi_2$ in its powdered form. Unlike its bulk counterpart, the powder's high specific surface area and elevated defect density make it prone to oxidation or even ignition at relatively low temperatures. To counteract this, surface modifications, such as $SiO_2$ or $Al_2O_3$ coatings, are applied to suppress low-temperature

degradation. Silica is a particularly favored choice for radiative systems, as its chemical inertness and optical transparency do not interfere with heat transfer. Once stabilized, the powder is typically shaped via cold pressing or extrusion using minimal binders to create a "green body", which then undergoes high-temperature sintering to achieve its final, dense ceramic state. [32][35]

Ultimately, it is this specific intersection of traits, a high melting point and oxidation resistance via $SiO_2$ passivation, balanced by intermediate electrical resistivity and high emissivity, that establishes $MoSi_2$ as a unique material for high-temperature electric and radiative heating technologies. At the same time, its brittleness, creep behavior and processing constraints represent the main technological barriers that must be addressed for large-scale or applications in extreme conditions. Everything will be further discussed in the next chapters.

## 2.2. Commercial examples

Molybdenum disilicide ($MoSi_2$) already constitutes a mature, commercially established technology, supported by a global infrastructure of recognized industrial suppliers. Within the context of this study, various grades of MolyCom®, manufactured by the German supplier SCHUPP (a family-owned enterprise active in the sector since 1996) were evaluated. SCHUPP produces $MoSi_2$ elements under the MolyCom® brand (Figure 9), categorized into two primary technical grades: MolyCom®-Ultra and MolyCom®-Hyper.

*Figure 9. MolyCom® prototype [24]*

The MolyCom®-Ultra grade represents the industrial standard and is available in several variants distinguished by their maximum application temperatures, specifically 1700°C, 1800°C, 1850°C, and 1900°C. In contrast, the MolyCom®-Hyper grade is characterized by ultra-high-purity raw materials with minimized trace element concentrations, tailored for sophisticated applications requiring high chemical cleanliness. Within the Hyper grade category, manufacturers have developed specialized variations to address distinct industrial challenges. One notable example is MolyCom®-Hyper 1800SC (Super Clean), which is specifically engineered for high-purity environments. In the sintering of zirconia, for instance, traditional heating elements can cause unintended discoloration; the SC variant mitigates this risk, ensuring the final ceramic retains its aesthetic and structural purity. Another relevant advancement is the MolyCom®-Hyper 1800AP (Anti-Pest). This grade targets the pest oxidation regime: by enhancing the passivation barrier within this specific window, the AP grade extends the lifespan of elements that must frequently cycle through lower temperatures. [24]

As the technical data in Table 3 illustrates, the main distinction of the Hyper series remains its significantly higher maximum operating ceiling compared to standard grades.

The thermomechanical performance of a heating element is dictated by its geometry, which defines the localization of the high-temperature hot zone and the efficiency of radiative heat flux delivered to the furnace workload. $MoSi_2$ elements are typically engineered in a dual-diameter rod configuration. The central heating zone features a reduced cross-sectional area to increase electrical resistance and promote localized Joule heating. Conversely, the terminals or cold ends possess a larger diameter to minimize electrical resistance and reduce heat generation at the connections, thereby ensuring mechanical robustness and protecting furnace hardware. These cold ends function as integrated busbars, conducting high current to the hot zone while mitigating the risk of overheating the furnace frame or electrical terminal clamps.

*Table 3. MolyCom® -Ultra properties (a), MolyCom® -Hyper properties (b) [24]*

| MATERIAL PROPERTIES OF MOLYCOM®-ULTRA 1700 / -ULTRA 1800 / -ULTRA 1850 / -ULTRA 1900 | | | | |
|---|---|---|---|---|
| | MolyCom®-Ultra 1700 | MolyCom®-Ultra 1800 | MolyCom®-Ultra 1850 | MolyCom®-Ultra 1900 |
| Density | 5.8 kg/dm³ | 5.8 kg/dm³ | ≥ 6.5 kg/dm³ | 7.0 kg/dm³ |
| Bending strength at 20 °C (68 °F) | 350 – 450 N/mm² | 350 – 450 N/mm² | 350 – 450 N/mm² | 360 N/mm² |
| Porosity | < 1 % | < 1 % | < 1 % | < 1 % |
| Max. element temperature (under air) | 1.700 °C (3092 °F) | 1.780 °C (3236 °F) | 1.820 °C (3308 °F) | 1.850 °C (3362 °F) |
| Max. furnace/kiln temperature (under air) | 1.550 °C (2822 °F) | 1.650 °C (3002 °F) | 1.750 °C (3128 °F) | 1.800 °C (3272 °F) |

*(a)*

| MATERIAL PROPERTIES OF MOLYCOM®-HYPER 1800 / -HYPER 1800SC / -HYPER 1800AP / -HYPER 1900 | | | | |
|---|---|---|---|---|
| | MolyCom®-Hyper 1800 | MolyCom®-Hyper 1800SC[1)] | MolyCom®-Hyper 1800AP[2)] | MolyCom®-Hyper 1900 |
| Density | 5.7 kg/dm³ | 5.7 kg/dm³ | 5.7 kg/dm³ | 7,2 kg/dm³ |
| Bending strength at 20 °C (68 °F) | 350 – 450 N/mm² | 350 – 450 N/mm² | 350 – 450 N/mm² | 400 – 500 N/mm² |
| Porosity | < 1 % | < 1 % | < 1 % | < 1 % |
| Max. element temperature (under air) | 1.800 °C (3272 °F) | 1.800 °C (3272 °F) | 1.800 °C (3272 °F) | 1.850 °C (3362 °F) |
| Max. furnace/kiln temperature (under air)* | 1.750 °C (3182 °F) | 1.750 °C (3182 °F) | 1.750 °C (3182 °F) | 1.800 °C (3272 °F) |
| * Depending on furnace size and type. \| [1)]SC - Super Clean / [2)]AP- Anti Pest | | | | |

*(b)*

As illustrated in the U-shaped element in Figure 9, distinct surface finishes and colors are utilized to differentiate the functional zones of the element. The upper part of terminal features a smooth, machined finish to ensure low contact resistance and secure seating for metallic

clamps or contact straps. Conversely, the intermediate sections of the cold ends often exhibit a rougher, as sintered, or coated ceramic surface designed for structural and insulating purposes. These textural differences prevent improper clamping and result from specialized surface treatments or powder compositions optimized for high-temperature oxidation resistance rather than electrical contact. To further optimize connectivity, the contact tips (at the extremities of the element) are frequently metallized with aluminum, facilitating a low-resistance interface for electrical connection via flat braided aluminum straps; that is why these final segments present a rougher light grey surface.

MolyCom® elements are manufactured according to rigorous industry standards in various geometries, including rods and U-, L-, or W-shaped configurations, with custom geometries available for specific furnace architectures (Figure 10).

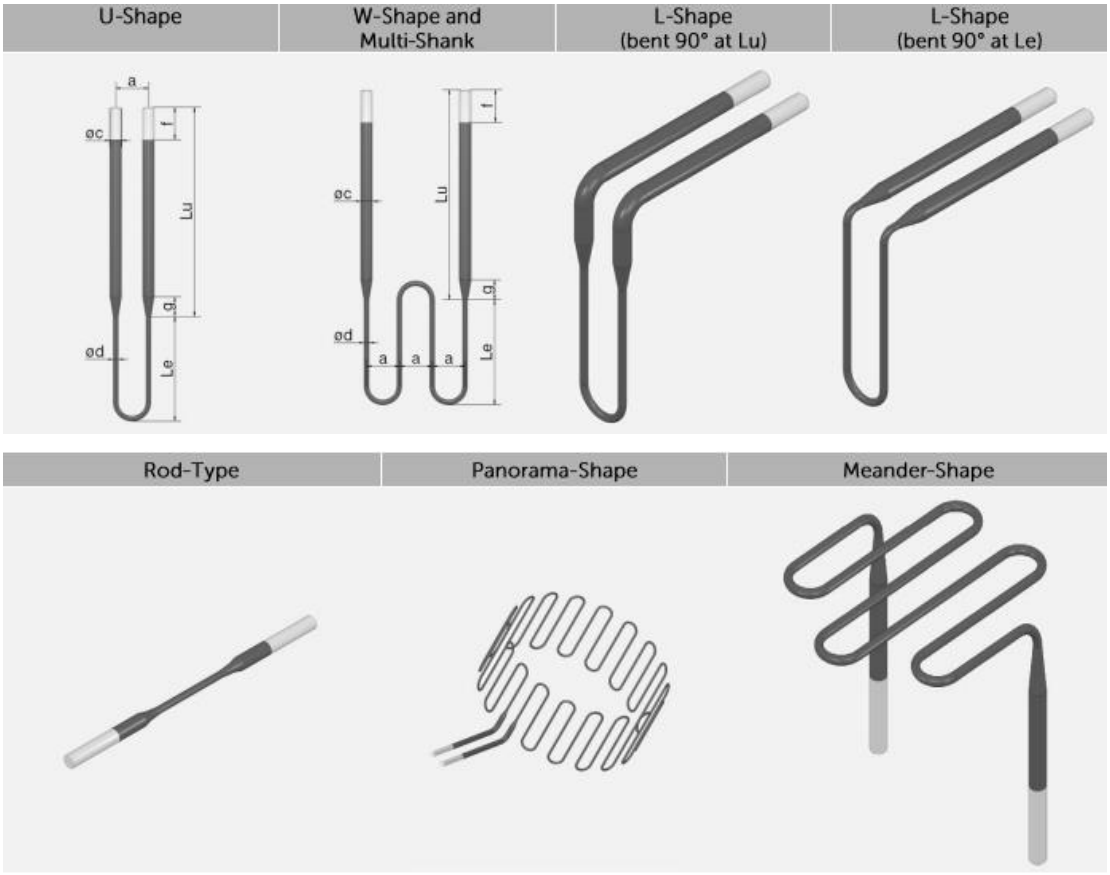


*Figure 10. SCHUPP available types of heating elements [24]*

Standard Hot Zone/Cold End diameter ratios include 3/6, 4/9, 6/12, 9/18, and 12/24 mm, with lenghts spanning 25 mm to 2000 mm. The most prevalent design is the two-shank U-shaped element, where the heating zone is welded to terminals that have a diameter typically double

that of the active section. These elements can be modified with 45° or 90° bends in either the hot zone or the terminals to accommodate specific installation constraints. While various configurations exist, four-shank elements are typically restricted to horizontal mounting. In contrast, bent configurations serve as a necessity when physical constraints, such as roof limitations or restricted heating zone lengths, preclude the use of standard suspended installations.

Beyond basic geometry, the strategic arrangement of these elements into multiple rows allows for a sophisticated level of multi-zone power control, ensuring precise thermal gradients throughout the furnace. The industry's reliance on rod geometries for $MoSi_2$ is not arbitrary; it represents a calculated balance between production feasibility and long-term mechanical reliability. Standard manufacturing techniques, such as extrusion and pressing, are naturally optimized for cylindrical forms. These shapes can be sintered to near theoretical density while maintaining the high degree of straightness required for industrial use. Deviating into complex cross sections or planar shapes introduces significant risk, primarily in the form of warping or cracking during the sintering phase. Furthermore, since $MoSi_2$ is inherently brittle, engineering protocols favor simple geometries to avoid stress concentrators like sharp corners or large, unsupported spans. For example, attempting to form a $MoSi_2$ rod into a tight helix would generate localized stresses and inhibit thermal expansion, likely leading to fracture or detachment at the terminals. From a structural and chemical perspective, the symmetry of a rod ensures that the protective silica $SiO_2$ layer develops as a uniform shell. This results in a benign, axisymmetric loading state, whereas irregular or flat geometries (such as fins or plates) would suffer from non-uniform thickness and localized cooling gradients. These variations can trigger complex stress fields within the $SiO_2$ scale, eventually leading to spallation and material failure. There is also a practical infrastructure barrier: current industrial standards for busbars and furnace feedthroughs are built around rod-shaped terminals. Moving away from this standard would require an expensive update of power connections and sealing systems.

Ultimately, an element's longevity is dictated by its surface load ($W/cm^2$). The predictable surface-to-volume ratio of a round rod allows engineers to establish a clear relationship between diameter, current density, and temperature. By contrast, non-uniform shapes create "hot spots" of high current density and poor radiative view factors at edges. These localized extremes accelerate grain coarsening and lead to premature failure, making the simple rod the most

reliable geometry for high-temperature service. Consequently, complex commercial shapes are essentially assemblies of rod segments connected by large radii of curvature. Truly different forms are technically possible but would require different forming with much higher cost and lower yield, and much more sophisticated support and allowance for oxide scale growth stresses and thermal gradients. [16][24][27][28]

Another prominent industry leader is the Swedish company Kanthal, which has pioneered electric heating technology since 1931. Their $MoSi_2$ product line, Kanthal® Super, encompasses various grades tailored for specific atmospheric conditions and temperature requirements, analogous to the SCHUPP portfolio. The mechanical and physical properties of the primary Kanthal® Super grades are detailed in Table 4.

*Table 4. Mechanical and physical properties of Kanthal® Super [36]*

| | KANTHAL® SUPER ER | KANTHAL® SUPER HT | OTHER KANTHAL® SUPER |
|---|---|---|---|
| Tensile strength at 1550°C (2820°F) | – | 100 MPa ±25% | 100 MPa ±25% |
| Bending strength at 20°C (68°F) | 450 MPa ±10% | 350–400 MPa ±10% | 450 MPa ±10% |
| Compression strength at 20°C (68°F) | 1400–1500 MPa | 1400–1500 MPa | 1400–1500 MPa |
| Fracture toughness, KIC, at 20°C (68°F) | 3–4 $MPam^{1/2}$ | 4 $MPam^{1/2}$ | 3–4 $MPam^{1/2}$ |
| Hardness, HV, at 20°C (68°F) | 9 GPa | 8 GPa | 9 GPa |
| Density | 5.6 g/cm³ 0.20 lb/in³ | 7.0 g/cm³ 0.25 lb/in³ | 6.5 g/cm³ 0.23 lb/in³ |
| Porosity | < 5% | < 1% | < 1% |
| Thermal conductivity<br>20–600°C (68–1110°F)<br>600–1200°C (1110–2190°F) | <br>30 $Wm^{-1} K^{-1}$<br>15 $Wm^{-1} K^{-1}$ | <br>30 $Wm^{-1} K^{-1}$<br>15 $Wm^{-1} K^{-1}$ | <br>30 $Wm^{-1} K^{-1}$<br>15 $Wm^{-1} K^{-1}$ |
| Coefficient of linear expansion | 7–8 × $10^{-6} K^{-1}$ | 7–8 × $10^{-6} K^{-1}$ | 7–8 × $10^{-6} K^{-1}$ |
| Specific heat capacity at 20°C (68°F) | 0.42 kJ $kg^{-1} K^{-1}$ | 0.42 kJ $kg^{-1} K^{-1}$ | 0.42 kJ $kg^{-1} K^{-1}$ |
| Emissivity | 0.75–0.85 | 0.70–0.80 | 0.70–0.80 |

Kanthal® Super elements can be installed in either vertical or horizontal orientations. While typically positioned along sidewalls, wide furnace architectures may require elements to be distributed across the furnace width or across multiple vertical levels to meet power requirements. In low-profile furnaces where roof-mounted suspension is impractical, horizontal installation may be the most efficient solution. However, it introduces a significant mechanical challenge (anticipated before): $MoSi_2$ begins to soften once temperatures climb past 1200°C. Without adequate support, the elements are prone to sagging or permanent deformation. However, adding physical support is not a simple fix, as it introduces a new ceiling at the maximum operating temperature. This limit is often dictated by the chemical compatibility between the element's protective silica layer and the underlying support structure. A primary concern during thermal cycling is the risk of adhesion. If the silica scale bonds with standard refractory bricks, the resulting sticking effect can lead to catastrophic fractures as the materials

expand and contract at different rates. To avoid this chemical bonding, alumina supports are the industry standard; it serves as an excellent electrical insulator and a chemically compatible mechanical support, maintaining the structural alignment of the $MoSi_2$ rod while preventing vibration-induced damage or bending. [36]

### 2.3. Industrial application in a molten salts bed

To evaluate the technical feasibility of $MoSi_2$ heating elements for multi-megawatt industrial applications, a reference configuration developed by NEM Energy was analyzed. The system is designed for high-temperature Power-to-Heat (P2H) conversion, utilizing a triaxial concentric arrangement to facilitate efficient radiative heat transfer while ensuring structural integrity.

The core of the assembly consists of Kanthal-type $MoSi_2$ refractory rods, characterized by their exceptional oxidation resistance and high-temperature emissivity. Each rod, possessing a diameter of 20 mm and an active length of 2 m, is encapsulated within a secondary protective tube composed of Aluminum Nitride (AlN). AlN was selected for its high thermal conductivity and dielectric strength, providing an initial barrier against chemical interaction. This assembly is further enclosed in a tertiary metallic sheath made of Incoloy 825 (I825), an austenitic nickel-chromium alloy chosen for its superior corrosion resistance in molten salt environments (Figure 11). The AlN tube features an inner diameter of 23.6 mm with a 3 mm wall thickness, while the external I825 tube has an outer diameter of 34 mm and a 1.2 mm thickness.

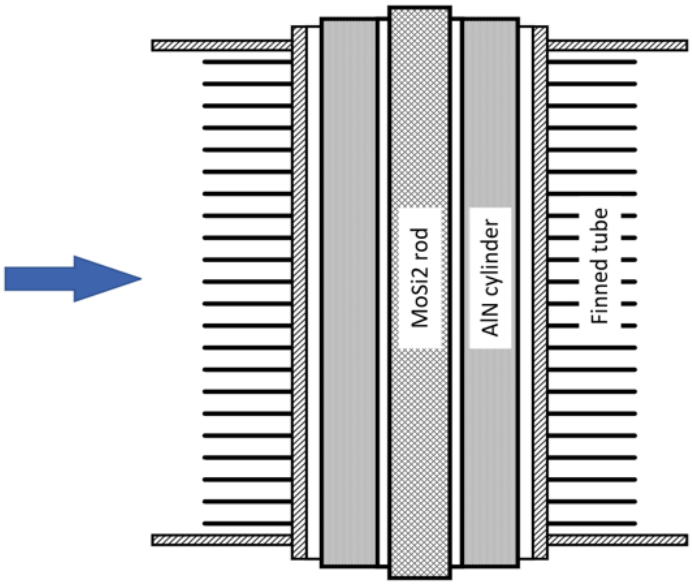


*Figure 11. System's scheme (NEM property information)*

The industrial scale of the system is achieved through a modular electrical architecture. The plant is divided into four primary sections, each containing an array of 24 heating elements (four rods, each associated with six tubes in a specific cluster arrangement). To optimize the electrical load and minimize Joule losses in the supply lines, the system employs a balanced three-phase scheme. Within each section, heating elements of the same phase are connected in parallel, while the sections are interconnected in series. This topology yields a total installed electric capacity of 3.1 MW at a target operating voltage of 15.75 kV. The boundary conditions for the thermal analysis were defined by a fixed rod surface temperature of 1800 °C, corresponding to a nominal heat flux of 256 kW/m².

The thermal performance was evaluated using a steady-state, one-dimensional radial model. Heat transfer within the solid domains (AlN and I825) was governed by Fourier's Law in cylindrical coordinates, utilizing the logarithmic formulation for thermal resistance. Temperature-dependent thermal conductivity λ(T) was integrated where data permitted.

The dominant heat transfer mechanism is surface-to-surface radiation across the annular gaps. The surfaces were modeled as grey and diffuse, and the exchange was solved using the Radiosity Method. This allowed for the simultaneous accounting of Stefan-Boltzmann emission and inter-surface reflections, effectively coupling the temperature-dependent radiative fluxes with the radial conductive resistance of the ceramic and metallic layers. Inside the concentric structure, view factors ($F_{ij}$) were simplified based on the enclosure theory for long cylinders. The $MoSi_2$ rod radiates directly to the inner AlN surface; subsequently, the outer AlN surface radiates to the inner I825 wall.

The external boundary condition involves a complex radiative exchange between the I825 sheath and a heterogeneous environment consisting of a molten salt bath (Solar Salt SAND2001-2100) and T321H stainless steel finned tubes, which serve as the heat extraction interface for the secondary process. This external environment was simplified into two equivalent radiating surfaces with assigned view factors to partition the energy flux between the thermal storage medium (the salt) and the heat exchanger. The resulting system of coupled non-linear equations was solved iteratively using a Newton-Raphson approach until the energy balance residuals at each interface reached convergence.

The model yields a coherent temperature gradient across the multi-layer assembly, revealing the thermal bottlenecks of the design. From the source temperature of 1800 °C at the $MoSi_2$ rod, the

temperature decreases to 1440.7 °C at the AlN inner interface and 1417.2 °C at its outer boundary. The relatively small ΔT across the AlN layer confirms the effectiveness of its high thermal conductivity.

Conversely, a significant temperature drop is observed between the ceramic and metallic stages, resulting in an I825 inner surface temperature of 356 °C and an outer surface temperature of 344.4 °C. This steep gradient is critical, as it ensures the Incoloy 825 structural component operates within a temperature regime where its mechanical properties and corrosion resistance are maximized. In terms of power density, the system achieves a total output of 3087 kW, with a per-tube dissipation of 32.16 kW, demonstrating the feasibility of high-flux radiative heating for large-scale molten salt applications.

This configuration represents a sophisticated approach to the electrification of industrial heat. By decoupling the high-temperature radiant source from the corrosive molten salt through a multi-barrier sheath, the system combines the high-grade heat potential of $MoSi_2$ with the massive thermal energy storage (TES) capacity of nitrates. Such systems are pivotal for the integration of Concentrated Solar Power (CSP) or for Power-to-Heat-to-Storage schemes, providing a scalable solution for decarbonizing heavy industries that require continuous, high-temperature thermal loads.

# 3. Theoretical framework

## 3.1. Hybrid composites: metal-like conductivity vs ceramic-like robustness

As established in the preceding sections, the design of high-performance electric heating elements necessitates a confluence of material properties that are often mutually exclusive in monolithic substances. Identifying an ideal candidate for high-temperature heating is a significant engineering challenge. The performance criteria are so varied that a single chemical element rarely suffices; instead, intermetallic compounds or composite materials should be considered. $MoSi_2$ is a prime example of this hybrid approach, successfully bridging the gap between the conductivity of metals and the thermal resilience of ceramics. To be viable for industrial electric heating, a material must balance several competing technical attributes:

- Optimal electrical resistivity: the material needs a high enough electrical resistivity to allow for compact element designs with manageable cross sections.
- Thermo-Mechanical integrity: it must retain its structural strength and avoid excessive brittleness at peak service temperatures to prevent mid-cycle failure.
- Electrical stability: a low Temperature Coefficient of Resistance (TCR) is vital. If resistivity fluctuates too wildly between room temperature and the operating ceiling, maintaining a stable electrical load becomes nearly impossible.
- Self-passivating chemistry: superior oxidation kinetics are essential. The material must be capable of forming a stable, protective oxide skin during standard operation to prevent rapid bulk degradation.
- Industrial scalability and processability: regardless of its laboratory performance, the substance must be prone to common fabrication processes, allowing it to be shaped into the diverse geometries required by modern furnace architectures.

Consequently, the selection matrix for radiative heating is remarkably narrow. The field is limited to a specific subset of refractory metals, advanced ceramics, and specialized composites that possess both high melting points and the ability to self-heal via protective scales. Ultimately, the final choice is a complex trade-off between the operating atmosphere (vacuum vs. air), peak temperature demands, and the cold hard reality of cost-effectiveness.

$MoSi_2$ stands as the preeminent material in this field because it satisfies nearly all the mentioned criteria. However, its dual nature also imposes certain scaling limitations. Its metallic-like electronic conduction results in relatively low intrinsic resistivity, which complicates high-power applications; to handle large electrical loads while limiting current, the operating voltage must be increased, a requirement that is directly hindered by the material's low resistance. Furthermore, it is characterized by significant brittleness at room temperature, necessitating high precision and care during handling and installation. It was observed that the commercial heating elements can fracture and break just by being dropped from a height of less than one meter (Figure 12).

*Figure 12. Broken MoSi2 sample*

The electrical resistivity of $MoSi_2$ remains notably stable over its operational lifecycle and demonstrates a linear correlation with temperature. It exhibits a positive TCR, with resistivity values increasing by a factor of approximately ten between 20°C and 1800°C (as illustrated in Figure 13).

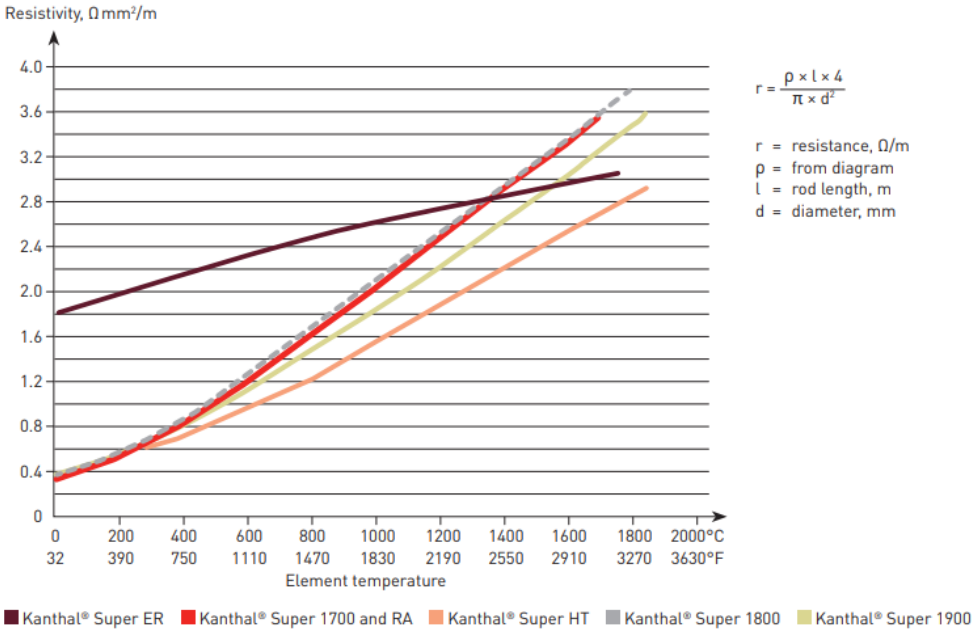


*Figure 13. Temperature dependence of Kanthal Super resistivity [36]*

This resistive behavior is sensitive to several extrinsic factors, including the synthesis methodology, the degree of densification, and the resultant grain morphology. The synthesis route determines phase purity and the presence of secondary phases (such as $Mo_5Si_3$, elemental Si or Mo), as well as defect density, all of which serve as scattering centers that modify carrier concentration. Beyond basic chemistry, the specific fabrication route deeply influences the electrical performance of a material by altering its grain boundary density, crystallographic texture, and internal stress state. These microstructural features are the primary governors of electron mobility. For instance, any deficiency in the densification process, such as residual porosity or micro-cracking, creates bottlenecks and scattering sites within the current path. From a macroscopic perspective, high porosity effectively shrinks the available cross-sectional area for conduction. This results in an apparent rise in measured resistivity, even if the grains themselves remain intrinsically conductive. To avoid this, industrial standards typically mandate a densification target of at least 95-98% of the theoretical density. Falling below this threshold, under-densified elements suffer from unpredictable electrical resistance and extreme mechanical fragility. Finally, grain size determines the volume fraction of grain boundaries. A finer, more fragmented grain structure increases the frequency of boundary scattering. This effect is particularly pronounced if the boundaries are structurally disordered or harbor chemical

contaminants, both of which can significantly raise resistivity and complicate the thermal management of the furnace.

### 3.2. Oxydation resistance and pest phenomena

It is well-established that $MoSi_2$ exhibits superlative oxidation resistance at elevated temperatures due to the formation of a passivating, thin silica ($SiO_2$) layer. However, the material is susceptible to accelerated oxidation at lower temperatures, specifically around 773 K. This phenomenon, identified by Fitzer in 1955, is termed "pest oxidation." There is a general scientific consensus that the pesting of $MoSi_2$ at these intermediate temperatures is intrinsically linked to the formation of volatile and voluminous molybdenum trioxide ($MoO_3$). From a purely thermodynamic standpoint, $SiO_2$ is significantly more stable than either $MoO_2$ or $MoO_3$. Under ideal equilibrium, this hierarchy suggests that molybdenum oxides remain absent until the alloy's silicon reservoir is completely exhausted, a relationship that is true regardless of the operating temperature. This favorable thermodynamic condition is precisely why $MoSi_2$ is so effective at high temperatures; it essentially prioritizes the growth of a protective silica scale over volatile metal oxides. The transition occurs through a phased partitioning of the material. Upon initial oxygen exposure, silicon is drawn from the $MoSi_2$ matrix to produce $SiO_2$, leaving behind a $Mo_5Si_3$ sub-layer. As oxidation continues, silicon is further taken from this intermediate phase, yielding more silica alongside the volatile $Mo_3Si$ phase, eventually terminating in a molybdenum solid solution. However, the pest oxidation, driven by the rapid formation of $MoO_3$, is not thermodynamically preferred so its cause is found in kinetic limitations. Below 600°C, the diffusion coefficients for both molybdenum and silicon within the lattice are essentially negligible. At these lower temperatures, the material cannot maintain the necessary silicon flux to build a continuous, protective silica barrier, allowing the more aggressive (though less stable) molybdenum oxides to dominate the surface reaction. This kinetic limitation results in the simultaneous co-oxidation of silicon and molybdenum, producing a mixed-oxide scale. The formation of molybdenum oxides induces structural failure due to significant molar volume expansion, which ruptures the scale and accelerates further oxidation.

Analyzing the kinetics in greater detail, an effective diffusion length can be defined as:

$$L_D = \left(D\frac{\alpha}{\nu}\right)^{1/2}$$

If $L_D$> $\alpha_0$, where $\alpha_0$ represents the nearest-neighbor distance between silicon and molybdenum atoms in $MoSi_2$, silicon atoms cannot migrate to the oxide/$MoSi_2$ interface at a rate sufficient to sustain silica formation, nor can molybdenum atoms diffuse away from the interface to avoid oxidation. This results in the production of a mixed silica and molybdenum oxide scale. On the other hand, when $L_D$>> $\alpha_0$, the formation of a continuous, protective silica layer becomes possible, shielding the $MoSi_2$ from further degradation.

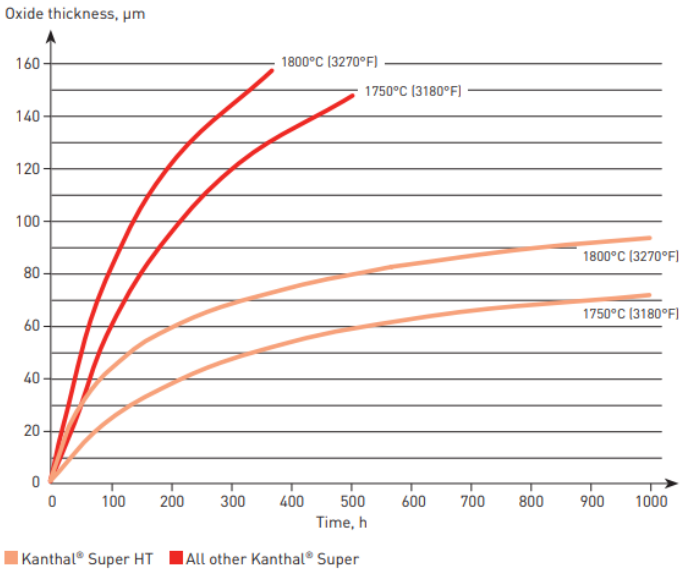


*Figure 14. Kanthal® Super oxidation rate [36]*

$L_D$ is also a function of the oxidation rate, which has been empirically determined to be on the order of $10^{-9}$-$10^{-10}$ m/s within the pest temperature range. As temperatures increase, the material transitions to a parabolic growth rate, with oxidation speeds dropping to remarkably low levels near $10^{-12}$ m/s [18]. This decelerating trend is a characteristic of high-performance silicides. A practical illustration of this behavior is captured in the Kanthal® technical documentation, which contrasts the oxidation thickness of the Super HT grade against its counterparts in the Super series (see Figure 14).It is important to note, however, that while the oxidizing environment and specific synthesis methods heavily influence these rates, they do not tell the full story. The oxidation resistance of a heating element is a multi-faceted characteristic; a low growth rate is a prerequisite, but it must be paired with mechanical adhesion and chemical stability of the scale to ensure long-term survivability in industrial service.

A critical role is played by the operating temperature, which dictates the presence of a protective oxide layer and its growth kinetics over time. By considering reported oxidation rates at various temperatures, the effective diffusion length $L_D$can be estimated as a function of temperature (as shown in Figure 15).

The data indicates that the oxidation behavior of $MoSi_2$ can be categorized into three distinct temperature regimes relative to $\alpha_0$: (I)T < 783 K; (II) 873 < T1273 K; (III) T > 1273 K. Within

Regime (I), the effective bulk diffusion length falls significantly short of the critical threshold $\alpha_0$. At these lower temperatures, the mobility of both molybdenum and silicon atoms is severely restricted. Once the initial silicon reservoir at the oxide/silicide interface is exhausted, the $MoSi_2$ matrix is unable to replenish the supply at a rate sufficient to maintain a pure silica scale. The consequence of this supply-chain failure is the development of the mixed oxides. The localized swelling caused by $MoO_3$ essentially break the oxide layer from within, causing it to rupture and flake away. This mechanical breakdown creates a feedback loop of fresh surface exposure, rapidly accelerating the pest phenomenon and leading to the total structural disintegration of the material. Grain boundary diffusion also contributes significantly to pesting in this regime, as the effective grain boundary diffusion length exceeds $\alpha_0$ (regime (I)).

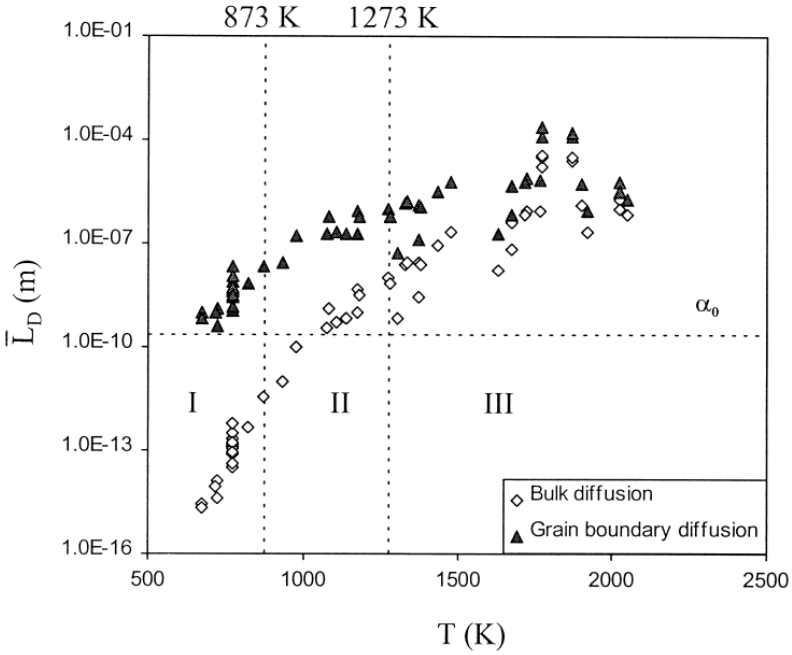


*Figure 15. Effective diffusion length of MoSi2 at different temperatures [18]*

Given that $MoSi_2$ oxidation is governed by nucleation and growth, with the silica growth rate limited by silicon diffusion, the low bulk diffusion coefficient makes transport along surfaces and grain boundaries critical. This explains the preferential oxidation of grain boundaries during pesting. In regime (II), the effective bulk diffusion length is of the same order of magnitude as $\alpha_0$. The transition from non-protective to protective oxidation occurs in this interval; the formation of $SiO_2$ amorphous layers has been linked to the increased volatility of MoO3 as it approaches its melting point of 795°C. In regime (III), the effective bulk diffusion length is

clearly greater than $\alpha_0$, allowing for the formation of a continuous, passivating silica layer that protects the $MoSi_2$ matrix from further oxidation [18][29][33].

When the pest phenomenon is avoided at the operating temperatures required for electric heating, $MoSi_2$ demonstrates exceptional oxidation resistance in air, a performance level that is difficult to replicate with other commercial alternatives.

### 3.3. Emissivity considerations

Within the suite of thermophysical properties governing the performance of molybdenum disilicide, emissivity ($\varepsilon$) is of paramount importance due to its decisive role in radiative heat transfer. Consequently, high-fidelity emissivity data are fundamental for the accurate thermal modeling, design, and operational evaluation of $MoSi_2$-based heating elements.

In their standard operational regime, $MoSi_2$ heating elements function as high-emissivity radiators, closely approximating "gray body" or "near black" behavior. The exceptional radiative efficiency of these elements is strongly related to the silica-rich scale. In the context of industrial furnace design, commercial $MoSi_2$ elements typically maintain a total hemispherical emissivity between 0.70 and 0.85 across a broad temperature range of 800°C to 1700°C.The practical importance of this value is grounded in the Stefan-Boltzmann law, where the radiative heat flux scales proportionally to $\varepsilon T^4$. Consequently, emissivity acts as a main control for power dissipation; it determines exactly how much energy an element can shed at a given surface temperature. Visually, the $SiO_2$ passivation layer gives the element a characteristically matte, gray finish. Beyond its protective role, this oxide scale is partially transparent to thermal radiation. This transparency allows a substantial portion of the infrared energy generated by the underlying $MoSi_2$ substrate to pass through the surface film rather than being trapped or reflected, maximizing the effective heat output of the system. This optical coupling between the substrate exitance and the oxide layer results in a marked increase in both spectral absorptivity and emissivity compared to a pure, bare metallic surface [19].

Consequently, the emissivity of $MoSi_2$ is not a static material constant but is a dynamic function of the following parameters:

- The thickness of the $SiO_2$ scale, which dictates the optical path length and interference effects.
- The structural morphology, including phase crystallinity and density.

- The chromaticity/color, which reflects the spectral absorption characteristics of the surface.

Because of these variables, $MoSi_2$ emissivity cannot be reduced to a single fixed value. Its dependence on temperature is illustrated in Figure 16.

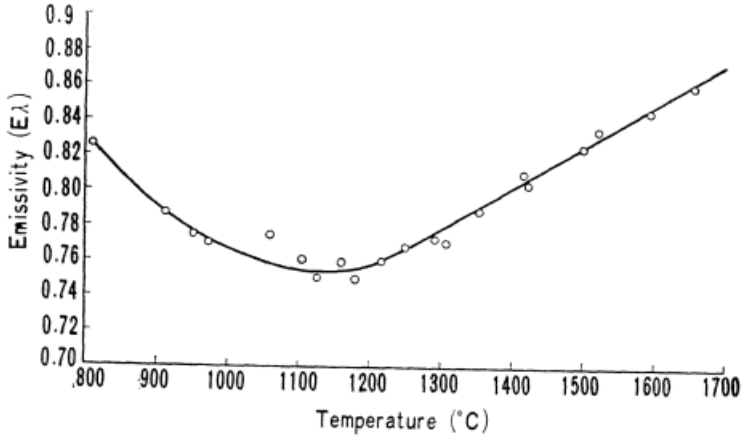


*Figure 16. MoSi2 spectral emissivity measured at 0.65 μm in function of temperature [19]*

Generally, a thin and uniform oxide film ensures a stable emissivity profile. In contrast, the development of a thick, glassy, or heterogeneous layer can lead to unpredictable radiative behavior. Furthermore, emissivity is subject to temporal evolution as the oxide scale thickens during service. At extreme temperatures (exceeding 1700-1800°C), the active volatilization of silica occurs; this not only compromises the material's oxidation resistance but also triggers a degradation in emissivity as the surface layer recedes.

Material macroscopic emissivity is not just a function of its chemistry; it is heavily influenced by its surface topography. As an element's surface becomes increasingly rough, it develops a complex distribution of micro-cavities and valleys. These features act as traps for thermal radiation, suppressing mirror-like reflectivity in favor of diffuse absorption through internal re-radiation. Beyond these internal reflections, high surface roughness effectively expands the total surface area available for emission. This is why aged heating elements often outperform their pristine counterparts in terms of radiative efficiency. While a brand-new element has a smooth, controlled finish, the surface degradation that occur during thousands of hours of service

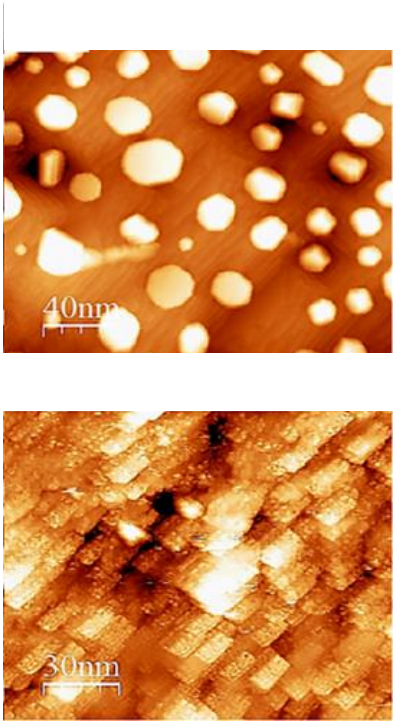


*Figure 17. STEM image of MoSi2 oxidation [29]*

actually serve to boost the emissivity value, allowing the older element to shed heat more effectively than when it was first installed.

Figure 17 provides an illustrative example via Scanning Transmission Electron Microscopy (STEM) images of nanoscale $MoSi_2$ crystallites synthesized via molybdenum deposition on a Si(001)-(2x1) substrate. The images compare the morphology pre- and post-oxidation after exposure to 10 L of $O_2$ at 750°C. The transition clearly demonstrates the proliferation of surface roughness and the growth of micro-cavities following the formation of the oxide layer [29].

In light of the physical mechanisms, $MoSi_2$ elements exhibit superior overall emissivity characteristics, maintaining radiative performance levels that exceed those of most standard refractory oxides (as shown in Figure 18).

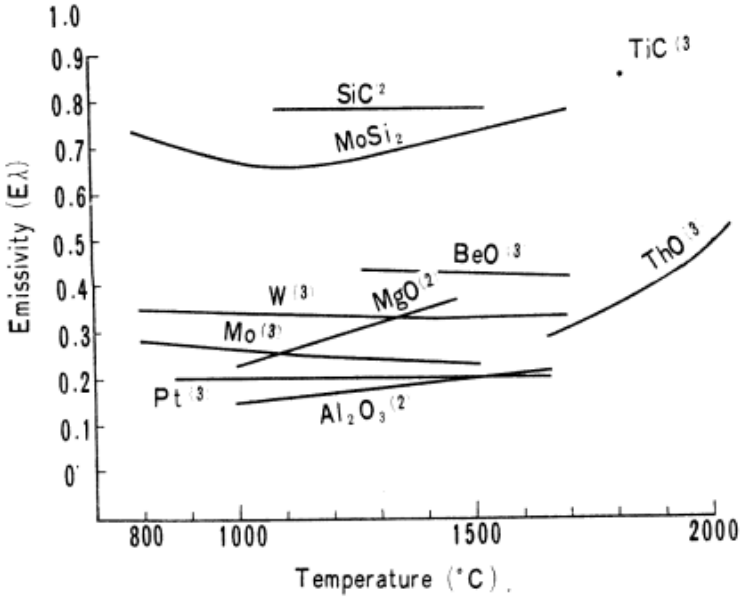


*Figure 18. Spectral emissivity of different materials at 0.65 μm [19]*

# 4. Alternative materials

## 4.1. Candidate materials families

The primary focus of this study, prior to investigating novel alternatives or enhancement strategies for molybdenum disilicide ($MoSi_2$), involved a systematic review of materials currently employed in electric high-temperature heating applications, as well as those whose intrinsic properties suggest functional suitability for such extreme environments. This evaluation facilitated the selection of $MoSi_2$ alternatives, establishing a robust framework for identifying materials capable of advancing current heating technologies.

The selection of candidate materials was governed by the following technical criteria:

- Maximum service temperature: materials must maintain structural and chemical integrity during safe operation above 1200°C, with an ideal threshold ranging between 1600°C and 1800°C.
- Electrical resistivity: at room temperature, candidate's electrical resistivity should ideally match or exceed the standard set by $MoSi_2$ (23-27 $\mu\Omega\cdot cm$). This ensures the material can generate sufficient heat without requiring impractical, oversized cross-sections in the element design.
- Oxidation resistance and chemical compatibility: high temperature stability is not just about melting points, but it requires absolute chemical inertness. The candidate must be capable of forming a stable, self-healing oxide barrier to prevent rapid degradation when exposed to ambient air or aggressive process atmospheres.
- Thermomechanical stability: the material must survive the thermal shock of rapid cycling and steep temperature gradients. Beyond immediate strength, creep resistance is a critical long-term requirement; without it, the heating elements would slowly deform under their own weight at peak service temperatures.
- Spectral emissivity: high spectral emissivity is essential for effective heat transfer. A material that cannot efficiently shed its energy via radiation will struggle to maintain the necessary power density required for industrial furnace operations.
- Scalability and production: finally, the material's laboratory performance must translate to the industrial level. It must be compatible with scalable manufacturing routes, such as

extrusion or advanced sintering, to ensure that complex furnace geometries can be produced reliably and cost-effectively.

Few material classes satisfy this rigorous set of requirements. Consequently, the scope of viable candidates is restricted to the following families: intermetallic silicides (analogous to $MoSi_2$), refractory metallic alloys, carbon-based materials and carbides, and Ultra-High Temperature Ceramics (UHTCs).

### 4.1.1. Intermetallic Silicides

As molybdenum disilicide belongs to the silicide family, this group represents the primary candidates for alternative heating element materials. Specifically, $WSi_2$, $NbSi_2$, and $TaSi_2$, exhibit physiochemical properties analogous to $MoSi_2$. These transition metal silicides are characterized by strong interatomic bonding between the refractory metal and silicon. Tungsten (W), Niobium (Nb), and Tantalum (Ta) are viable substitutes for Molybdenum due to their high-temperature compatibility and similar electronic configurations; being proximally located in the periodic table, these elements possess partially filled d-orbitals, resulting in comparable silicide crystal structures (e.g., *C40*, *C11b*, *C49*, and *C59) [40][50][55].*

Elemental tungsten shares with molybdenum a similar profile of thermal and electrical traits but can push the physical limits further. It reaches the highest melting point of any metal (3410°C), a high density of 19.3 $g/cm^3$, and a room-temperature thermal conductivity (173 W/mK) that leads the refractory group. However, tungsten is notoriously less ductile than molybdenum, which complicates the fabrication of complex element shapes. It is also highly sensitive to recrystallization-driven embrittlement and thermal shock, vulnerabilities that mirror those of molybdenum but are often more pronounced. The most restrictive barrier for pure tungsten is its poor oxidation resistance. In aerobic environments, degradation begins as low as 500°C and turns catastrophic by 1200°C. Consequently, its use is strictly confined to vacuum or inert atmospheres, where it can reliably reach service temperatures near 2500°C. Its electrical resistivity (5.5 $\mu\Omega\cdot$cm at 20°C) is nearly identical to that of molybdenum, making it an electrical substitute in non-oxidizing settings [37][38][48][51][52].

Its silicide $WSi_2$ is an emerging material currently favored for coatings and additives, though it has yet to reach the industrial maturity of $MoSi_2$ for standalone heating elements. The W-Si bond is fundamentally similar to the Mo-Si one, characterized by a hybrid metallic-covalent nature born from the overlap of W-d and Si-p orbitals. While $WSi_2$ offers slightly lower resistivity, its

higher density (9.3 g/cm³) forces a redesign of element geometry. To maintain mechanical stability and appropriate current densities, engineers must often resort to thicker or shorter cross-sections, which can limit the flexibility of furnace architectures.

The oxidation behavior of $WSi_2$ (detailed in Figure 19) is highly temperature-sensitive and it's defined by three distinct stages:

- 773-1273 K: mass gain scales with temperature, reaching a peak at the upper limit.
- 1273-1473 K: the material undergoes significant mass loss as tungsten oxide ($WO_3$) begins to sublime.
- Above 1573 K: mass change stabilizes. At these extremes, the high vapor pressure of $WO_3$ causes it to evaporate entirely from the scale, leaving behind a purified, protective $SiO_2$ layer. Notably, $WSi_2$ suffers from a broader pest oxidation window than $MoSi_2$. This necessitates a more aggressive thermal ramping strategy to skip this critical zone and prevent the element from disintegrating before it can establish its protective silica shell [42][45][57].

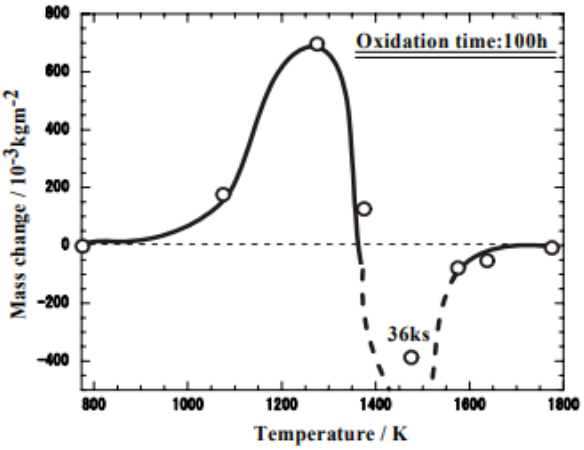


*(a)*

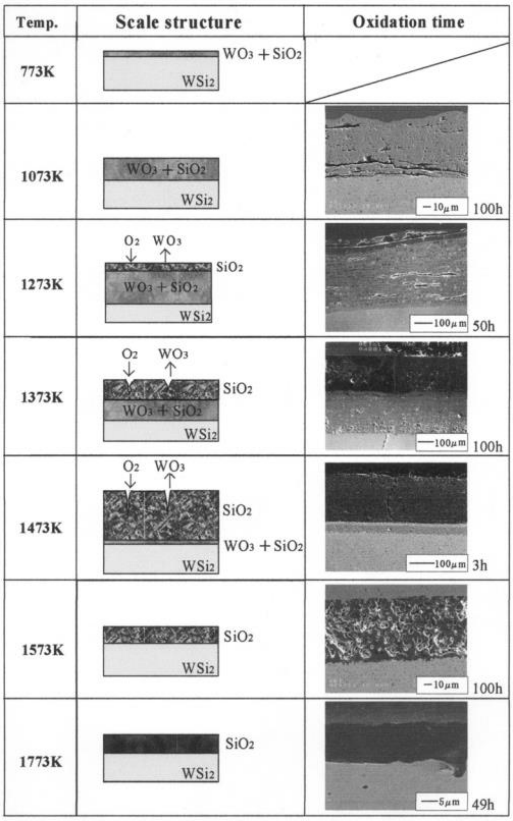


*(b)*

*Figure 19. Oxidation kinetics of WSi2 in air (a), Structure of scales formed on WSi2 (b) [57]*

Niobium is characterized by a lower density (~ 8.57 g/cm³) and moderate thermal conductivity (~ 54 W/(mK) at RT). Its resistivity (~ 15-17 μΩ·cm at RT) is higher than that of molybdenum, but it undergoes rapid oxidation in air, leading to severe spallation and embrittlement. $NbSi_2$ crystallizes in the hexagonal *C40* structure (Figure 20), with a band gap near the Fermi level and properties dictated by Nb-4d and Si-3p orbital interactions. It features a lower density (5.62 g/cm³) and a melting point of approximately 1950°C. The elastic moduli (bulk, shear, and Young's) of $NbSi_2$ are lower than those of $MoSi_2$ and $WSi_2$, indicating weaker interatomic bonding and structural ordering in the *C40* compared to the *C11b*.

The primary barrier to $NbSi_2$ implementation is its poor oxidation resistance. Unlike the volatile $MoO_3$, niobium oxides ($Nb_2O_5$) remain stable on the surface. The thermodynamic stability of $Nb_2O_5$ causes a burden for $NbSi_2$, as it forces the growth of a mixed $SiO_2/Nb_2O_5$ scale rather than a pure protective layer. This becomes a structural liability: the massive molar volume expansion triggered by the formation of niobium oxide generates intense internal stresses. These mechanical forces eventually cause the oxide to crack and spall away from the surface. This fragmentation prevents the material from establishing a continuous, self-healing silica film. The issue is compounded by a fundamental kinetic mismatch: silicon diffusion within niobium silicides is much slower than in the molybdenum-based alternatives, meaning the surface cannot be repaired fast enough to stop the degradation. Additionally, $NbSi_2$ remains highly vulnerable to pest oxidation, occuring in a broad temperature window between 773K and 1173K.

While precise resistivity data for bulk $NbSi_2$ is limited, being Nb's resistivity slightly higher than Mo, it could be empirically expected to exceed that of $MoSi_2$ [39][41][43][44][46][47][53].

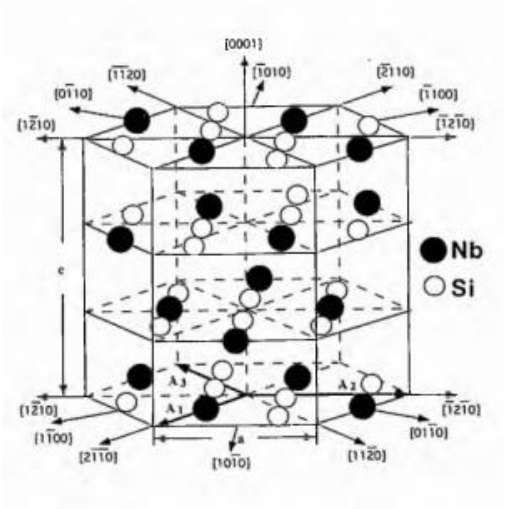


*Figure 20. C40 structure of NbSi2 [44]*

Medium and high entropy silicide alloys (Mo,W,Ta,Nb,Cr)$Si_2$ that inlude $WSi_2$ and NbSi2 type structure exhibit total IR emissivity values of 0.4-0.5 at room temperature, increasing to 0.7-0.8 at elevated temperatures, suggesting that binary $WSi_2$ is likely in a similar range.

Tantalum, in the end, is one of the most corrosion-resistant refractory metals, widely used in aggressive chemical environments. Due to this, tantalum is widely applied in chemical equipment like heat exchangers, reaction vessels and tubes. However, it is highly reactive at elevated temperatures, absorbing hydrogen, oxygen, nitrogen, and carbon to form brittle hydrides, oxides, nitrides, or carbides. Consequently, Ta must be operated in high vacuum ($<10^{-4}$ torr) or high-purity inert atmospheres (Ar/He), where it can reach 2400°C. It should be noted that tantalum's supply is very unstable and so it is very expensive when compared to either molybdenum or tungsten. The average price can be approximately one half of that listed for platinum. Ta is notably ductile and maintains this property after recrystallization, provided it is shielded from interstitial contaminants. However, its high cost (approximately half that of platinum) and volatile supply chain limit its widespread industrial application. $TaSi_2$ adopts the hexagonal *C40* structure, with a density of 9.25 g/cm³ and a melting point of ~ 2025°C.

Compared to the extensive literature on other silicides, research into bulk $TaSi_2$ remains quite sparse. Most of the existing data is derived from thin-film studies, where samples are typically fabricated via Physical Vapor Deposition (PVD) techniques such as DC sputtering, co-sputtering, or reactive sputtering. These thin film analyses report a characteristic room-temperature resistivity of ~ 50 μΩ·cm, with a positive Temperature Coefficient of Resistance (TCR). However, translating these electrical properties into high-temperature applications is hindered by vulnerability to atmospheric oxidation. While the material is theoretically capable of developing a $SiO_2$ layer, this process is frequently interrupted by the simultaneous growth of $Ta_2O_5$ (which possesses a high melting point of 1800°C). The co-formation of this stable tantalum oxide disrupts the continuity of the silica scale, preventing the development of the protective, passivating barrier required for long-term survival in air.

Furthermore, the density of $Ta_2O_5$ (8.20 g/cm3) is lower than that of $TaSi_2$ (9.14 g/cm3). The 3.86% molar volume increase during $Ta_2O_5$ formation induces microcracking and fragmentation of the silicide. Mechanically, $TaSi_2$ behaves as a typical refractory silicide, exhibiting brittleness at low temperatures and improved plasticity only at high temperatures. The emissivity is expected to be like the other disilicides. In engineering use, TaSi2 is usually

treated as brittle at low temperature with improved deformability only at elevated temperature, consistent with the general mechanical behavior of many refractory silicides [40][49].

### 4.1.2. Metallic Alloys

Metallic alloys represent a mature material family with extensive industrial implementation in resistive heating applications. Commercially available products are primarily categorized into Nickel-Chromium (NiCr) and Iron-Chromium-Aluminum (FeCrAl) systems. These alloys are characterized by high cost-effectiveness, fabrication versatility, and superior resilience to mechanical and thermal shock. A key operational advantage is their stable electrical resistance relative to both temperature fluctuations and service life, which simplifies power supply design and control logic. Furthermore, these materials exhibit high reliability under frequent thermal cycling. However, their primary technical constraint is a relatively low maximum service temperature in oxidizing environments compared to ceramic or intermetallic alternatives.

NiCr alloys have been a standard in electric heating since the early 20th century. Suitable materials for heating elements are classified under A.S.T.M. grades: Grade "A" (80/20 Nichrome), Grade "B" (70/30 Nichrome), Grade "C" (60/15 Nichrome), and Grade "D" (35/20 Nichrome). The physical and thermal properties of these grades are summarized in Table 5.

The maximum operating temperature for NiCr alloys is generally limited to <1250°C, with a solidus temperature near 1400°C.

*Table 5. NiCr alloys properties [62]*

| | A grade 80/20 NiCr | 70/30 NiCr | C Grade 60/15 NiCr | D Grade 35/20 NiCr |
|---|---|---|---|---|
| UNS | N06003 | N06008 | N06004 | None |
| Highest service temperature in air | 1200oC or 2200oF | 1260oC or 2300oF | 1150oC or 2100oF | 1100oC or 2000oF |
| Melting point | 1400oC or 2550 oF | 1380oC or 2520 oF | 1390oC or 2530oF | 1390oC or 2530oF |
| Specific gravity | 8.41 | 8.11 | 8.25 | 7.95 |
| Density | 0.304 lb/in3 | 0.293 lb/in3 | 0.298 lb/in3 | 0.287 lb/in3 |
| Specific heat | .107 Btu/lb/F | .110 Btu/lb/F | .107 Btu/lb/F | .110 Btu/lb/F |
| Tensile strength | 830 MPa or 120 ksi | 900 MPa or 130 ksi | 760 Mpa or 110 ksi | 620 Mpa or 90 ksi |
| Yield strength, .2 % | 415 MPa or 60 ksi | 485 MPa or 70 ksi | 380 Mpa or 55 ksi | 345 MPa or 50 ksi |
| Elongation % | 240 MPa or 35 ksi | 240 MPa or 35 ksi | 240 MPa or 35 ksi | 240 MPa or 35 ksi |
| Reduction of area | 55 % | 55 % | 55 % | 55 % |

While these alloys exhibit excellent cold-workability and ductility for coiling, they are susceptible to significant creep deformation at elevated temperatures. The resistivity value is around 110 μΩ·cm @ room T, with a positive but very low TCR. The electrical resistivity is also influenced by Cr-concentration, as shown in Figure 21. This is due to the higher resistivity of Cr, almost double the Ni one.

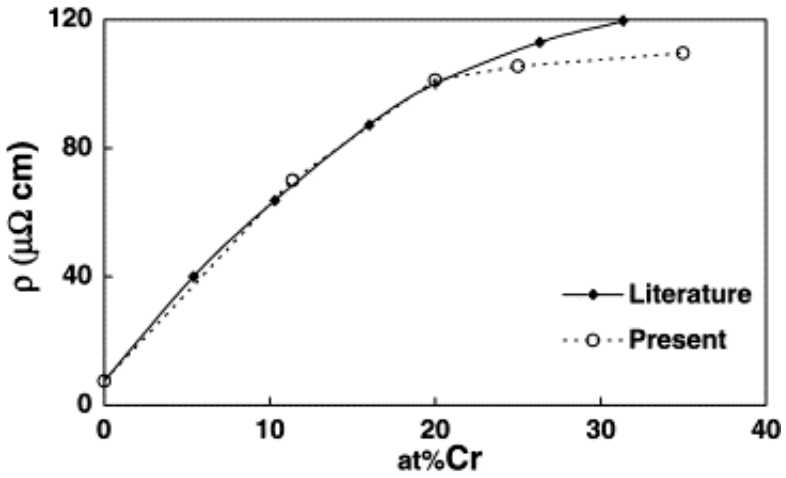


*Figure 21. NiCr resistivity as a function of Cr-concentration [58]*

In air, NiCr forms a $Cr_2O_3$-based scale with some spinel type oxides, which provides good oxidation resistance up to roughly 1100-1150 °C at the metal/scale interface. The protective scale is generally adherent and self-healing if Cr supply is sufficient, but at higher temperatures it can grow rapidly, spall, or transform toward less protective mixed oxides, especially under cyclic thermal loading. Over extended periods of high-temperature service, chromium is progressively leached from the subsurface region. If the local chromium concentration falls below the critical threshold required to maintain a continuous $Cr_2O_3$ scale, the oxidation rate accelerates sharply. This localized thinning of the element's cross-section creates high-resistance spots, which ultimately lead to premature structural failure. Furthermore, the presence of water vapor, sulfur, or aggressive process gases can significantly destabilize the protective scale, drastically shortening the element's operational life compared to idealized dry-air laboratory data. Visually and thermally, the emissivity of NiCr wires begins around 0.65-0.70 in their pure state, though this value reaches 0.90 once a robust oxide layer has matured [58][62][63].

For more demanding high-temperature environments, FeCrAl alloys are the preferred choice due to their superior oxidation kinetics and high electrical resistivity. A typical high-performance composition consists of roughly 70-80% Fe, 15-22% Cr, and 4-7% Al, often supplemented with trace rare-earth elements to enhance scale adhesion. A standard benchmark for these alloys is a 72.5% Fe / 22% Cr / 5.5% Al blend. These materials are characterized by:

- Density: approximately 7.1-7.2 g/cm³
- Melting point: near 1500°C

- Thermal conductivity: notably low, in the range 11-15 W/(mK)
- Thermal expansion: a coefficient comparable to that of standard stainless steel.

The higher grades made by traditional melt technology have limiting temperatures of 1400°C on the element with chamber temperatures typically 1300°C. At room temperature FeCrAl has tensile strength of ~500-800 and yield strength ~470-545 MPa, with elongation to fracture ~15-25 %. At elevated temperature (~900 °C), tensile strength drops to tens of MPa, and creep strength becomes the design limiting property for unsupported elements.

FeCrAl alloys are characterized by a typical room-temperature resistivity in the 135-145 μΩ·cm range, paired with a modest positive TCR. This stability makes them a predictable choice for resistive heating applications.

In oxidizing environment, once the material surpasses 1000°C, it triggers the formation of a dense, highly adherent $Al_2O_3$ layer. Rather than a simple surface change, this scale acts as a sophisticated kinetic barrier. By significantly impeding the inward diffusion of oxygen, the alumina effectively stops the degradation of the underlying metal, shielding the core from internal oxidation and ensuring a prolonged service life. The growth of this oxide scale follows parabolic rate kinetics, where the thickness increases at a decreasing rate over time, ensuring long-term stability without excessive scaling, like the chromium oxide scale. However, it has one very important difference: it is very thin and adheres tightly to the base metal, making it less likely to flake off and lead to product contamination. As the element is thermally cycled, small cracks may develop in the oxide, which eventually will lead to aluminum depletion in the base metal. Generally, this aluminum depletion occurs at a much slower rate than the chromium depletion in NiCr materials of similar configuration. The oxide is very resistant to carbon infiltration and is particularly stable in the presence of sulfur. The oxide is also an excellent electrical insulator, which is beneficial should element sections inadvertently touch. This situation can be disastrous in the case of chromium oxide protected materials.

FeCrAl alloys typically have a higher use temperature, higher resistance, and lower density than NiCr. They offer lower cost, easier fabrication and longer lifetime than NiCr, but cannot reach the 1600-1800 °C regime where $MoSi_2$ operates and suffer more creep and dimensional change at the top of their range. On the downside, it also shows a lower hot strength, reduced ductility, and embrittlement with use.

In the past few years, FeCrAl alloys have been introduced that use powder metal technology in their manufacturing process. The advantage gained by this extended and fairly expensive process is a FeCrAl product that has improved hot strength and creep resistance, leading to better form stability, reduced need for supports, and less sagging and resistance drift during long-term operation near their maximum rating. In one case, the resultant maximum element temperature is listed at 1425°C [59][60][61].

### 4.1.3 Carbides and Carbon-Based Materials

Graphite, a crystalline allotrope of carbon, was initially evaluated as a potential alternative material due to its exceptional thermal stability and superior thermophysical properties. It stands out in the refractory landscape due to unique thermal advantages, most notably its high thermal conductivity and a favorable CTE, secured by a sublimation point near 3600°C. Unlike many materials that degrade as they heat up, graphite exhibits a positive correlation between temperature and thermal conductivity, with values reaching 1500-2000 W/(mK). This high conductivity, paired with a low modulus of elasticity and a small friction coefficient, grants the material an almost excellent resistance to thermal shock. Perhaps the most striking characteristic of graphite is its anomalous mechanical behavior. While it lacks the structural integrity of conventional metals at room temperature, its strength increases as it is heated through the 1000-2500°C range. This inverse relationship suggests that extreme environments actively optimize its structural performance rather than degrading it. Furthermore, with a high hemispherical emissivity (ranging from 0.80 to 0.95), graphite remains a highly efficient radiator, even as its emissivity slightly decreases at peak temperatures. Its low density (1.6-2.2 g/cm$^3$) also offers a significant advantage over refractory metals: the resulting reduction in mass simplifies furnace architecture and eases the physical demands of on-site maintenance.

Despite these traits, graphite is hindered by its susceptibility to environmental contamination, driven by two distinct mechanisms: particulate shedding and outgassing. Because of its relative softness, the material can release micro-particles from its surface, which may contaminate the surrounding environment. More critically, graphite’s inherent porosity allows it to act like a sponge, adsorbing moisture, cleaning agents, and atmospheric vapors. When subjected to vacuum and high heat, these trapped molecules are violently released. This outgassing can compromise vacuum integrity and introduce impurities into metallurgical processes, potentially jeopardizing the final product's quality. In vacuum conditions, graphite remains operational up

to 2500°C; however, it is highly susceptible to rapid oxidation in aerobic atmospheres starting at 400-500°C. Its electrical resistivity is approximately one to two orders of magnitude higher than that of $MoSi_2$ [64][65][66][67][68][71][80]. The temperature dependence of its resistivity follows a trend analogous to $MoSi_2$, as depicted in Figure 22.

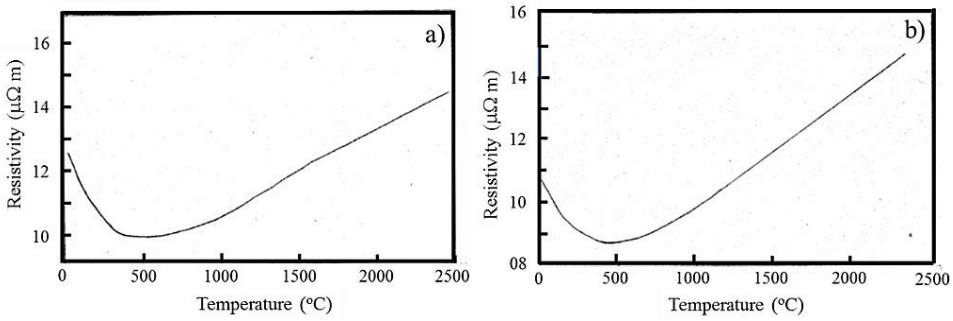


*Figure 22. Temperature dependence of resistivity for two electro-grade graphite materials [67]*

A prevalent industrial alternative to $MoSi_2$ for electric heating elements is constituted by Silicon carbide (SiC), attributed to its robust thermo-mechanical properties and specific electrical resistivity. The fundamental physical and thermal properties of SiC are synthesized in Table 6. A defining characteristic of SiC is the absence of a liquid phase under standard processing conditions; it remains rigid across all practical operating temperatures. SiC elements are typically manufactured via recrystallization or reaction-bonding processes. Unlike fully dense heating elements, the resulting hot sections of SiC components are characterized by a residual porosity ranging from 8% to 30%. This porous architecture allows the surrounding atmosphere to react not only with the external surface but also throughout the bulk of the material. This differentiates SiC elements from other element types, which are fully dense, and can react only on the surface of their hot section.

*Table 6. SiC properties*

| **SiC main properties** | |
|---|---|
| Density | 3.1 g/cm³ |
| Thermal conductivity | 120 W/(mK) |
| CTE | $4.0 \times 10^{-6}$°C$^{-1}$ |
| Emissivity | ~0.8 |
| Resistivity | ($10^2$-$10^6$ Ω·cm) |
| Melting point | 2830°C |

This volumetric reactivity leads to a phenomenon known as aging. In oxidizing environments, SiC undergoes a chemical reaction to form silicon dioxide ($SiO_2$) and carbon dioxide ($CO_2$). Oxygen infiltrates the porous structure and attacks the intergranular bridge points, converting the carbide into silica. While the growth of a $SiO_2$ layer generally serves as a robust passivating barrier, this protective skin is constantly under seige from thermal cycling, mechanical wear, and chemical erosion. Once this barrier is breached, the underlying virgin SiC is immediately exposed to fresh oxidative attack. As the core material is consumed to reform the oxide, the effective conductive cross-section of the element is incrementally reduced. This physical thinning manifests as a progressive rise in electrical resistance over time.

For typical SiC elements, the maximum recommended operating temperature is 1650°C. The aging rate is further accelerated by thermal cycling in air due to the granular nature of the material and the specific thermal expansion coefficient of the formed silica. Furthermore, SiC is susceptible to mechanical shock, while its thermal shock resistance varies from moderate to excellent depending on the specific manufacturing process and material grade. Commercial geometries include straight rods, multi-leg elements, and spiral-cut configurations, the technical specifications of which are detailed in the subsequent sections [69][70][73][76][77].

A subsequent investigative step was undertaken to bridge the previously analyzed transition metals with the exceptional ceramic properties, ultra-high temperature resistance, and the high electrical resistivity inherent to carbon-based systems. In reviewing the established literature, a specific set of transition metal carbides, most specifically those of tantalum, hafnium, tungsten, and zirconium, consistently emerges as the focal point for high-temperature research. These compounds are frequently championed as ideal candidates because they possess the thermal resilience of ceramics while retaining the electrical and structural advantages of metals. Among these, tungsten carbide (WC) is perhaps the most remarkable. As a stoichiometric compound with equal molar proportions of tungsten and carbon, it offers a formidable combination of physical traits. With a high density of approximately 15 $g/cm^3$, its macrocrystalline structure provides a level of mechanical strength, fracture toughness, and operational longevity that simply cannot be matched by conventional metallic alloys. In industrial heating, this translates to a material that can withstand extreme thermal loads without the rapid structural degradation typical of less robust refractory systems.

In its hexagonal form, the lattice consists of layers of tungsten atoms lying directly over one another, with carbon atoms occupying half of the interstices; this results in a regular trigonal prismatic coordination for both atoms. Usually, to synthesize this material, tungsten metal or powder is reacted with carbon at temperatures between 1400°C and 2000°C. The resulting material is a fine gray powder produced in over 20 unique grades, varying in grain size, tensile strength, hardness, and melting point, allowing for high adaptability.

Mechanically, WC is defined by a combination of extreme strength and inherent brittleness. While it boasts exceptional compressive and tensile ratings, its lack of ductility remains a significant constraint in high-impact or structurally dynamic environments. This mechanical rigidity is matched by an equally robust thermal profile, characterized by a high melting point of 2780°C, a thermal conductivity of 110 W/(mK), and a remarkably low coefficient of thermal expansion. The electrical behavior of WC reveals a more complex, non-linear temperature dependency. At lower ranges (between -50 and 200°C), the material follows a traditional metallic trend: conductivity drops by approximately 8% per 100°C as lattice vibrations increase electron scattering. Once the material surpasses 800°C, it exhibits an anomalous spike in conductivity. This departure from standard metallic behavior is likely driven by high-temperature lattice reconstruction or shifts in defect-induced carrier mobility, phenomena that suggest WC may behave quite differently under extreme thermal loads than simplified models predict.

Chemically, WC is characterized by its high degree of inertness, resisting most mineral acids at room temperature. Its primary vulnerabilities are limited to aggressive hydrofluoric/nitric acid mixtures or halogen gases; it reacts with fluorine at ambient temperatures and chlorine once heated beyond 400°C. Crucially for furnace design, WC remains entirely unreactive in dry $H_2$ environments right up to its melting point

The oxidation of bulk WC begins at 500-600°C, yet the scientific literature regarding its oxidation kinetics remains inconsistent. Early studies suggested that WC oxidizes an order of magnitude faster than pure tungsten between 700°C and °C due to $CO_2$ gas evolution at the interface causing scale cracking and porosity; however, more recent evidence suggests thicker oxide scales form on pure W in the 0-500°C range. This versatility, combined with its high abrasion resistance and sharp edge retention, ensures high equipment effectiveness and a low total cost of ownership in mission-critical applications [78][79].

Complementing the properties of tungsten carbide are the tantalum carbide (TaC) and hafnium carbide (HfC), which are distinguished by even higher thermal and structural thresholds, including melting points exceeding 3800°C, elastic moduli surpassing 500 GPa, and Vickers hardness values ranging from 15 to 20 GPa. Both carbides crystallize in the same cubic NaCl-type structure, allowing for the formation of a continuous, single-phase $Ta_xHf_yC_{x+y}$ solid solution. At the atomic level, bond overlap analyses reveal a fundamental divergence in character: the Hf-C bond is a hybrid of covalent and ionic forces, while the Ta-C bond leans more heavily toward pure covalency. By integrating these two phases, engineers can develop ceramics with superior elastic properties and enhanced thermal conductivity at high temperatures.

However, mechanical improvements do not scale monotonically with TaC addition; instead, there is a complex trade-off as the composite's overall metallicity increases, which can compromise the element's hardness. Furthermore, their extreme thermal stability makes experimental validation difficult, leaving a notable gap in the understanding of their specific melting points and electronic transport behaviors.

The same high-strength covalent bonding that makes TaC and HfC so desirable also creates a massive technical obstacle. Because of their low self-diffusion coefficients and rigid bonding, consolidating these pure ceramics into dense, usable components is exceptionally difficult. Even with advanced techniques like hot pressing or pressureless sintering, achieving full densification remains a metallurgical challenge that often necessitates specialized additives or extreme processing environments.

For pure TaC, which is an isotropic material, the Young's modulus is reported between 531 and 549 GPa, highly dependent on specimen density and porosity, while its room-temperature electrical resistivity ranges from 15 to 42 μΩ cm and its thermal conductivity is approximately 22 W/(mK). The oxidation of tantalum carbide initiates in atmospheric conditions within the temperature range of 500-650 °C, resulting in the formation of tantalum pentoxide ($Ta_2O_5$). The weakness of the resulting oxide phase lies in its sintering kinetics. Because the particles fail to fuse effectively, the surface develops a loose, porous architecture rather than a dense, hermetic seal. This structural deficiency creates an open pathway for the continuous inward diffusion of oxygen, leaving the underlying material permanently vulnerable. At extreme temperature thresholds, the situation shifts from passive degradation to active

destruction as the $Ta_2O_5$ layer undergoes liquefaction. While the molten oxide to provide a transient glazing effect against further oxidation, at the same time triggers a catastrophic structural erosion. This liquid phase aggressively dissolves the TaC substrate, facilitating the dissociation of carbon and the violent evolution of gaseous carbon oxides ($CO/CO_2$). Although the transition to a fully oxidized state occurs near 1000 °C, the oxidation kinetics exhibit a pronounced acceleration between 1400 °C and 1800 °C when exposed to oxidizing environments [72][74]. While they may not match the specific balance of toughness found in WC-binder composites, the TaC-HfC system represents the pinnacle of thermal stability for mission critical applications in the most demanding thermochemical environments.

Completing this list of refractory carbides is zirconium carbide (ZrC), a material categorized as a metal-like ceramic characterized by mixed ionic and covalent bonding. ZrC is increasingly viewed as a viable, cost-effective alternative to traditional refractory metals and other ultra-high-temperature ceramics due to its high melting point (>3500°C), exceptionally low vapor pressure even at temperatures exceeding 2000°C, and significantly lower specific mass compared to tungsten-based counterparts. While it exhibits lower electrical and thermal conductivities than molybdenum or tungsten, these characteristics are advantageous for specific applications such as electrical heating elements (Figure 23) and thermal composite structures.

ZrC heating element properties are summarized in Table 7. Thermophysically, ZrC demonstrates a linear progression of electrical resistance up to 2000°C, high mechanical strength, and a fracture toughness comparable to that of silicon carbide (SiC). Chemically, it maintains outstanding corrosion stability under non-oxidizing atmospheres. However, under oxidizing conditions at 1073K, the material follows linear oxidation kinetics governed by the inward diffusion of oxygen through an intermediate scale layer of constant thickness. This layer comprises amorphous carbon and $ZrO_2$ nanocrystals, with oxygen diffusion measured at $9 \times 10^{-10} \mathrm{cm}^2 \mathrm{s}^{-1}$.

Historically, the industrial adoption of ZrC was constrained by the technical difficulty of producing large-format, high-density components. Recent advancements in manufacturing technology, specifically coordinated pressureless sintering processes, have overcome these limitations, enabling the fabrication of dense ZrC geometries, including plates and rods, with lengths exceeding 250 mm.

*Figure 23. ZrC heating elements [81]*

Beyond its thermomechanical performance, ZrC offers a superior economic and strategic profile; it is less expensive than many refractory alternatives and does not rely on critical or scarce raw materials, ensuring a more secure supply chain. These factors, combined with its high hardness, stiffness, and chemical resilience, position ZrC as a critical material for advanced fluid lines, structural elements, and thermal protection systems, ultimately enhancing the reliability and operational uptime of high-temperature industrial processes [75][81].

*Table 7. Material properties of ZrC heating elements [81]*

| Parameter | Value | Unit | Application facts |
|---|---|---|---|
| Density (theoretical) | 6.73 | $g \cdot cm^{-3}$ | |
| Density (sintered) | 6.63 | $g \cdot cm^{-3}$ | 98.5 % of the theoretical density; ceramically practical complete compaction possible |
| Open porosity | 0.05 | Vol.% | No significant interactions with the environment |
| Melting point ZrC | 3532 | °C | Refractory material with higher melting point than tungsten (3422 °C) |
| 4-point bending strength / RT | 350–450 | MPa | Usual strength of high-quality ceramic materials such as SiC |
| 4-point bending strength / 1400 °C | 150–230 | MPa | High strength level even at higher temperatures; strength decreases with temperature |
| 4-point bending strength after aging at 1900 °C at RT | 350–450 | MPa | No loss of strength due to thermal load |
| Fracture toughness | 4 | $MPa \cdot m^{1/2}$ | Similar to SiC |
| E-modulus / RT | 410 | GPa | High stiffness, like SiC |
| Expansion coefficient / RT | 5.4 | $10^{-6} \cdot K^{-1}$ | |
| Expansion coefficient / 2000 °C | 7.1 | $10^{-6} \cdot K^{-1}$ | |
| Spec. electrical resistance / RT | $6.8 \cdot 10^{-5}$ | Ωcm | Metal-like electrical resistance, relatively high |
| Spec. electrical resistance / 2000 °C | $2.1 \cdot 10^{-4}$ | Ωcm | Moderate positive temperature coefficient |
| Thermal conductivity / RT | 31 | $W \cdot (mK)^{-1}$ | Moderate thermal conductivity like $Al_2O_3$ or $Si_3N_4$ |
| Thermal conductivity / 2000 °C | 38 | $W \cdot (mK)^{-1}$ | Moderate increase in thermal conductivity |
| Spec. heat capacity / RT | 0.355 | $J \cdot (gK)^{-1}$ | |
| Spec. heat capacity / 2000 °C | 0.490 | $J \cdot (gK)^{-1}$ | |

### 4.1.3. UTHC (Ultra High Temperature Ceramics)

Another alternative solution for high-temperature applications involves materials synthesized according to the same constitutional principles as $MoSi_2$: the combination of a refractory transition metal with a semi-metallic or metalloid element. Zirconium diboride ($ZrB_2$) and hafnium diboride ($HfB_2$) represent the primary candidates within this category.

These ceramics are characterized by a hybrid bonding profile that merges metallic agility with covalent-ceramic rigidity. Their ceramic side is defined by high thermal conductivity, moderate thermal expansion, and a formidable Vickers hardness. Yet they simultaneously behave like metals, maintaining high electrical conductivity (low resistivity). The baseline physical and thermal profiles for these two borides are synthesized in Table 8.

Historically, $ZrB_2$ and its derivatives were dismissed as unsinterable due to the extreme strength of their covalent bonds and notoriously low self-diffusion coefficients. However, modern processing has turned the trend; it is now possible to achieve fully densified, fine-grained microstructures at temperatures below 2000°C through both pressure assisted and pressureless routes. A review of the fabrication routes reveals three pillars for successful densification:

- Chemical scavenging: the use of reactive sintering aids to remove detrimental surface oxides ($ZrO_2$ or $B_2O_3$) that otherwise inhibit grain boundary motion.
- Morphological control: reducing the initial powder particle size to maximize the surface-energy driving force for sintering.
- Volatile Management: Implementing critical degasification stages during pressure-assisted consolidation to vent entrapped impurities.

While advanced techniques such as Spark Plasma Sintering, microwave sintering, and Hot Pressing have pushed $HfB_2$ composites toward their theoretical density limits, they often struggle with scalability. These methods are frequently confined to simpler, smaller geometries. For industrial applications requiring large-scale components or complex geometries, pressureless sintering remains the most commercially viable path forward.

The intrinsic, similar properties of these diborides suggest significant potential for use as resistive heating elements in environments exceeding 1800 °C. Nevertheless, their practical application is severely constrained by their oxidation kinetics in atmospheric conditions.

*Table 8. ZrB2 and HfB2 basic relevant properties*

| | $ZrB_2$ | $HfB_2$ |
|---|---|---|
| Melting T | 3245°C | 3250°C |
| Thermal conductivity | 85 W/mK | ~80 W/mK |
| Resistivity @ room T | 22 μΩ cm | 8-15 μΩ cm |
| Density | 6.09 g/cm³ | ~10.5-11 g/cm³ |
| CTE @ room T | ~2.5-3.5x$10^{-6}K^{-1}$ | ~3.5-4.5x$10^{-6}K^{-1}$ |

With respect to their mechanical performance, $ZrB_2$ exhibits a high room-temperature flexural strength of approximately 447 MPa. This value undergoes a significant reduction to 196 MPa at 1800 °C, followed by a notable recovery to 360 MPa at 2300 °C when evaluated under inert atmospheric conditions.

$ZrB_2$ fracture toughness ($K_{IC}$) jumps from 2.3 MPa·$m^{1/2}$ at ambient conditions to 3.1 MPa·$m^{1/2}$ at 2200°C. This is supported by a great Vickers hardness (13-23 GPa) and a rigid elastic modulus of approximately 489 GPa. These traits are the direct consequence of the material's dense covalent bonding and hexagonal crystal symmetry. However, these intrinsic strengths are highly sensitive to variables such as grain size distribution and chemical purity. As will be explored in later sections, the introduction of secondary phases, specifically SiC, can further reinforce flexural strength through complex reinforcement mechanisms. Similar mechanical properties are observed in $HfB_2$, with both diborides demonstrating an almost excellent resistance to creep and plastic deformation under massive thermal loads.

Despite their structural brilliance, these borides face a performance degradation once they surpass 1400°C. At these temperatures, the $B_2O_3$ liquid phase, which provides a degree of protection at lower temperatures, begins to volatilize rapidly. This leaves behind a skeleton of $ZrO_2$ (or $HfO_2$ in the case of hafnium diboride) that is catastrophically porous. Without the boria liquid to seal the gaps, the scale allows oxygen to migrate freely into the substrate and trigger degradation.

In summary, the combination of inadequate high-temperature oxidation resistance, excessively low electrical resistivity for standard heating applications, high raw material costs, and

manufacturing complexity renders these monolithic borides less competitive from a commercial standpoint as discrete electric heating elements. By strategically integrating secondary ceramic phases, these inherent weaknesses can be mitigated by creating a hybrid material capable of surviving more hostile environments [82][83][84][85].

### 4.2. Current commercial alternatives

Several of the refractory materials discussed in the preceding sections have reached significant commercial maturity as electric heating elements. Beyond the established use of $MoSi_2$, the most prevalent industrial technologies are based on Silicon Carbide (SiC), Nickel-Chromium (NiCr), and Iron-Chromium-Aluminum (FeCrAl) alloys. To provide a rigorous comparative analysis, this study references the product portfolios of Kanthal®, an industry benchmark and the most consolidated manufacturer in the field of electric heating.

Kanthal® is the global leader in the production of SiC heating elements, marketed primarily under the Globar® brand. Unlike metallic heating elements that tend to soften or creep as they approach their thermal limits, SiC maintains its structural integrity at temperatures as high as 1625°C. This high-temperature stiffness represents a profound advantage in engineering, as the material remains entirely self-supporting regardless of its physical orientation. By eliminating the need for complex and costly auxiliary support systems, SiC allows furnace designers to span horizontal or vertical gaps without the risk of sagging or mechanical deformation.

They are available in a broad range of geometries, with standard diameters ranging from 10 up to 55 mm, hot zone lengths up to 4.2 m, and total lengths extending to 6 m. This physical scale is complemented by an exceptional power-handling capability; SiC can sustain surface power loadings that far exceed those of conventional metallic alloys. This allows for a more compact furnace footprint, reducing the total number of elements required while maintaining the necessary thermal output.

From a structural standpoint, SiC elements are available in various configurations, ranging from basic rods and tubes to sophisticated multi-leg geometries (Figure 24). In multi-leg designs (2, 3, or 4 legs), individual components are matched for electrical resistance to ensure uniform current distribution and load balancing. These segments are integrated into a monolithic α-SiC architecture using specialized silicon carbide bridges.

Unlike traditional joining methods, such as cements or welds, which often introduce thermal or mechanical bottlenecks, these bridges maintain the chemical and structural integrity of the entire element. By maintaining a uniform material profile across the joint, the system avoids the hot spots and mismatched expansion coefficients that typically afflict conventional assemblies [69][89].

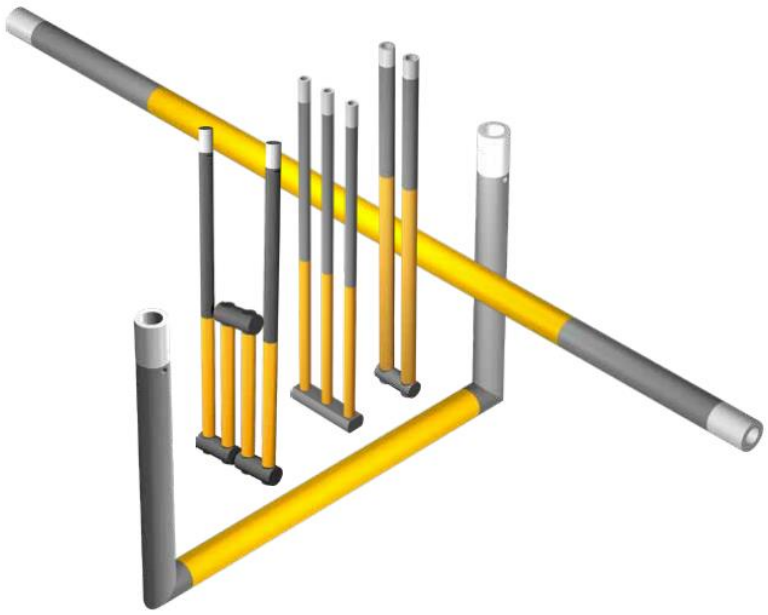

*Figure 24. Globar® SiC elements shapes [69]*

Parallel to its ceramic offerings, Kanthal maintains a dominant role in the production of high-performance metallic resistance alloys, specifically the FeCrAl (Kanthal®) and NiCr (Nikrothal®) series. FeCrAl alloys are generally favored for higher-intensity environments, for element temperatures up to 1425°C, whereas the NiCr-based alternatives provide a stable, reliable solution for applications capped near 1250°C. The choice between these two alloy families is dictated by the specific atmospheric and electrical requirements of the furnace, with FeCrAl offering superior oxidation resistance at the extreme upper end of the metallic temperature scale.

These alloys are commercially available in diverse forms, including wire, rod, and strip (ranging from 0.10-3.5 mm in thickness and 4-195 mm in width), to accommodate specific resistance and high-temperature requirements. The fundamental properties of these alloys are summarized in Table 9.

*Table 9. Kanthal® and Nikrothal® base properties [90]*

| | | KANTHAL® | KANTHAL® | | | NIKROTHAL® | | | |
|---|---|---|---|---|---|---|---|---|---|
| | | APM | A-1 | AF | D | 80 | 70 | 60 | 40 |
| Max continuous operating temp. °C | | 1425 | 1400 | 1300 | 1300 | 1200 | 1250 | 1150 | 1100 |
| Nominal composition, % | Cr | 22 | 22 | 22 | 22 | 20 | 30 | 15 | 20 |
| | Al | 5.8 | 5.8 | 5.3 | 4.8 | – | – | – | – |
| | Fe | balance | balance | balance | balance | – | 5% | balance | balance |
| | Ni | – | – | – | – | balance | balance | 60 | 35 |
| Resistivity at 20°C, $\Omega mm^{-2}m^{-1}$ | | 1.45 | 1.45 | 1.39 | 1.35 | 1.09 | 1.18 | 1.11 | 1.04 |
| Density, $g/cm^3$ | | 7.10 | 7.10 | 7.15 | 7.25 | 8.3 | 8.1 | 8.2 | 7.9 |
| Coefficient of thermal expansion, $K^{-1}$ | 20–750°C | 14×10-6 | 14×10-6 | 14×10-6 | 14×10-6 | 16×10-6 | 16×10-6 | 16×10-6 | 18×10-6 |
| | 20–1000°C | 15×10-6 | 15×10-6 | 15×10-6 | 15×10-6 | 17×10-6 | 17×10-6 | 17×10-6 | 19×10-6 |
| Thermal conductivity at 20°C, $Wm^{-1}K^{-1}$ | | 13 | 13 | 13 | 13 | 15 | 13 | 13 | 13 |
| Specific heat capacity at 20°C, $KJkg^{-1}K^{-1}$ | | 0.46 | 0.46 | 0.46 | 0.46 | 0.46 | 0.46 | 0.46 | 0.50 |
| Melting point, °C | | 1500 | 1500 | 1500 | 1500 | 1400 | 1380 | 1390 | 1390 |
| Mechanical properties (approx.)* | | | | | | | | | |
| Tensile strength, $N\ mm^{-2}$ | | 680 | 680 | 680 | 650 | 810 | 820 | 730 | 675 |
| Yield point, $N\ mm^{-2}$ | | 470 | 475 | 475 | 450 | 420 | 430 | 370 | 340 |
| Hardness, Hv | | 230 | 230 | 230 | 230 | 180 | 185 | 180 | 180 |
| Elongation at rupture, % | | 20 | 18 | 18 | 18 | 30 | 30 | 35 | 35 |
| Tensile strength at 900°C, $N\ mm^{-2}$ | | 40 | 34 | 37 | 34 | 100 | 120 | 100 | 120 |
| Creep strength at 800°C | | 11 | 6 | 8 | 6 | 15 | 15 | 15 | 20 |
| at 1000°C | | 3.4 | 1 | 1.5 | 1 | 4 | 4 | 4 | 4 |
| Magnetic properties | | magnetic (curie point 600°C) | | | | non | non | slightly | non |
| Emissivity, fully oxidized condition | | 0.70 | 0.70 | 0.70 | 0.70 | 0.88 | 0.88 | 0.88 | 0.88 |

* The values given apply for wire sizes of 4 mm diameter for the Kanthal alloys and of 1 mm for the Nikrothal alloys

Due to their higher operational temperature ceiling, Kanthal® (FeCrAl) alloys can withstand superior surface loadings (Figure 25a) and offer an operational lifespan 2 to 4 times greater than that of Nikrothal® (NiCr) when operated in air at equivalent temperatures (Figure 25d). The higher specific electrical resistivity of FeCrAl (Figure 25c) facilitates the use of materials with larger cross-sections, which is particularly beneficial for extending the life of thin wire components. Furthermore, the resistivity of FeCrAl alloys is notably more stable, exhibiting less sensitivity to cold-working and subsequent heat treatments compared to NiCr.

From a mechanical perspective, the higher yield strength of FeCrAl alloys minimizes plastic deformation during the coiling of the wire. Crucially, the oxidation behavior differs between the two: FeCrAl forms a protective alumina ($Al_2O_3$) scale, whereas NiCr forms a chromia ($Cr_2O_3$) scale. The alumina layer is more adherent, provides superior electrical insulation, is less prone to contaminating the furnace environment, and acts as a more effective diffusion barrier. Additionally, the $Al_2O_3$ scale offers enhanced resistance to carburizing atmospheres.

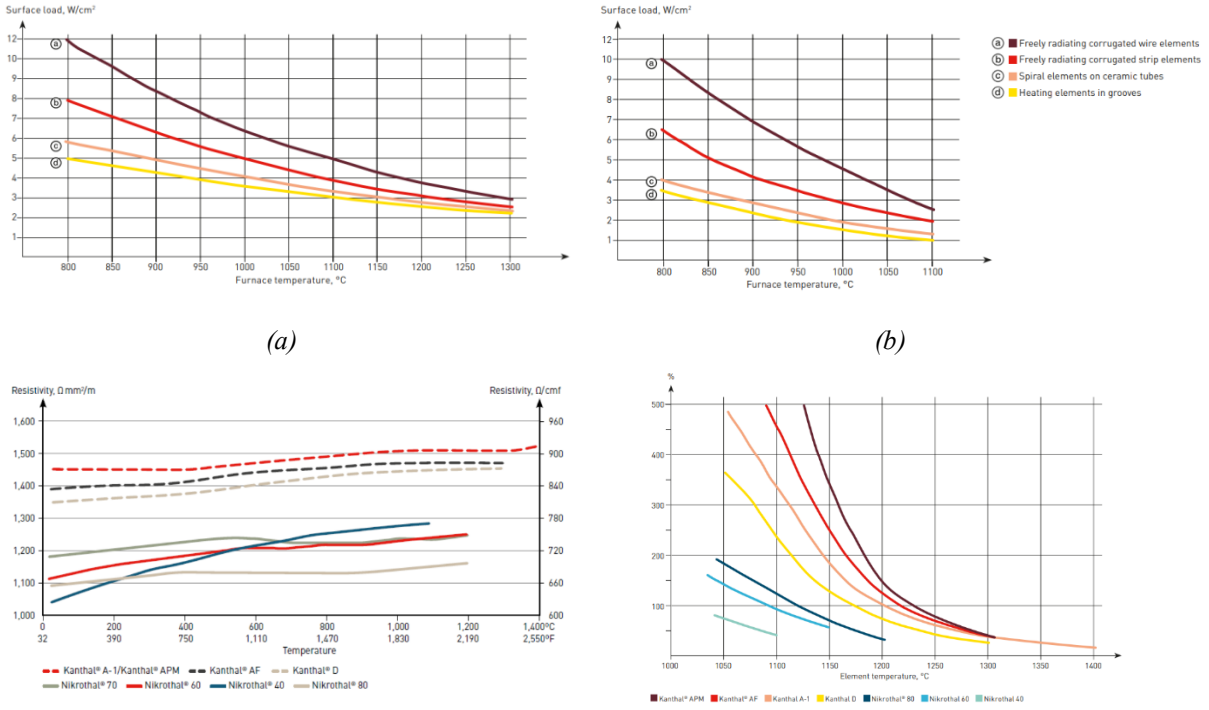


*Figure 25. Maximum reccomended Kanthal® surface loads (a), Maximum reccomended Nikrothal® surface load (b), Resisivity comparison (c), Comparative life (d) [90]*

Finally, FeCrAl alloys possess a lower theoretical density than NiCr alloys. This property, combined with higher resistivity, implies that a lower mass of material is required to achieve the same power output. When transitioning from NiCr to FeCrAl, engineers can either maintain wire diameter to reduce surface load or maintain surface load while reducing the wire diameter. In both scenarios, the high-performance characteristics of FeCrAl alloys lead to substantial weight reductions and cost efficiencies in industrial heating applications [59][60][61][90].

### 4.3. Comparative analysis with MoSi2

Table 10 provides a comparative summary of the decisive properties of $MoSi_2$ relative to the candidate materials evaluated in this study.

The comparative assessment of $MoSi_2$ against the identified candidate families, reveals a complex engineering landscape where no single monolithic material satisfies all the requirements for high-power industrial electrification. $MoSi_2$ remains the preeminent choice primarily due to its superlative oxidation resistance, enabled by the formation of a passivating, self-healing silica layer that allows for sustained operation at temperatures up to 1800°C. However, the data confirms the "resistivity paradox" that serves as the central motivation for this study; the low intrinsic resistivity of $MoSi_2$ necessitates thin, mechanically vulnerable geometries to reach the high electrical resistance required for high-voltage scaling, which in turn increases the risk of fracture and creep-induced deformation.

Furthermore, many emerging alternatives remain in the nascent stages of development, characterized by a lack of extensive longitudinal research. Currently, Globar® Silicon Carbide represents the most viable competitor; however, its operational envelope is constrained by lower peak temperatures and a higher susceptibility to oxidative aging. This accelerated degradation is attributed to the inherent porosity of the SiC microstructure, which compromises stability under extreme thermal loads. Consequently, SiC elements exhibit significantly lower specific surface load capacities compared to $MoSi_2$ (see Figure 26).

Evaluation of the alternative intermetallic silicides listed in the table, such as $WSi_2$, reveals only a marginal improvement in resistivity over $MoSi_2$. These materials are often disqualified by secondary failure mechanisms; for instance, the volatility of $WO_3$ actively destabilizes the protective scale at elevated temperatures. Transition metal silicides like $NbSi_2$ and $TaSi_2$ face similar hurdles in aerobic environments. Their oxides undergo significant molar volume expansion during formation, which triggers severe spallation and prevents the development of a coherent, passivating film. Furthermore, the data underscores a critical performance gap for Ultra-High Temperature Ceramics (UHTCs) like $ZrB_2$ and $HfB_2$. Despite melting points that surpass 3000°C, these ceramics undergo catastrophic oxidation in air above 1400°C. This degradation is driven by the rapid volatilization of boria, which leaves the remaining scale too porous to act as an effective oxygen barrier.

*Table 10. Materials comparison summary*

| MATERIAL | ELEMENTS | EMISSIVITY(ε) | MAX WORKING T | MECH-PHYS. PROPERTIES | THERMAL PROPERTIES | OXIDATION T | ρ |
|---|---|---|---|---|---|---|---|
| **$MoSi_2$** | Mo-Si | 0.70-0.85 | Around 1800◦ C | - Brittleness at low T<br>- Ductility at high T<br>- Density: 6.26 g/$cm^3$ | - Thermal cond @room T= 66.2 W/mK<br>- Th. Expansion coeff = 7-10×$10^{-6}$ $K^{1}$<br>- Risk of thermal shock failure with big T gradients<br>- Melting point: 2030 ◦ C | - Pest oxidation at low T (773 K)<br>- Silica layer at T> 1000◦ C | - From 23 to 27 μΩ cm @ room T, depending on fabrication procedure<br>- Linear increase with T and time independent |
| **$WSi_2$** | W-Si | - Polished form: ~0.3<br>- Oxidized: >0.8 | - Around 1600-1700 ◦ C in oxidizing atmospheres<br>- About 1800 ◦ C in inert or reducing enviroments | - Same crystal structure of MoSi2 (C11b)<br>- Density: 9.3 g/$cm^3$ | - Th. Expansion coeff = 8.5x$10^{-6}$ $K^{1}$<br>- Thermal cond @room T= 30-60 W/mK<br>- Melting point: above 2160◦ C | - Increase in mass gain between 773-1273 K<br>- Great mass loss at 1473 K($WO_3$ evaporation)<br>- T>1573 K mass change negligeble<br>- At high T>1300◦ C the kinetics are parabolic | 60-80 μΩ cm @room T |
| **$NbSi_2$** | Nb-Si | - Polished form: ~0.3<br>- 0.70-0.82 @high T (>800◦ C) | Lower than the others siicides | - Density: 5.62 g/$cm^3$<br>- C40 structure<br>- Bulk, shear and Young's moduli are smaller than $MoSi_2$ and $WSi_2$ | - Thermal cond lower than other metal disilicides<br>- Th. Expansion coeff: 11.7x$10^{-6}$$K^{1}$<br>Melting point: ~1950◦ C | - Pest degradation between 773 and 1173 K<br>- Linear oxidation until 1300 ◦ C, parabolic until 1450◦ C, then steady weight loss<br>- Volatilities of $Nb_2O_5$ very low<br>- Diffusion rate of Si very slow | 22-39 μΩ cm @room T |
| **$TaSi_2$** | Ta-Si | - Similar to the other silicides<br>- <$MoSi_2$ at high T | 1400-1600◦ C (hypothetical) | - Density: 9.25 g/$cm^3$<br>- C40 structure<br>- Brittle at low T and improved plasticity at high T | - Melting point: 2025◦ C<br>- Thermal properties similar to other silicides | - Formation of $Ta_2O_5$ disrupts the continuity of the silica scale<br>- $Ta_2O_5$ induces microcracking and fragmentation | ~50 μΩ cm @room T with positive TCR |
| **SiC** | Si-C | ~0.8 | ~1650◦ C | - Density: 3.1g/$cm^3$ | - Thermal cond @room T= 120-150 W/mK<br>- Th. Expansion coeff = around 4x$10^{-6}$$K^{1}$<br>- Melting point: 2830◦ C | - Silica layer between 1350 and 1500◦ C | - Between 5-50x$10^{4}$ μΩ cm @room T<br>- Sharp decrease until 600-800◦ C<br>- Increase after 800 ◦ C |
| **ZrC** | Zr-C | - ~0.6 for λ=0.65 μm between 1400-2500K<br>- nearly temperature-independent | Between 1800-2100◦ C (in vacuum or protective gas) | - Melting point: 3532 ◦ C<br>- Density: 6.73 g/$cm^3$<br>- Strength lower than refractory metals | - Moderate thermal cond @room T= 31 W/mK<br>- Th. Expansion coeff @room T= 5.4 $10^{-6}$$K^{1}$ | - Severe oxidation at T>800-1000◦ C<br>- Porous and non-adherent ZrO2 layers prone to spallation and catastrophic failure above 1500◦ C | - 43-68 μΩ cm @room T<br>- 210 μΩ cm @2000 ◦ C |
| **TaC** | Ta-C | Low ~0.3-0.43 @1000◦ C | - above 2000◦ C in oxidizing air<br>- closer to melting in vacuum | - Density: 14.5 g/$cm^3$ | - Thermal conductivity: 22 W/mK<br>- CTE: 6.6x$10^{-6}$$K^{1}$<br>- Melting point: >3800 ◦ C | - It starts at 500-650◦ C with $Ta_2O_5$ formation<br>- Non-protective, loose and porous surface<br>-Fully oxidized near 1000◦ C | 15-42 μΩ cm @room T |

| MATERIAL | ELEMENTS | EMISSIVITY (ε) | MAX WORKING T | MECH-PHYS. PROPERTIES | THERMAL PROPERTIES | OXIDATION T | ρ |
|---|---|---|---|---|---|---|---|
| **WC** | W-C | No WC standalone value. Similar refracrories ~0.8-0.9 | - around 500-600◦ C in oxy atmospheres<br>- around 800◦ C in non-oxy atmospheres | - Melting point: 2780◦ C<br>- El. Cond = $0.7x10^{6}$ S/m but anomalous increases at high T<br>- Density: 15 g/$cm^3$ | - Thermal cond @room T = 85-110 W/mK<br>- CTE = $5.4x10^{-6}K^{1}$ | - Poorer performance than W cause of $CO_2$ at interface<br>- Loss of inegrity and mechanical properties after 600◦ C | - About 20 μΩ cm @room T<br>- Decrease at high T |
| **W** | W | Aged filament: 0.32-0.35 | Around 2500◦ C in high vacuum or protective atmosphere: 1600-2000◦ C in $H_2$ atmosphere | - Density: 19.3 g/$cm^3$<br>- Britleness problem | - Thermal conductivity: 173 W/mK<br>- CTE around $4.8x10^{-3}K^{1}$ @0-100◦ C<br>- Melting point: 3410◦ C | - Initiates at ~ 500°C and becomes catastrophic at ~ 1200°C | Around 5.5 μΩ cm @room T |
| **FeCrAl** | Fe-Cr-Al | ~0.7 (Kanthal® alloys) | Up to 1425◦ C in air | - Density: ~7.1 g/$cm^3$<br>- Melting point: 1500◦ C<br>- Creep at elevated temperatures, design-limiting property | - Thermal conductivity: 11-15 W/mK<br>- CTE: 11-15x$10^{-6}K^{1}$ over 20-1000◦ C | - Continuous, adherent α-$Al_2O_3$ layer at T>1000◦ C<br>- Above 1450-1500◦ C alumina can break down<br>- Parabolic rate kinetics | ~135-145 μΩ·cm @room T |
| **NiCr (different grades)** | Ni-Cr | - Clean: 0.65-0.70<br>- Oxidized: ~0.9 | Up to 1250◦ C in air | - Density: 7.95-8.41 g/$cm^3$<br>- Excellent cold workability and ductility | - CTE: 14-19x$10^{-6}K^{1}$ over 20-1000◦ C<br>- Thermal comductivity: 13-15 W/mK<br>- Melting point: 1380-1400◦ C | - $Cr_2O_3$ based scale<br>- Good oxidation resistance up to 1100-1150◦ C | 95-118 μΩ·cm @room T with a poitive but low TCR |
| **Graphite** | C | - 0.80-0.95<br>- slightly decrease with T | Up to 2500◦ C in vacuum, much lower in air | - Density: 1.6-2.2 g/$cm^3$<br>- Tendency to particle shedding and outgassing (softness and porosity) | - Melting point: 3600◦ C<br>- Thermal conductivity: up to 1500-2000 W/mK | Oxidizes very quickly in air and starts degradating from 400-500◦ C | ~$10^3$ μΩ·cm |
| **$ZrB_2$** | Zr-B | Missing information | Up to 1400◦ C in air, higher in vacuum | Density: 6.09 g/$cm^3$ | - Melting point: 3245◦ C<br>- Thermal conductivity: 85 W/mK<br>- CTE: ~2.5-3.5x$10^{-6}K^{-1}$ | Poor oxidation resistance @T>1400◦ C<br>Rapid volatilization of $B_2O_3$<br>Non-protective ZrO2 scale | 22 μΩ·cm @room T |
| **$HfB_2$** | Hf-B | Missing information | Similar to $ZrB_2$ | Density: ~10.5/11 g/$cm^3$ | - Melting point: 3250◦ C<br>- Thermal conductivity: ~80 W/mK<br>- CTE: ~3.5-4.5x$10^{-6}K^{-1}$ | Oxidation resistance very similar to $ZrB_2$ | 8-15 μΩ·cm @room T |

Consequently, while metallic alloys from the NiCr and FeCrAl families remain the industry standard for ductility and ease of fabrication, they are physically limited to the lower thermal range. These alloys cannot sustain structural integrity in the 1600-1800°C regime, where they inevitably face melting or accelerated creep.

Ultimately, the comparative analysis in Table 10 underscores that $MoSi_2$ provides the most balanced thermomechanical profile currently available, yet its limitations in a monolithic form create a clear technological ceiling. This provides the scientific rationale for the subsequent chapters of this thesis, which focus on composite strategies and functionally graded architectures designed to decouple electrical resistivity from mechanical fragility and environmental degradation.

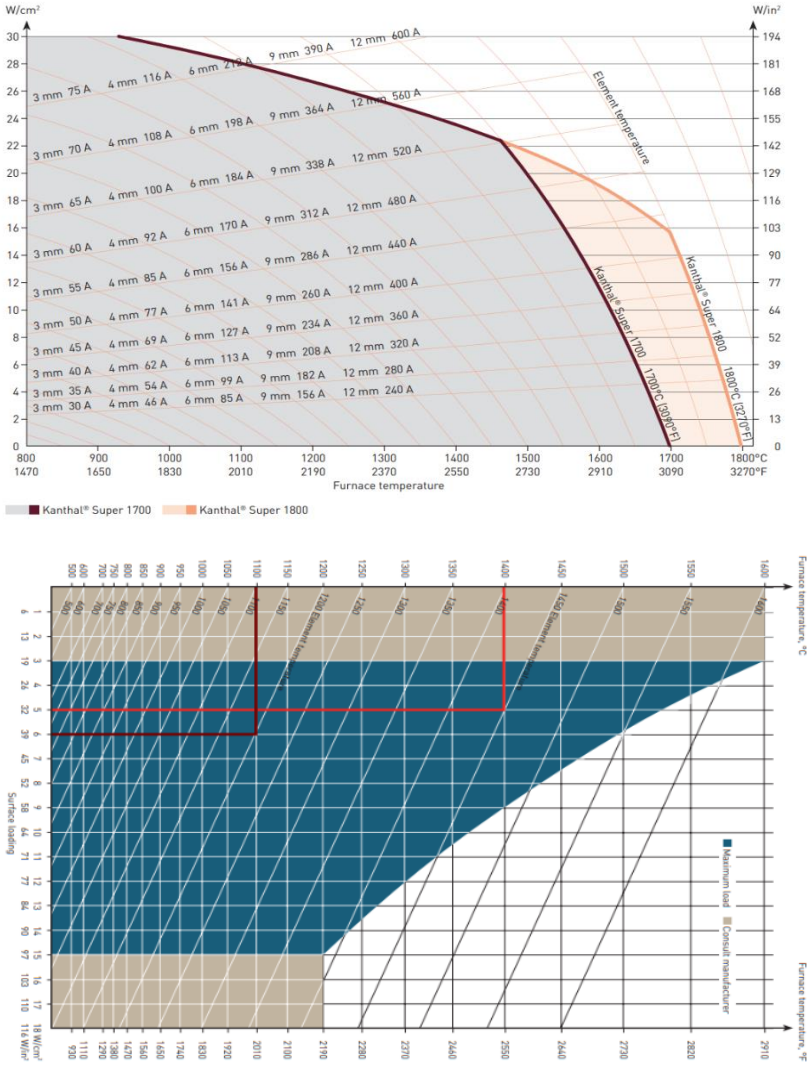


*(a)*

*(b)*

*Figure 26. Temperature loading diagram for Kanthal® Super (a) [36], Temperature loading diagram for Kanthal Globar® (b)[89]*

## 5. Performance improvement of MoSi2

The optimization of $MoSi_2$ performance can be theoretically approached through several distinct methodologies. One primary strategy involves elemental doping or the formulation of alloys with secondary elements or compounds to enhance specific target properties. These alloying strategies typically target three core performance metrics: the chemical stability of the protective oxide scale, high-temperature creep resistance, and electrical resistivity. The latter is tuned by modulating carrier concentrations and electron scattering behaviors. In practice, however, optimizing one functional property often compromises another, forcing a design compromise that balances these competing thermal, mechanical, and electrical demands.

A second methodology focuses on the precise control of microstructural architecture. As previously established, the specific fabrication route, the degree of densification, grain size distribution, and the presence of residual porosity significantly influence the measured macroscopic resistivity. These factors induce electron scattering and current-path constriction (tortuosity), even in cases where the intrinsic resistivity of the $MoSi_2$ grains remains constant. This strategy offers a practical engineering advantage: it bypasses the need for entirely new chemical phases. The challenge, however, lies in the inherent friction between mechanical robustness and oxidation resistance, which creates a narrow operational window.

A third alternative involves surface engineering, which provides a distinct pathway for optimization. Techniques such as emissivity-modulating coatings or the use of diffusion barriers can effectively govern oxide scale growth and prevent delamination by altering its adherence kinetics. This approach serves as a practical engineering lever since it does not necessitate the introduction of novel chemical phases; however, its application is fundamentally limited by the competing requirements for mechanical strength and oxidation resistance.

Finally, this study investigates an alternative paradigm: the development of composite compounds that exclude $MoSi_2$ entirely. This approach seeks to integrate various material families, as previously categorized, to leverage synergistic effects and improve the collective performance beyond the capabilities of traditional silicide-based systems.

### 5.1. Alloying / doping

Alloying and doping represent the most direct methodologies for modifying the functional behavior of $MoSi_2$ through the controlled regulation of defect chemistry and phase assembly. Substitutional alloying of Mo sites with transition metals, most notably Nb, Ta, and W$, drives the formation of solid solutions or complex heterophase architectures (C11b, C40, C54). These microstructural shifts are the primary governors of slip evolution, mechanical strength, and oxidative stability. Furthermore, replacing molybdenum with heavier elements induces a pronounced lattice distortion; this lattice strain enhances electrical resistivity, primarily through solid-solution scattering. Elements like V, Cr, Nb, and Ta, which usually form C40 disilicides, show high solubility within the $MoSi_2$ lattice and trigger a temperature-sensitive mechanical shift. This is characterized by a drop in yield strength below 800°C, followed by a strength recovery above 1300°C. Within this group, Nb-doping stands out for providing the most robust high-temperature reinforcement, while Cr-modification optimizes Si-O bonding to inhibit oxygen diffusion without compromising the underlying stoichiometry. While comprehensive $\rho(T)$ data for these specific ternary systems is somewhat limited, trends from Mo-Si-B and related silicides suggest that transition metal additions only marginally nudge room-temperature resistivity. Typically, we see shifts by factors of 1 to 3 rather than the order of magnitude jumps required for deep electrification. First principles modeling of Cr, Nb, and W doped C11b structures confirms that while bonding characteristics and elastic properties shift, the electronic density of states (DOS) near the Fermi level remains remarkably stable. This stability explains why these materials undergo minor conductivity fluctuations instead of a true metal-to-semiconductor transition. Mechanically, the effects are divergent: Cr significantly softens the elastic modulus, and W depresses the Debye temperature. In contrast, the B/G (Pugh's) and Poisson's ratios for Nb-doped $MoSi_2$ increase significantly (Figure 27), pointing toward more metallic bonding and improved fracture ductility.

Elements that form isostructural C11b phases, such as W and Re, exhibit nearly total solid solubility in $MoSi_2$. These dopants elevate yield strength across all temperatures due to their inherent hardness, yet they introduce significant drawbacks. Research into $(Mo,W)Si_2$ borides highlights a persistent vulnerability to pesting, driven by the high volatility of $WO_3$ which leaves the silica scale porous and ineffective. Beyond these chemical hurdles, the high density and prohibitive cost of W and Re make them poor candidates for large-scale structural components.

Their impact on electron transport is equally modest; $WSi_2$ maintains a metallic conductivity profile on par with $MoSi_2$, resulting in room-temperature resistivity that stays within the tens of $\mu\Omega\cdot$cm and retains a positive temperature coefficient. Ultimately, while doped molybdenum silicides remain a focal point for thermoelectric research and aero-turbine coatings, they have failed to penetrate the commercial heating element market. This lack of adoption stems from the marginal gains in functional performance when measured against baseline $MoSi_2$. More critically, these dopants often destabilize the delicate $SiO_2$ scale chemistry, inviting catastrophic oxidation and the formation of brittle, deleterious intermetallic phases.

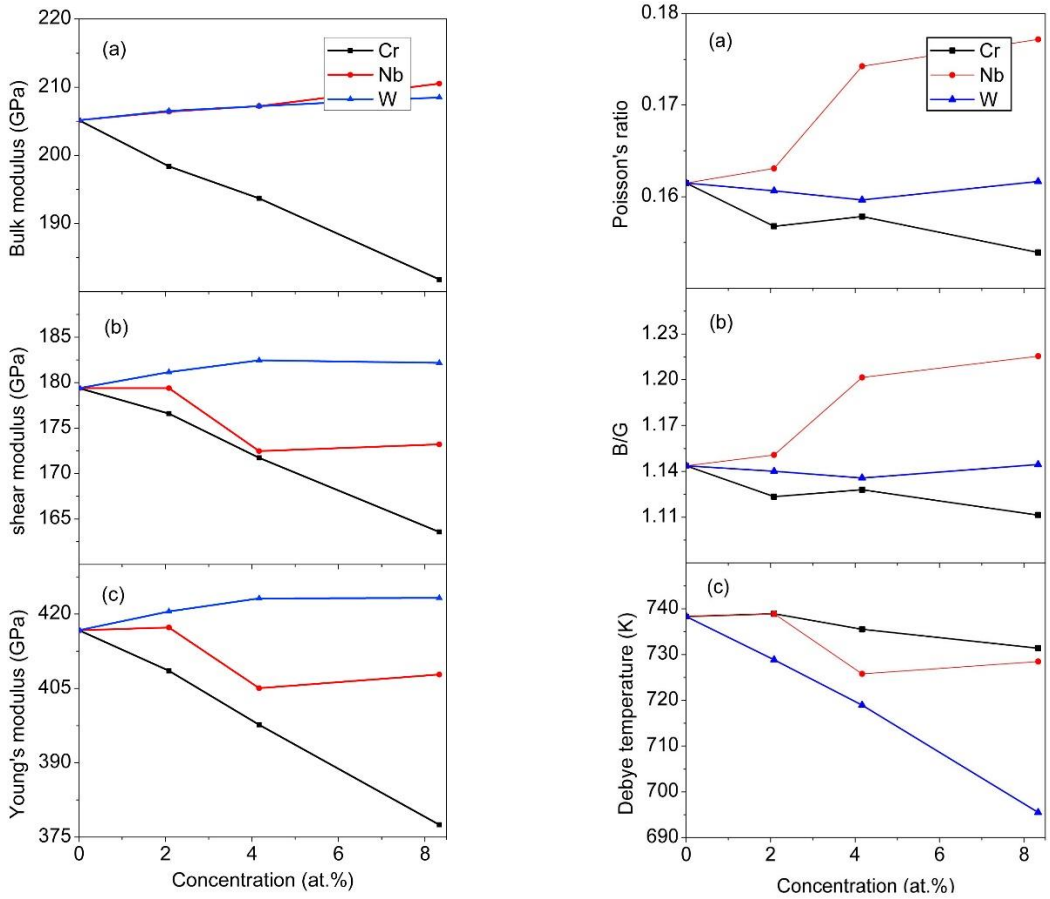


*(a)* *(b)*

*Figure 27. Calculated mechanical moduli of C11b MoSi2 doped with Cr, Nb and W (a), Calculated Poisson's ratios, B/G ratios and Debye temperatures of C11b MoSi2 doped with Cr, Nb and W [101]*

The most technologically mature strategy for property optimization involves the incorporation of discrete secondary phases into the $MoSi_2$ matrix. Of particular interest are $MoSi_2$-UHTC (Ultra-High Temperature Ceramic) composites (e.g., $ZrB_2$, $HfB_2$, SiC), typically synthesized via pressureless sintering or hot-pressing. The integration of particulate reinforcements such as

MoB, $Si_3N_4$, and SiC has been widely documented as an effective means of enhancing mechanical performance. Among these additives, the $ZrB_2$-SiC system, benchmark UHTC, has demonstrated a significant advantage in the structural strengthening of $MoSi_2$-based ceramics. Experimental investigations have characterized the properties of $MoSi_2$ across various UHTC volume fractions. The standardized processing protocol involves planetary ball-milling of $MoSi_2$-UHTC mixtures in polyethylene vessels utilizing zirconia media and ethanol as the milling fluid, followed by drying via rotary evaporation. The resulting composite powders are consolidated through uniaxial dry pressing in steel molds. Densification is achieved through pressureless sintering under an Ar atmosphere at temperatures ranging from 1700 to 1900 °C for a 1-hour dwell time within a graphite-element furnace. Sintering temperatures are adjusted accordingly to accommodate specific compositional variations in the $MoSi_2$-UHTC system.

While all $MoSi_2$-($ZrB_2$-SiC) ceramics exhibit superior mechanical strength relative to monolithic $MoSi_2$, a result of the synergistic reinforcement provided by the $ZrB_2$ and SiC phases, their room-temperature electrical resistivity follows a decreasing trend as the UHTC volume fraction increases (Figure 28). To model these transport properties, Fan et al. developed a topological transformation method for predicting the electrical resistivity of two-phase composites, which accounts for the influence of particle morphology and spatial distribution via the following derived expression:

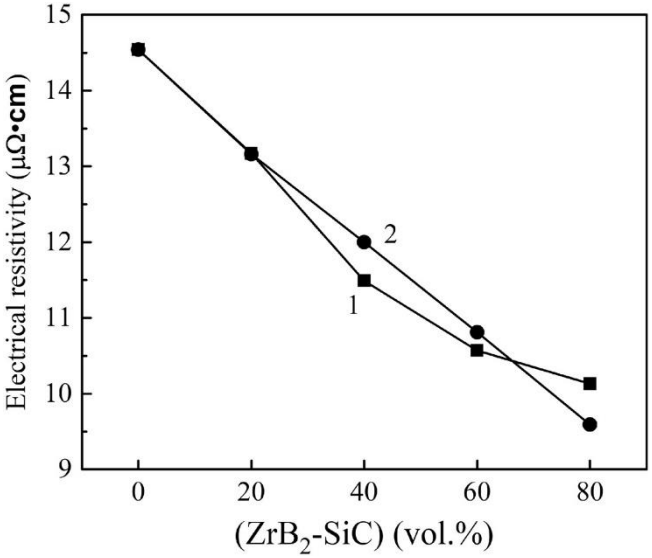


*Figure 28. Electrical resistivity vs. (ZrB2-SiC) content: 1 experimental data and 2 calculated data [15]*

$$\frac{1}{\rho} = \frac{f_\alpha{}^m}{\rho_\alpha} + \frac{f_\beta{}^n}{\rho_\beta} + \left( \frac{(1-f_\alpha{}^m - f_\beta{}^n)^2}{\rho_\alpha (f_\alpha - f_\alpha{}^m) + \rho_\beta (f_\beta - f_\beta{}^n)} \right)$$

In this model, ρ represents the bulk resistivity of the two-phase composite; ρα and ρβ denote the resistivities of the constituent phases; fα and fβ are their respective volume fractions; and m and n are constants determined by the phase distribution. In general, a highly continuous phase network tends to drive down the values of m and n. Since the goal of this study is to avoid a decrease in resistivity, the design logic must pivot in the opposite direction. There are several tactical routes to achieve this: curtailing the

overall conductive UHTC loading, replacing portions of the $ZrB_2$ phase with higher-resistivity alternatives, or intentionally diluting the matrix with SiC-rich micro-regions.

Historically, investigations into $MoSi_2$-SiC binary systems were predominantly restricted to processing methodologies and empirical mechanical benchmarking. However, recent advancements have facilitated the first synthesis of these composites via pressureless reactive sintering, coupled with a rigorous topological analysis of their electrical resistivity. This methodological evolution enables the inverse design of the composite architecture; specifically, SiC volume fractions and microstructural configurations can now be quantitatively predicted based on target electrical transport properties. Consequently, research regarding the $MoSi_2$-SiC system has transitioned from qualitative observation to a phase of strategic microstructural planning. While historical research in the $MoSi_2$-SiC binary system focused predominantly on synthesis protocols and empirical mechanical characterization, more recent advancements have introduced pressureless reactive sintering and rigorous topological analysis of electrical resistivity. This shift marks the transition from purely qualitative assessment to a rigorous microstructural planning phase. At this stage, specific target resistivity values are used to reverse engineer the necessary SiC volume fractions and phase distributions.

From a design perspective, SiC functions as a versatile, multifunctional additive; it simultaneously bolsters fracture toughness, preserves high-temperature mechanical strength, and refines oxidation kinetics. During thermal exposure, SiC participates in the development of a dense, protective $SiO_2$-SiC composite scale. Just as importantly, because SiC is far less conductive than $MoSi_2$ at typical furnace operating temperatures, its inclusion effectively drives up bulk resistivity. In many cases, increasing the SiC content triggers a semiconducting-like $\rho(T)$ profile, particularly at lower temperatures. This effect is most evident in complex systems like $Si_3N_4$-SiC-$MeSi_2$ (where Me = Mo, W, Nb), where compositions containing as little as 8 vol% silicide can reach resistivities near 10 $\Omega \cdot cm$ at room temperature, dropping to roughly 1 $\Omega \cdot cm$ at 1000°C.In such cases, the dielectric matrix ($Si_3N_4$/SiC) dominates the global transport properties, rendering the specific disilicide species a second-order influence.

However, several constraints must be considered when optimizing SiC content. Prohibitively high concentrations may entirely disrupt the $MoSi_2$ percolation network (which will be further discussed in later on), resulting in excessively high resistivity and a SiC-type thermal response that complicates power regulation during furnace operation. Tackling the challenges of

thermomechanical compatibility, specifically the discrepancies in thermal conductivity and the CTE, is vital for minimizing internal residual stress and avoiding microcracking. While the specific pairing mechanisms between $MoSi_2$ and SiC are detailed in the following section, the integration of $Al_2O_3$ into these matrices already stands out as a highly effective strategy. The chemical stability and near-perfect CTE match between these phases are instrumental in curbing thermal stresses during the cooling cycles following sintering, which directly bolsters both thermal shock resistance and long-term environmental durability. Experimental work on $MoSi_2$-$Al_2O_3$ composites, processed via pressureless sintering at 1550°C, suggests that a 20 vol% $Al_2O_3$ loading represents a sweet spot for overall performance. At this concentration, the composite generates a sophisticated $SiO_2$-$Al_2O_3$ oxide scale that acts as a formidable kinetic shield against oxygen ingress. Additionally, because maintains its dielectric integrity across a wide thermal range, its presence significantly d $Al_2O_3$ rises up room-temperature resistivity, allowing for more nuanced control over power and temperature. The data reflects a clear upward trajectory: resistivity climbs from 15 μΩ cm in monolithic $MoSi_2$ to 37.20 μΩ cm at 20 vol%, eventually reaching 75.82 μΩ cm at the 40 vol% mark (Table 11). From a microstructural standpoint, $Al_2O_3$ serves a double purpose as both a sintering aid and a structural reinforcement. Distributing these particles along $MoSi_2$ grain boundaries is essential for strengthening. While the rigid covalent bonds in $MoSi_2$ usually make pressureless densification difficult, nano scale $Al_2O_3$ provides a strong thermodynamic push for sintering, thanks to its high surface energy and specific surface area. This accelerates solid-phase kinetics, leading to a noticeable rise in relative density as the alumina fraction increases. Mechanical testing shows that hardness follows a parabolic relationship with $Al_2O_3$ content, peaking at 11.30 GPa for the 20 vol% mix. This peak is the result of optimized densification combined with significant grain refinement; the dispersed nanoparticles essentially pin the grain boundaries, preventing the $MoSi_2$ matrix from overgrowing. This refinement, alongside high relative density, is the primary driver behind the improved fracture toughness. By increasing the grain boundary density and reducing matrix size, the composite effectively obstructs crack propagation through deflection and pinning, far outperforming monolithic $MoSi_2$.

Flexural strength, a primary performance metric for structural ceramics, exhibits a positive correlation with $Al_2O_3$ concentration up to a critical threshold. The observed deterioration in strength for the M40 (40 vol%) composition is primarily attributed to residual porosity, where

pores function as critical failure nuclei. Under bending loads, these voids generate intense localized stress concentrations that facilitate crack initiation. As a result, flexural strength is largely dictated by a combination of relative density and the refined state of the microstructure. Dispersed $Al_2O_3$ nanoparticles serve as potent grain-growth inhibitors; by pinning the $MoSi_2$ grain boundaries, they effectively halt coarsening during the sintering process. This refinement creates a higher density of grain boundaries, which promotes dislocation pile-up and complex interaction mechanisms, factors that ultimately bolster the material's resistance to flexural deformation.

The oxidation kinetics tell a more complex story. In the incipient stage (below 650°C), $MoO_3$ and $SiO_2$ are generated simultaneously. However, as temperatures climb toward 800°C, the high vapor pressure of $MoO_3$ causes it to evaporate rapidly. This volatilization is dangerous; it can trigger localized porosity or even lead to the catastrophic pesting phenomenon. To preserve structural integrity, it is vital to minimize time spent within the critical 400-700°C window. During these preliminary oxidation stages, mass transport is dominated by the diffusion of Si atoms within the $MoSi_2/Mo_5Si_3$ interlayers, a process that occurs at a much faster rate than the movement of Mo atoms. It is pertinent to note that while $Al_2O_3$ influences scale formation and stability, it does not function as a kinetic diffusion barrier for silicon.

*Table 11. Physical and mechanical properties of MoSi2-Al2O3 composites [94]*

| Sample | Hardness (GPa) | Fracture toughness (MPa $m^{1/2}$) | Flexural strength (MPa) | Electrical resistivity (μΩ cm) |
|---|---|---|---|---|
| **M0** | 9.93 | 3.04 | 337.21 | 15.20 |
| **M10** | 10.50 | 3.64 | 359.95 | 24.86 |
| **M20** | 11.30 | 4.78 | 536.49 | 37.20 |
| **M40** | 8.63 | 6.05 | 275.38 | 75.82 |

The enhancement of oxidation resistance in these composites is driven by several interrelated physicochemical mechanisms. Primarily, the densification degree of the matrix is significantly improved through the auxiliary sintering effect of nano-scale $Al_2O_3$. Higher relative density is a critical determinant of oxidation performance, as it limits the pathways for internal oxidative attack. The concentration of $Al_2O_3$ directly modulates the growth kinetics of the oxide scale. In

the incipient stages, the higher density of grain boundaries provides pathways for a rapid inward flux of oxygen, which benefits the material by accelerating the formation of a continuous, passivating layer. Within this composite, the alumina remains in its α-$Al_2O_3$ allotropic state. This dense rhombohedral structure acts as a formidable kinetic barrier to oxygen transport, largely due to the massive activation energy (6.3-6.9 eV) required for vacancy formation. This stands in sharp contrast to oxygen movement through an amorphous $SiO_2$ scale, where vacancy defects facilitate transport at a much lower activation energy (1.17-1.35 eV) as seen in gas transport phenomena. This stark energy disparity highlights how α-$Al_2O_3$ suppresses the overall rate of oxygen diffusion. Additionally, the protective scale gains improved self-healing properties through modified high-temperature rheology. When minor fractions of $Al_2O_3$ dissolve into the $SiO_2$ phase, they create a eutectic system with a melting point of 1594°C, allowing the scale to flow and seal defects more effectively at extreme temperatures. This interaction reduces the softening point and viscosity of the amorphous silica, increasing its fluidity and enabling it to effectively encapsulate surface defects and bridge micro-cracks.

Finally, the thermomechanical stability of the protective scale during thermal cycling is greatly improved. Monolithic $SiO_2$ possesses an exceptionally low Coefficient of Thermal Expansion (CTE) of $0.55 \times 10^{-6}/\mathrm{K}$, which contrasts sharply with the higher CTE values of and $Mo_5Si_3$ substrates. This mismatch generates significant interfacial thermal stresses during cooling, typically resulting in scale fracture or delamination (spallation). The transition to a multi-component $SiO_2$-$Al_2O_3$ scale elevates the effective CTE of the oxide layer, thereby minimizing the thermal mismatch and enhancing the adherence and integrity of the protective film over repeated high-temperature cycles.

Also, the combustion synthesis (or self-propagating high-temperature synthesis) of SiC-$MoSi_2$-$Al_2O_3$ composites has been investigated using the highly exothermic $MoO_3$-Al-Si-$SiO_2$ reactive system. This fabrication process is driven by the aluminothermic reduction of $MoO_3$ and $SiO_2$. Within this framework, SiC is utilized as a filler material to moderate the reaction kinetics and act as a functional constituent of the heating element. Elements synthesized with approximately 60 wt% SiC exhibit high reactive conversion rates, superior net-shape fidelity, and relatively low porosity. While this study demonstrated the viability of preparing heating elements with a room-temperature resistivity of 12 Ω cm and a specific watt loading of 20

W/cm² at 1500 °C, the approach is deemed suboptimal for the present study due to the relatively high residual porosity and an upper service temperature limited to 1500 °C.

Furthermore, the incorporation of metallic second phases was evaluated. As predicted by transport theory, these refractory metals possess higher electrical conductivity than $MoSi_2$; consequently, the formation of any continuous metallic network triggers a detrimental drop in bulk resistivity. The potential for mechanical toughening via these additions is similarly restricted. Beyond the electrical trade-offs, metals such as Nb and W oxidize more rapidly than the disilicide matrix. This differential oxidation rate threatens the structural integrity of the passivating scale unless these metallic phases are completely encapsulated within the matrix.

In addition to alumina, the analysis covered various oxide and nitride dispersions, typically ranging from 5 to 20 vol% at the nano-to-micro scale. This group includes additives such as $ZrO_2$/$HfO_2$, $Si_3N_4$/$Si_2N_2O$, and $Ta_2O_5$/$Y_2O_3$. While these dispersions rarely trigger transformative leaps in the material's baseline properties, they serve as effective tuning knobs for the parametric adjustment of electrical resistivity, creep resistance, fracture toughness, and oxidation kinetics.

Lastly, a metallurgical route involving MoB and $Mo_5Si_3$ additions was investigated. While these phases successfully promote grain refinement, they also lead to thicker oxide scales and higher cyclic oxidation rates at 1400°C. Because these outcomes compromise both mechanical performance and long-term environmental stability, this specific alloying path is a less viable solution for high-performance heating element applications compared to the composite strategies discussed previously. [15][56][91][92][93][94][95][96][97][98][99][100][101]

### 5.2. Manufacturing routes

As previously established, the microstructural evolution, and consequently the macroscopic properties of the final product, is fundamentally dictated by the selected manufacturing route. The conventional industrial baseline for $MoSi_2$-based components typically follows a standardized processing sequence:

- Powder preparation: comminution and homogenization via ball milling of $MoSi_2$ powders and requisite additives.
- Shaping: fabrication of green bodies through extrusion (optimized for high-aspect-ratio geometries) or Cold Isostatic Pressing (CIP), followed by green machining.

- Thermal processing: controlled debinding to remove organic binders.
- Densification: pressureless sintering for standard applications, or Hot Pressing (HP)/Hot Isostatic Pressing (HIP) when near-theoretical density is mandatory.

For enhanced microstructural refinement, Spark Plasma Sintering (SPS) is utilized. This field-assisted technique effectively inhibits grain growth and facilitates the retention of fine, discrete second phase networks, making it particularly suitable for $MoSi_2$ composites and laminated architectures. However, SPS is subject to significant scalability constraints, primarily regarding die dimensions and the maintenance of isothermal conditions across large volumes, which complicates the production of meter long elements. While SPS remains an indispensable tool for initial alloy design and protocol optimization, the path toward industrial scaling inevitably necessitates a shift toward extrusion and conventional sintering. Reactive synthesis routes offer an alternative for achieving refined microstructures and superior interfacial bonding; however, these pathways are fraught with complex reaction kinetics. In large-scale components, these kinetics often trigger significant thermal gradients, leading to residual porosity or the localized nucleation of brittle phases that can compromise bulk integrity.

Central to understanding these microstructural transitions is the phenomenon of percolation, the emergence of long-range connectivity within a multiphase material (Figure 29). Specifically, percolation theory identifies the conditions under which a discrete phase coalesces into a continuous network as its volume fraction, $\phi$, reaches a critical value ($\phi_c$). In the context of these composites, $\phi_c$ represents the precise transition point where a single cluster of the filler phase spans the entire sample, effectively unlocking the global transport of electrons, phonons, or fluids. In the sub-percolative regime ($\phi < \phi_c$), the secondary phase is trapped in isolated, finite clusters, leaving the host matrix to dominate macroscopic transport. Under these conditions, electrical conduction is limited to short-range mechanisms, such as quantum tunneling or hopping between adjacent particles. However, once the volume fraction crosses the $\phi_c$ threshold, the formation of an infinite conductive cluster triggers a precipitous collapse in resistivity, a shift that often spans several orders of magnitude. In this post-percolative regime, current flow is primarily localized within the continuous high-conductivity network, whereas below the threshold, resistivity remains high and typically exhibits a smooth, near exponential dependence on filler loading.

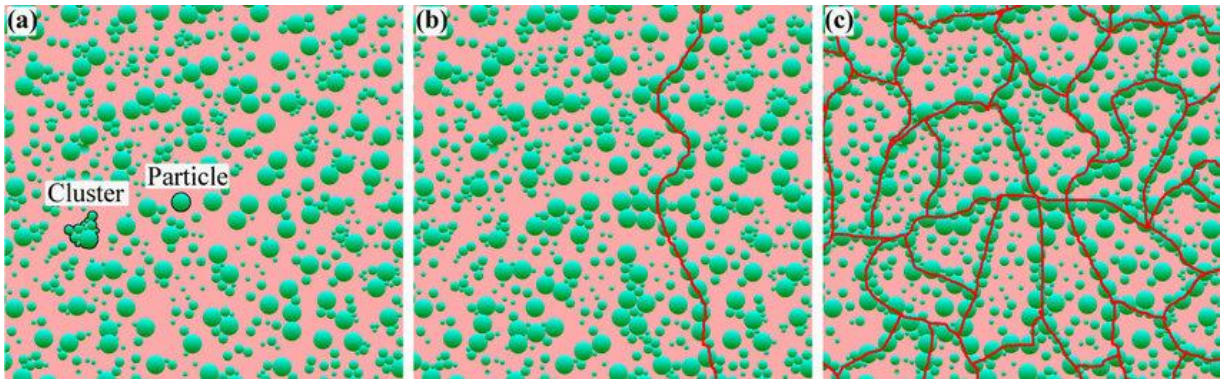


*Figure 29. Percolation behaviour in an insulating matrix-conductive filler composite. (a) Isolated clusters, (b) Percolation threshold, (c) Conductive network [113]*

The application of percolation theory provides a robust framework for tailoring the functional properties of $MoSi_2$-based systems incorporating secondary phases such as SiC, borides ($ZrB_2$, $HfB_2$), or alternative silicides. By manipulating the connectivity of these phases, several critical performance metrics can be optimized:

- Electrical resistivity: elevating macroscopic resistivity hinges on the intentional suppression of a continuous, high-conductivity $MoSi_2$ pathway. This can be executed through two primary tactical routes: either by forcing the $MoSi_2$ volume fraction below its percolation threshold ($\phi_c$) via fragmentation with insulating blocking phases, or by intentionally increasing junction resistance through the engineering of narrow inter-particle necks and high interfacial densities. By strategically incorporating fine insulating particles at loadings that approach, but strictly do not exceed, their own $\phi_c$, it becomes possible to maximize interface-induced scattering without accidentally establishing a parallel conductive network that would undermine the resistive goals.
- Mechanical integrity: it requires a similar level of spatial control. The percolation of highly brittle phases must be strictly limited to prevent the emergence of a continuous, low-energy fracture path that would compromise the bulk material. In scenarios where such a microstructural skeleton is unavoidable, the focus must shift to interfacial strength and the precise matching of CTE. These factors are paramount for mitigating the internal residual stresses that otherwise facilitate crack propagation.
- Thermal management: tuning the percolation of high thermal conductivity (k) versus low k phases allows for the strategic direction of thermal gradients. This ensures that

critical zones receive adequate heat dissipation without compromising the network's fracture toughness or increasing its susceptibility to thermal shock.

The sensitivity of these properties is mathematically defined by the scaling law $\sigma \propto (\phi - \phi_c)^t$, where the conductivity $\sigma$ increases rapidly above the threshold. Below $\phi_c$, the conductive phase exists as isolated clusters, resulting in high resistivity. Immediately above $\phi_c$, the emergence of a high-tortuosity, nascent network causes a collapse of orders of magnitude in resistivity. The non-linear performance shifts observed in $MoSi_2$-SiC-$Al_2O_3$ systems mirror this phenomenon, where property inversions correlate precisely with the volumetric crossing of the percolation threshold. To address the mechanical stresses that often accompany such phase transitions, Functionally Graded Materials (FGMs) offer a sophisticated architectural solution.

Subject to intense research since the mid-1980s, FGMs are defined by a deliberate, spatial graduation in composition or microstructure. For high-temperature applications, this approach sidesteps the inherent weaknesses of discrete, bonded multiphase laminates. By replacing sharp interfaces with a quasi-continuous transition between phases, FGMs effectively neutralize the thermomechanical disparities caused by CTE mismatches. Spreading the compositional shift across a broader volume allows the material to dissipate localized thermal stress concentrations, significantly lowering the risk of interfacial delamination and catastrophic structural failure.

The fabrication of FGMs presents a substantial technological challenge, generally categorized into two primary methodologies:

- Constructive processes: these involve the discrete physical assembly or layering of constituent phases to establish a macroscopic gradient.
- Transport-based processes: these rely on kinetic phenomena, such as heat or mass transfer, to induce a compositional or structural gradient within a precursor.

A prevalent and relatively straightforward constructive technique involves the sequential stacking and compaction of pre-mixed homogeneous layers. By minimizing the compositional increments between adjacent layers, the material can approximate a continuous gradient, effectively driving interfacial stresses down to negligible levels. Historically, such architectures were built using pre-synthesized composite powders that were only subsequently consolidated via high-temperature sintering. However, current manufacturing techniques have shifted toward a more integrated strategy: the concurrent reactive synthesis and densification of FGMs directly from their elemental reactants. This reactive processing route is particularly compelling for the

$MoSi_2$-SiC systems analyzed earlier. Modern research underscores the unique efficacy of Field-Assisted Sintering Techniques (FAST), most notably SPS, in facilitating this transition. In this setup, synthesis and consolidation occur simultaneously within a graphite die under uniaxial pressure and a high-intensity electric current. The rapid reaction and densification kinetics are not accidental; they stem from a synergy of phenomena, including localized Joule heating, enhanced mass transport through electromigration, and the potential for dielectric breakdown at particle contact points. The ability of this method to merge synthesis and densification into a single, efficient thermoelectrical cycle has been empirically confirmed for both monolithic and nanostructured materials. Experimental configurations have successfully spanned the full spectrum from 100% $MoSi_2$ to 100% SiC. As evidenced in Figure 30, the microstructural transition in a five-layer $MoSi_2$-SiC system highlights the precision of this technique. By utilizing 10 vol% $MoSi_2$ increments between adjacent layers, covering a range from 50% to 90% $MoSi_2$, this specific configuration produced a cohesive, functionally graded architecture with exceptional structural integrity.

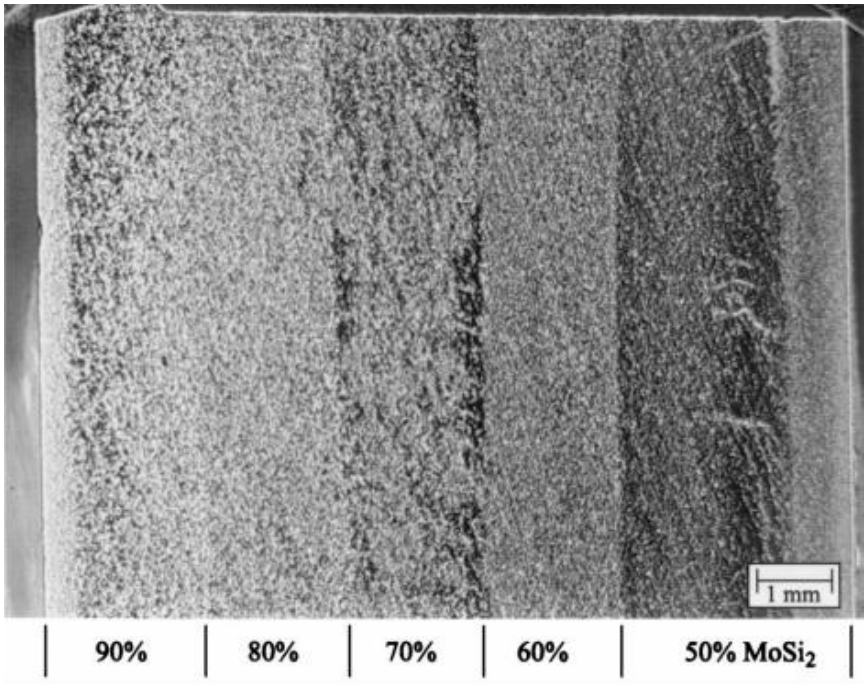


*Figure 30. Optical image of a five-layer FGM [110]*

Experimental characterization revealed that the relative density is inversely proportional to the SiC fraction, declining from approximately 99% for monolithic $MoSi_2$ to 76% for pure SiC. Similarly, the Young's modulus exhibited a monotonic decrease as the SiC content was

augmented. In contrast, Poisson's ratio remained largely invariant up to a SiC concentration of approximately 50%, beyond which a marginal reduction was observed (Figure 31).

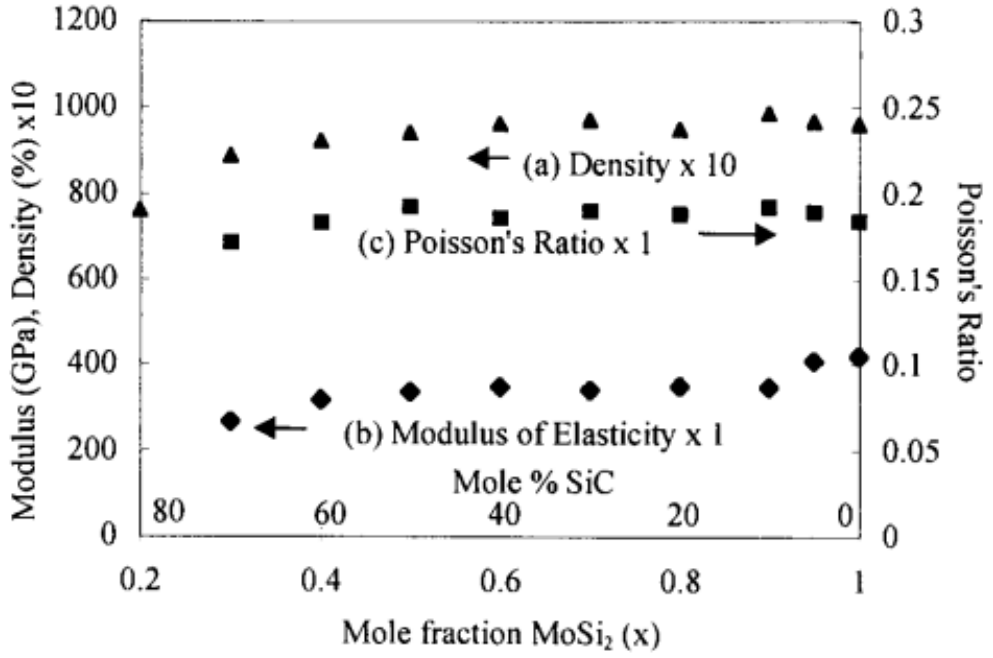


*Figure 31. (a) Density, (b) Modulus of elasticity, (c) Poisson's ratio [110]*

Experimental observations indicate that the compositional increment between adjacent layers is a critical design parameter for mitigating residual stresses. Specifically, bi-layer configurations with a compositional step exceeding 10 mol% $MoSi_2$/SiC exhibit catastrophic failure upon removal due to excessive thermal stresses. Conversely, a five-layer architecture spanning the full compositional range with approximately 10 mol% increments effectively prevent the formation of thermal stress induced cracks. This highlights the ability of Functionally Graded Material (FGM) architectures to decouple orthogonal performance requirements across the cross section or length of an element. By implementing gradual transitions in the Coefficient of Thermal Expansion (CTE) and elastic modulus, thermal stresses arising from significant temperature differentials ($\Delta T$) are distributed across the volume, thereby reducing the risk of surface fissuring or interfacial delamination.

From a functional perspective, the spatial modulation of the $MoSi_2$-to-SiC ratio allows for the precise tailoring of electrical and thermal profiles:

- Conductivity tuning: the development of a high-conductivity $MoSi_2$ core integrated with resistive outer layers facilitates a redistribution of current density, which can effectively flatten radial temperature gradients. Alternatively, a resistive core surrounded by a

conductive skin can be utilized to ensure isothermal surface profiles in specific geometries.

- Resistivity control: for the specific objectives of this study, maintaining a $MoSi_2$-dominant core preserves the primary resistive pathway, while grading with SiC or $Al_2O_3$ near the surface allows for a localized increase in resistivity. When integrated with percolation theory, this strategy permits an overall increase in effective bulk resistivity and allows for cross-sectional adjustments without overstressing the core.
- Oxidation resistance: in oxidizing environments, the FGM configuration is constrained by surface chemistry. In $MoSi_2$–SiC systems, the SiC phase provides supplementary $SiO_2$ for scale formation, maintaining an upper service limit of approximately 1700 °C, provided the $MoSi_2$-rich regions remain protected. In oxide-reinforced systems ($MoSi_2$–$Al_2O_3$), the incorporation of $Al_2O_3$ in the surface adjacent regions is particularly effective at suppressing pest oxidation and stabilizing surface morphology at intermediate temperatures.

The translation of FGM designs into high-aspect-ratio geometries, such as the rod-shaped configurations (U-shaped or straight) standard in commercial heating elements, represents a significant engineering frontier. Such geometries can be realized through centrifugal processing, multi-step powder metallurgy with controlled layering or, most notably, additive manufacturing (AM). AM techniques offer superior flexibility for prototyping and the realization of complex spatial gradients:

- Directed Energy Deposition (DED): methods such as Laser Directed Energy Deposition (LDED) or Wire-Arc Additive Manufacturing (WAAM) allow for the dynamic adjustment of powder feed ratios ($MoSi_2$:SiC) during the build process. This enables both axial grading and, through substrate rotation, radial grading.
- Powder Bed Fusion (PBF): techniques like Selective Laser Melting (SLM) or Electron Beam Melting (EBM) permit layer by layer compositional control via multi powder recoating systems. While powder mixing homogeneity remains a challenge, PBF is highly feasible for small diameter components (<20 mm).

Despite the theoretical and experimental advantages, commercial implementation of these advanced manufacturing routes remains limited. Further research and technological refinement are required to address the challenges of microstructural homogeneity and industrial scalability

in the production of functionally graded $MoSi_2$-based heating elements. [32][110][111][112][113]

### 5.3. Surface engineering

Surface engineering of $MoSi_2$-based heating elements offers a pragmatic route for enhancing spectral emissivity and oxidation stability. While these modifications can induce a modest increase in "apparent" resistivity, primarily through the modulation of surface current-path geometry, they do not fundamentally alter the bulk resistivity in the manner of a core compositional redesign.

The development and selection of these coatings are dictated by uncompromising thermomechanical requirements, most notably the need to eliminate mismatches that threaten interfacial integrity. Despite extensive research into coating alternatives, many candidates fail to bridge the gap between laboratory performance and the rigorous demands of industrial-scale implementation. From a functional perspective, the most compelling advantage of surface modification is the enhancement of radiative heat transfer. Engineered coatings and composites, (such as the $MoSi_2$-$ZrO_2$-borosilicate glass system) can push emissivity values beyond 0.9 in the near and mid-infrared spectra. This shift dramatically increases radiative power output without requiring a higher operating temperature. While a variety of systems have been tested for thermal protection, including SiC, transition metal oxides ($\gamma$-$Al_2O_3$, $TiO_2$, $ZrO_2$), and rare-earth oxides ($CeO_2$) monolithic coatings often fall short. They rarely possess the full package of properties needed for extreme service, such as the ability to provide robust oxidation shielding while simultaneously surviving the stresses of rapid thermal cycling.

Consequently, the design of multiphase coatings has emerged as a superior strategy. These systems typically comprise a crystalline emissive agent and a glass-phase binder designed to provide high bond strength and CTE compatibility with the substrate. In this context, pure $SiO_2$ glass is often unsuitable due to inadequate wetting and viscosity characteristics, while $B_2O_3$ suffers from rapid volatilization at elevated temperatures. Thermally stable borosilicate glass offers a more practical compromise, yet historical $MoSi_2$-borosilicate systems, despite reaching an emissivity of 0.8, remained prone to cracking under cyclic thermal loads. Integrating $ZrO_2$ into these architectures effectively mitigates these shortcomings. As a reinforcing phase, $ZrO_2$ provides a physical block against oxygen ingress, thereby curbing pest oxidation. Moreover, its

high melting point and strong high-temperature spectral emissivity are bolstered by its reaction with $SiO_2$ to produce zircon ($ZrSiO_4$), a chemically resilient silicate known for its excellent infrared properties. To push the system's reliability even further, the inclusion of $SiB_6$ introduces a critical self-healing function. Upon oxidation, $SiB_6$ generates a localized borosilicate flux that hermetically seals micro-cracks and surface defects, significantly boosting both thermal shock resistance and oxidative stability. Ultimately, the engineering of a $MoSi_2$-$ZrO_2$-borosilicate-$SiB_6$ multiphase system reflects a sophisticated, holistic approach to surface modification for high-performance heating elements. By pairing $ZrO_2$ for radiative power with $SiB_6$ for its autogenous healing capacity, this design sidesteps the traditional trade-off between high emissivity and mechanical durability. This integrated architecture offers a rugged solution for maintaining surface integrity under severe thermal gradients, effectively translating laboratory-scale concepts into viable industrial applications. [54][96][98][100]

### 5.4. New compounds and composites without MoSi

While $MoSi_2$-based systems are prevalent, the search for materials capable of exceeding 1800°C has led to extensive research into other Ultra-High Temperature Ceramics (UHTCs), primarily the $ZrB_2$-SiC system. This transition is motivated by the need for enhanced structural stability and oxidation resistance in extreme environments. The $ZrB_2$-SiC binary system has been recognized for its potential in ultra-high temperature structural applications since the mid-20th century. The synergy between these phases was first identified in 1956, when researchers pioneered the use of 30 wt% $ZrB_2$ to improve the thermal shock resistance of SiC. This relationship was reciprocated in 1966, as subsequent studies demonstrated that SiC additions (up to 20 vol%) could drastically curtail the oxidation rates of $ZrB_2$. Since those foundational findings, the literature has converged on a 20-30 vol% SiC concentration as the optimum quantity for balancing oxidation resistance, fracture toughness, and hardness. However, the precise efficacy of this window is heavily contingent upon the degree of phase interconnectivity and the specific particle size distribution of the starting powders.

The primary challenge in utilizing $ZrB_2$-SiC composites lies in their fabrication. Their high melting points and strong covalent bonding result in low self-diffusion coefficients, making densification difficult. Consequently, a wide array of advanced consolidation techniques has been employed, including hot-pressing (HP), spark plasma sintering (SPS), and additive

manufacturing methods such as direct ink writing (DIW) and binder jetting. Sintering aids are frequently employed to drive liquid-phase densification and reduce processing temperatures. However, their selection requires a delicate trade-off between ease of fabrication and the resulting high-temperature mechanical integrity. The exceptional oxidative stability of $ZrB_2$-SiC stems from the development of a protective borosilicate glass scale. In contrast to pure boria, this borosilicate phase possesses a higher viscosity, reduced vapor pressure, and a superior melting point, all of which combine to form a more robust kinetic barrier against oxygen ingress. A persistent challenge, however, is the emergence of a SiC-depleted zone directly beneath the oxide layer, a feature that often triggers mechanical instability or delamination. Emerging data suggests that ZrC additions can counteract this degradation. Under extreme thermal loads (exceeding 2000°C), ZrC expands volumetrically as it converts to $ZrO_2$, effectively filling the pores within the SiC-depleted region. Despite such microstructural fixes, the system faces a hard physical boundary at approximately 2066°C. At this threshold, the evolution of gaseous reaction products forces a transition from passive to active oxidation, marking a fundamental limit for these ceramics. It is important to note that a significant thermal gradient often exists between the surface and the reaction interface, meaning the local chemistry may be governed by temperatures lower than the nominal surface temperature.

The thermal conductivity of $ZrB_2$-SiC composites generally exceeds that of monolithic polycrystalline $ZrB_2$ (~85 W/(mK)). Depending on the SiC morphology and purity, the thermal conductivity of a $ZrB_2$-30 vol% SiC composite is predicted to range between 96 and 143 W/(mK). Electrically, the composite behaves as a classic conductor-insulator system. $ZrB_2$ maintains high, metallic-like conductivity, while SiC functions as a semi-conductor. This disparity means the bulk resistivity of the ceramic is essentially a function of the SiC volume fraction; as the SiC content grows, the resistivity follows an upward trajectory (Figure 32). The rising fraction of SiC also creates a higher density of $ZrB_2$-SiC grain boundaries, which act as physical bottlenecks for electron transport. This cumulative impedance explains why the $ZrB_2$-30SiC formulation consistently exhibits the highest resistivity among standard compositions. Similar trends in both thermal and electrical transport are observed in the $HfB_2$-SiC system.

$LaCrO_3$-based composites represent an alternative class of heating elements, primarily utilized in laboratory scale equipment since the 1970s. Unlike $MoSi_2$, $LaCrO_3$ does not undergo significant aging (resistance increase) over time and can operate up to 1800°C.

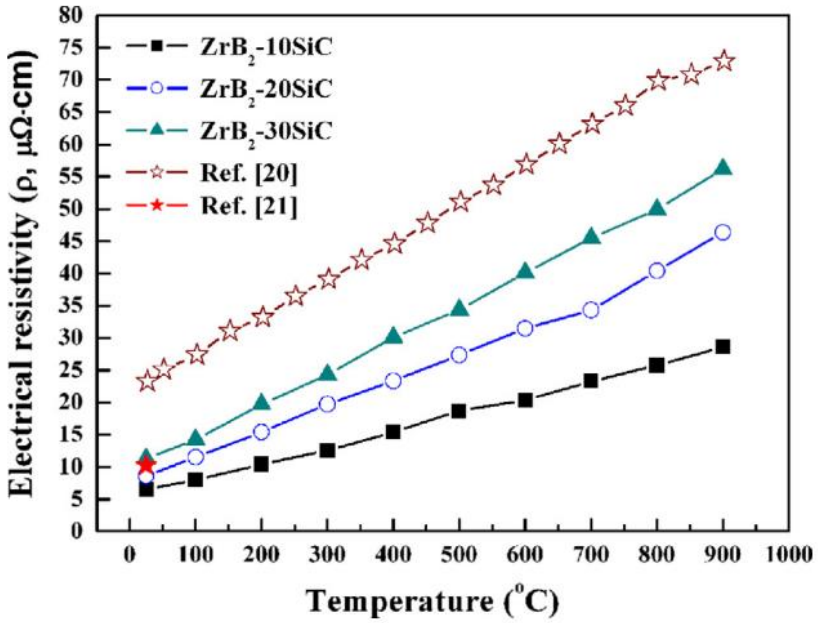


*Figure 32. Electrical resistivity of ZrB2-SiC composites [105]*

However, its application is limited by several technical and environmental drawbacks:

- Thermal and mechanical sensitivity: it exhibits high sensitivity to thermal shock and poor mechanical strength, often requiring vertical mounting at temperatures above 1200°C.
- Electrical characteristics: the material exhibits a Negative Temperature Coefficient (NTC). This inverse relationship, where resistance drops as the temperature increases, demands the use of specialized power supplies to mitigate the constant threat of thermal runaway.
- Environmental and health risks: once temperatures exceed 1600°C, chromium sublimation begins to occur. This volatilized chromium trioxide then reacts with atmospheric moisture to produce hexavalent chromium [Cr(VI)], a notorious and highly potent carcinogen. This chemical transition does more than just pose a health risk; it actively contaminates both the furnace elements and the processed materials. Consequently, any spent heating elements or degraded insulation must be handled as hazardous waste, significantly increasing the long-term operational costs and regulatory burden.

While $LaCrO_3$ was once preferred for niche applications like optical fiber splicing due to its formability into complex, miniature shapes, it is increasingly being superseded by

modern $MoSi_2$ and SiC prototypes which offer superior safety profiles and performance metrics. [85][102][103][104][105][106][107][108][109]

# 6. Conclusions

## 6.1. Comparative synthesis and key findings

This investigation has provided a critical assessment of the scalability limits inherent to molybdenum disilicide-based radiative heating elements, specifically addressing the requirement for higher power densities in industrial electrification. The central finding of this thesis is the confirmation of the resistivity paradox: while $MoSi_2$ offers superlative oxidation resistance at 1700-1800°C, its metallic-like electronic conduction results in an intrinsic resistivity that is too low for high voltage, multi megawatt scaling. This low resistivity necessitates the use of thin, mechanically vulnerable geometries to achieve the target electrical resistance, which in turn exacerbates susceptibility to fracture and dislocation climb-assisted creep.

The systematic benchmarking of candidate materials and architectural strategies has yielded the following key findings regarding resistivity modulation:

- Intrinsic limitations of the $MoSi_2$ benchmark: $MoSi_2$ remains the optimal balance for high-temperature stability due to its hybrid bonding character. However, its low resistivity creates a "technological ceiling" for electrification. To handle large electrical loads while limiting current levels, the operating voltage must be increased, a requirement that is directly hindered by the material's high conductivity.
- Solid-solution doping vs. charge transport: substitutional alloying of Mo sites with transition metals (Na, Ta, W, Cr) increases resistivity through solid-solution scattering mechanisms. However, this study found that such modifications only induce marginal shifts (factors of 1-3) and often come at the cost of destabilizing the passivating $SiO_2$ layer or promoting pest oxidation. Consequently, doping alone is insufficient to meet the resistivity requirements for high power industrial scaling.
- Composite strategies and percolation management: the incorporation of discrete secondary phases emerged as the most efficacious route for resistivity enhancement. The addition of dielectric reinforcements, such as $Al_2O_3$ or SiC, allows for the tailoring of the bulk resistivity by managing the percolation threshold ($\phi_c$). Empirical data confirmed that $MoSi_2$-$Al_2O_3$ composites can effectively double the room-temperature

resistivity (from 15 $\mu\Omega \cdot$ cm to 37.20 $\mu\Omega \cdot$ cm at 20 vol%) while simultaneously improving fracture toughness.

- Functionally Graded Materials (FGMs) as a resistivity solution: the transition from monolithic phases to FGMs ($MoSi_2$-SiC) represents a superior paradigm for decoupling resistivity from mechanical fragility. By spatially modulating the silicide-to-carbide ratio, it is possible to create a high resistivity surface region that facilitates localized heat generation and higher bulk resistance without compromising the continuity of the structural conductive backbone. This approach mitigates the thermal expansion mismatch (CTE) stresses that typically lead to delamination in discrete multi-phase systems.

In conclusion, the challenge of high-power electrification resides not in a lack of refractory candidates, but in the necessity for integrated electro-thermo-mechanical optimization. Microstructural design and composite architecture are the decisive factors in overcoming the low-resistivity bottleneck of traditional silicides.

### 6.2. Limits of the study and recommendations for further research

While this research establishes a scientific rationale for the development of next-generation heaters, several limits persist that warrant further investigation, particularly regarding the temporal and thermal evolution of resistivity:

- High temperature resistivity characterization: a primary limitation of this study is the paucity of high-fidelity, long-term resistivity data for complex composite systems at service temperatures exceeding 1500 °C. While initial models suggest stable transport properties, the impact of grain coarsening and secondary phase precipitation on carrier mobility over thousands of operational hours remains an unknown variable.
- Scale-up of resistivity gradients: the most promising resistivity tuning architectures identified (FGMs and nanostructured composites) were synthesized via Spark Plasma Sintering (SPS). While SPS provides exceptional control over microstructural architecture, it faces significant industrial scalability constraints for the production of meter-long heating elements. Transitioning these precise resistivity profiles to scalable manufacturing routes like extrusion or Directed Energy Deposition (DED) is a critical next step.

- Environmental impact on apparent resistivity: while surface engineering can modulate emissivity, the impact of oxide scale thickness on the "apparent" resistivity of thin elements was not fully quantified. As the $SiO_2$ or $SiO_2$-$Al_2O_3$ scale grows during service, the effective conductive cross section decreases, leading to aging (a progressive increase in resistance) that complicates power regulation.

Recommendations for further research are then:

- Dynamic resistivity modeling: future studies should develop predictive models that account for the evolution of resistivity as a function of both temperature and time (oxidative aging), specifically for hybrid $MoSi_2$-UHTC systems.
- Additive manufacturing of graded profiles: research should focus on Laser Directed Energy Deposition (LDED) to dynamically adjust powder feed ratios ($MoSi_2$:SiC) during the build process. This would allow for the fabrication of complex radial and axial resistivity gradients in high-aspect-ratio geometries.
- In situ thermoelectrical testing: it is recommended to perform in situ characterization of the percolation network under high-voltage stress to ensure that resistivity enhancing blocking phases do not lead to localized current crowding or dielectric breakdown at high power densities.

## References

*The author acknowledges the use of artificial intelligence (AI) tools during the preparation of this thesis. Specifically, these technologies were utilized to support the identification of relevant literature and sources, as well as to assist in the structural adjustment, linguistic refinement, and grammatical correction of the technical manuscript. All sources provided were manually verified for accuracy and relevance.*


[1] Future Cleantech Architects. (2024, October). *Decarbonizing high-temperature heat in industry: Technology assessment and policy recommendations for Europe*. https://fcarchitects.org

[2] GeoEnergy, T., & Richter, A. (2017, November 10). Geothermal and industrial heat demand—New IEA report on the role of heat | ThinkGeoEnergy—Geothermal News & Insights. https://www.thinkgeoenergy.com/geothermal-and-industrial-heat-demand-new-iea-report-on-the-role-of-heat/

[3] World Energy Outlook-2017. (2017).

[4] Rosenow, J., Arpagaus, C., Lechtenböhmer, S., Oxenaar, S., & Pusceddu, E. (2025). The heat is on: Policy solutions for industrial electrification. Energy Research & Social Science, 127, 104227. https://doi.org/10.1016/j.erss.2025.104227

[5] Decarbonizing Industrial Heat- an important puzzle piece to solving climate change. (n.d.). https://www.cleantechforeurope.com/news/decarbonizing-industrial-heat-an-important-puzzle-piece-to-solving-climate-change?utm_source=chatgpt.com

[6] MoveEnergy. (2025, October 6). Electrical heat as the next frontier in industrial decarbonisation. Move Energy. https://moveenergy.vc/electrical-heat-as-the-next-frontier-in-industrial-decarbonisation/

[7] R Kemna, MV Elburg - European Commission, 2002, Heat from renewable energy sources. The RES-H initiatives and related directives

[8] Why industrial heating must go electric. Now—Kanthal®. (n.d.). https://www.kanthal.com/en/knowledge-hub/inspiring-stories/why-industrial-heating-must-go-electric.-now

[9] Electrical heating fundamentals. (1982). In The Efficient Use of Energy (pp. 94–114). Elsevier. https://doi.org/10.1016/B978-0-408-01250-8.50016-7

[10] Ganji, D. D., Sabzehmeidani, Y., & Sedighiamiri, A. (2018). Radiation Heat Transfer. In Nonlinear Systems in Heat Transfer (pp. 105–151). Elsevier. https://doi.org/10.1016/B978-0-12-812024-8.00003-5

[11] NEM Energy B.V. (2024). Electrification of heat.

[12] Andersen, O. K., Jepsen, O., Antonov, Vl. N., Antonov, V. N., Yavorsky, B. Yu., Perlov, A. Ya., & Shpak, A. P. (1995). Fermi surface, bonding, and pseudogap in MoSi2. Physica B: Condensed Matter, 204(1–4), 65–82. https://doi.org/10.1016/0921-4526(94)00245-Q

[13] Arvanitis, A., Diplas, S., Tsakiropoulos, P., Watts, J. F., Whiting, M. J., Morton, S. A., & Matthew, J. A. D. (n.d.). TO 40 at% Al) VIA AUGER PARAMETER SHIFTS AND CHARGE TRANSFER CALCULATIONS.

[14] chemtalk. (2021, February 7). The Marvelous Element Molybdenum | Periodic Table. ChemTalk. https://chemistrytalk.org/molybdenum-element/

[15] He, R., Tong, Z., Zhang, K., & Fang, D. (2018). Mechanical and electrical properties of MoSi2-based ceramics with various ZrB2-20 vol% SiC as additives for ultra high temperature heating element. Ceramics International, 44(1), 1041–1045. https://doi.org/10.1016/j.ceramint.2017.10.043

[16] Kanthal Handbuch: Heizleiterlegierungen für elektrische Geräte und Anlagen in Haushalt, Gewerbe und Industrie. (1995). Kanthal.

[17] Kovbashyn, V., & Bochar, I. (2022). The study of technological peculiarities for improvement of chemical and physico-mechanical properties of reaction-sintered ceramic materials based on molybdenum disilicide. Scientific Journal of the Ternopil National Technical University, 2(106), 39–46. https://doi.org/10.33108/visnyk_tntu2022.02.039

[18] Liu, Y. Q., Shao, G., & Tsakiropoulos, P. (2001). On the oxidation behaviour of MoSi2. Intermetallics, 9(2), 125–136. https://doi.org/10.1016/S0966-9795(00)00114-X

[19] Matsuo S., & Homma K. (1964). Spectral Emissivity of Molybdenum Disilicide. Journal of the Ceramic Association, Japan, 72(824), 115–118. https://doi.org/10.2109/jcersj1950.72.824_115

[20] Mohamad, A., Ohishi, Y., Muta, H., Kurosaki, K., & Yamanaka, S. (2018). Thermal and Mechanical Properties of α-MoSi2 as a High-Temperature Material. Physica Status Solidi (b), 255(4), 1700448. https://doi.org/10.1002/pssb.201700448

[21] Molybdenum disilicide. (2025). In Wikipedia. https://en.wikipedia.org/w/index.php?title=Molybdenum_disilicide&oldid=1290233844

[22] Molybdenum Facts, Symbol, Discovery, Properties, Uses. (n.d.). https://www.chemistrylearner.com/molybdenum.html

[23] Molybdenum—Element information, properties and uses | Periodic Table. (n.d.). https://periodic-table.rsc.org/element/42/Molybdenum

[24] Schupp Ceramics—MolyCom®-Hyper. (n.d.). https://www.schupp-ceramics.com/en/electric-heating/hochreine-molybdaendisilizid-heizelemente-mosi2-molycom-hyper.html

[25] Silicon Facts, Symbol, Discovery, Properties, Common Uses. (n.d.). https://www.chemistrylearner.com/silicon.html

[26] Silicon—Element information, properties and uses | Periodic Table. (n.d.). https://periodic-table.rsc.org/element/14/silicon

[27] Solution, Z. (2023, November 23). MoSi2 Heating Elements Complete Guide. Solution for Thermal Processing, Material Science | ZYLAB. https://www.zylabsolution.com/mosi2-heating-elements-complete-guide/

[28] Type Special molybdenum disilicide heating elements-Henan Flourishing Energy Saving Service Co.,Ltd. (n.d.).https://www.qs-heatingelements.com/index.php?m=Home&c=case&a=view&case_id=1&nav_id=1

[29] Volders, C., & Reinke, P. (2019). Reaction pathways in the oxidation and pesting of molybdenum disilicide MoSi2 studied with scanning tunneling microscopy and spectroscopy. Surface Science, 681, 134–142. https://doi.org/10.1016/j.susc.2018.11.015

[30] What is Molybdenum—Chemical Properties of Molybdenum—Symbol Mo. (2020, November 21). Periodic Table. https://material-properties.org/Molybdenum-periodic-table-atomic-number-mass-radius-density/

[31] What Is The Electrical Resistivity Of Molybdenum Disilicide? Unlocking Its High-Temperature Heating Power. (n.d.). https://kindle-tech.com/faqs/what-is-the-electrical-resistivity-of-molybdenum-disilicide

[32] 博高村, 高村博, 成田里安, & 成田里安. (2019). MoSi2 heating element and method of manufacturing the same (Patent No. JP6590319B2). https://patents.google.com/patent/JP6590319B2/en

[33] Maxwell, W. A. (1952). *Oxidation-resistance mechanism and other properties of molybdenum disilicide* (NACA RM E52A04). National Advisory Committee for Aeronautics.

[34] Okamoto, H. Mo-Si (Molybdenum-Silicon). J. Phase Equilib. Diffus. 32, 176 (2011). https://doi.org/10.1007/s11669-010-9843-0

[35] Carabat, A. L., Van Der Zwaag, S., & Sloof, W. G. (2015). Creating a Protective Shell for Reactive MoSi2 Particles in High-Temperature Ceramics. Journal of the American Ceramic Society, 98(8), 2609–2616. https://doi.org/10.1111/jace.13625

[36] Kanthal. (2013). *Kanthal Super handbook* (2nd ed.)

[37] admin. (2024, December 10). Tungsten Rod Manufacturing Experts: Exploring the Processes and Innovations in Tungsten Rod Factories. https://www.chemetalusa.com/tungsten-rod-manufacturing-experts-exploring-the-processes-and-innovations-in-tungsten-rod-factories/

[38] Can Tungsten Be Used As A Heating Element? Unlocking Extreme Heat For High-Temperature Applications. (n.d.). https://kindle-tech.com/faqs/can-tungsten-be-used-as-heating-element

[39] Cezairliyan, A. (1971). High-Speed (Subsecond) Measurement of Heat Capacity, Electrical Resistivity, and Thermal Radiation Properties of Niobium in the Range 1500 to 2700 K. Journal of Research of the National Bureau of Standards. Section A, Physics and Chemistry, 75A(6), 565–571. https://doi.org/10.6028/jres.075A.045

[40] Chandrasekharaiah, M. S., Margrave, J. L., & O'Hare, P. A. G. (1993). The Disilicides of Tungsten, Molybdenum, Tantalum, Titanium, Cobalt, and Nickel, and Platinum Monosilicide: A Survey of Their Thermodynamic Properties. Journal of Physical and Chemical Reference Data, 22(6), 1459–1468. https://doi.org/10.1063/1.555922

[41] Choi, Y.-J., Yoon, J.-K., Kim, G.-H., Yoon, W.-Y., Doh, J.-M., & Hong, K.-T. (2017). High temperature isothermal oxidation behavior of NbSi 2 coating at 1000–1450 °C. Corrosion Science, 129, 102–114. https://doi.org/10.1016/j.corsci.2017.10.002

[42] Department, the C. & WebQC.Org. (n.d.). Properties of WSi2. http://www.webqc.org/compound-WSi2-WSi2.html

[43] Guizzetti, G., Marabelli, F., Borghesi, A., Nava, F., Gottlieb, U., & Laborde, O. (1993). Optical and electrical characterization of VSi2 and NbSi2 single crystals. Applied Surface Science, 73, 237–242. https://doi.org/10.1016/0169-4332(93)90172-8

[44] Howard, S., & Howard, S. (n.d.). Development of NbSi2 based alloys.

[45] Luković, J., Zagorac, D., Schön, J. C., Zagorac, J., Jordanov, D., Volkov-Husović, T., & Matović, B. (2017). Tungsten Disilicide (WSi2): Synthesis, Characterization, and Prediction of New Crystal Structures. Zeitschrift Für Anorganische Und Allgemeine Chemie, 643(23), 2088–2094. https://doi.org/10.1002/zaac.201700329

[46] Menon, E. S. K., Mendiratta, M. G., & Dimiduk, D. M. (n.d.). Oxidation behavior of complex niobium based alloys.

[47] Niobium silicide:Crystal Structure,Properties,Uses,Synthesis_Chemicalbook. (n.d.). https://www.chemicalbook.com/article/niobium-silicide-crystal-structure-properties-uses-synthesis.htm

[48] Qedfusion.org/LIB/PROPS/PANOS/w.html. (n.d.). https://qedfusion.org/LIB/PROPS/PANOS/w.html

[49] Rinnerbauer, V., Senkevich, J. J., Joannopoulos, J. D., Soljačić, M., Celanovic, I., Harl, R. R., & Rogers, B. R. (2013). Low emissivity high-temperature tantalum thin film coatings for silicon devices. Journal of Vacuum Science & Technology A: Vacuum, Surfaces, and Films, 31(1), 011501. https://doi.org/10.1116/1.4766295

[50] Solutions, H. C. S. (2020, December 15). Refractory Metals: What Are They? AZoM. https://www.azom.com/article.aspx?ArticleID=19965

[51] Tungsten Mechanical & Physical Properties | EFINEA, Inc. (n.d.). EFINEA Metals. https://www.efineametals.com/refractory-metal-supplier/tungsten/tungsten-properties/

[52] Tungsten: Properties and Applications. (n.d.). https://www.iqsdirectory.com/articles/tungsten/tungsten-metal.html

[53] Wang, S., Pan, Y., Wu, Y., & Lin, Y. (2018). Insight into the electronic and thermodynamic properties of NbSi2 from first-principles calculations. RSC Advances, 8(50), 28693–28699. https://doi.org/10.1039/C8RA04959A

[54] Wang, Z., Wang, Y., Wang, S., Zou, Y., Chen, G., Wen, L., Zhang, G., Zhao, L., Ouyang, J., Jia, D., & Zhou, Y. (2023). High-temperature oxidation resistance and high emissivity of a novel NbSi2/SiO2-Nb2O5/MoSi2-Yb2O3 multilayer coating on Nb substrate for thermal protection. Corrosion Science, 224, 111519. https://doi.org/10.1016/j.corsci.2023.111519

[55] Zhang, S.-L., & Östling, M. (2003). Metal Silicides in CMOS Technology: Past, Present, and Future Trends. Critical Reviews in Solid State and Materials Sciences, 28(1), 1–129. https://doi.org/10.1080/10408430390802431

[56] Zhou, X., Xiao, L., Zha, Y., Xu, J., Fang, J., Deng, G., Xu, S., Liu, S., Zhao, X., & Cai, Z. (2024). Study on the Oxidation Behavior of TiB2-CeO2-Modified (Nb,Mo,Cr,W)Si2 Coating on the Surface of Niobium Alloy. Materials, 17(21), 5244. https://doi.org/10.3390/ma17215244

[57] Kurokawa, K., Shibayama, A., & Kobayashi, A. (2007). Formation of $SiO_2$ scale in high-temperature oxidation of $WSi_2$. Transactions of JWRI, 36(2), 51–55. https://doi.org/10.18910/3766

[58] Al-Aql, A. A. (2003). Electrical resistivity measurements in Ni–Cr alloys. Materials & Design, 24(7), 547–550. https://doi.org/10.1016/S0261-3069(03)00093-1

[59] Ferritic alloys—Kanthal®. (n.d.). https://www.kanthal.com/en/knowledge-hub/heating-material-knowledge/resistance-heating-alloys/ferritic-alloys/

[60] Heanjia. (2025, May 7). FeCrAl Alloy Grades and Properties. Heanjia Super Metals Co. Ltd. https://super-metals.com/fecral-alloy-properties/

[61] Kanthal (alloy). (n.d.). Grokipedia. https://grokipedia.com/page/Kanthal_(alloy)

[62] Milne, J. E., & Giler, R. (n.d.). NICKEL CHROMIUM ALLOYS FOR ELECTRIC RESISTANCE HEATING.

[63] Nickel Chromium Heating Element and Resistance Alloys by JLC Electromet Pvt. Ltd. (n.d.). JLC Electromet Nickel Speciality Alloys. https://www.jlcelectromet.com/nickel-chromium-heating-resistance-alloy-grades.html

[64] Can Graphite Be Used As A Heating Element? Discover Its High-Temp Power In Controlled Environments. (n.d.). https://kindle-tech.com/faqs/can-graphite-be-used-as-a-heating-element

[65] Carbon, E. (2024a, January 9). Thermal Properties of Graphite. East Carbon. https://www.eastcarb.com/thermal-properties-of-graphite/

[66] Carbon, E. (2024b, November 8). 10 Benefits of Graphite Heating Elements in Vacuum Furnaces. East Carbon. https://www.eastcarb.com/graphite-heating-elements-in-vacuum-furnaces/

[67] Chai, P., Wu, Y., & Okamoto, K. (2020). Experimental determination of the emissivity of nuclear graphite at high temperature conditions. Mechanical Engineering Letters, 6(0), 20-00204-20–00204. https://doi.org/10.1299/mel.20-00204

[68] Feinauer, A., Jakkala, S. G., Vengadesan, S., Petrasch, J., & Benard, A. (2025). kW-scale graphite heater for extreme temperature applications. Applied Thermal Engineering, 274, 126398. https://doi.org/10.1016/j.applthermaleng.2025.126398

[69] Globar® heating elements—Kanthal®. (n.d.). https://www.kanthal.com/en/products/furnace-products/electric-heating-elements/silicon-carbide-heating-elements/#tab-characteristics

[70] Home, Us, A., Lines, P., Certifications, Center, M. R., Grades, A. F. B. M. A. B., Gallery, Sitemap, & Us, C. (n.d.). Silicon Carbide Material Properties. Imetra, Inc. https://www.imetra.com/silicon-carbide-material-properties/

[71] [Hot Item] Precision Graphite Heater for High-Temperature Applications Durable Graphite Heating Element with Superior Corrosion Resistance. (n.d.). Made-in-China.Com. https://ttwymachinery.en.made-in-china.com/product/rxQRkYvVTeUm/China-Precision-Graphite-Heater-for-High-Temperature-Applications-Durable-Graphite-Heating-Element-with-Superior-Corrosion-Resistance.html

[72] Jiang, J., Wang, S., & Li, W. (2016). Preparation and Characterization of UltraHigh-Temperature Ternary Ceramics Ta4 HfC5. Journal of the American Ceramic Society, 99(10), 3198–3201. https://doi.org/10.1111/jace.14436

[73] Pelissier, K., Chartier, T., & Laurent, J. M. (1998a). Silicon carbide heating elements. Ceramics International, 24(5), 371–377. https://doi.org/10.1016/S0272-8842(97)00024-2

[74] Savvatimskiy, A. I., Onufriev, S. V., Valyano, G. V., Nepapushev, A. A., & Moskovskikh, D. O. (2022). Thermophysical properties of tantalum carbide (TaC) within 2000–5500 K temperature range. Ceramics International, 48(14), 19655–19661. https://doi.org/10.1016/j.ceramint.2022.03.102

[75] Schönfeld, K., Trache, M., & Martin, H. -P. (2021). Electrical performance of ZrC ceramics. Materialwissenschaft Und Werkstofftechnik, 52(12), 1338–1345. https://doi.org/10.1002/mawe.202100097

[76] Silicon Carbide Electric Heating Elements | Sic Heaters. (n.d.). https://www.rubi-resistencias.com/en/silicon-carbide-heater.html

[77] Silicon Carbide Heating Elements. (n.d.). MHI-INC. https://mhi-inc.com/silicon-carbide-heating-elements/

[78] Tungsten Carbide Properties. (n.d.). https://carbideprocessors.com/pages/carbide-parts/tungsten-carbide-properties.html

[79] Tungsten Carbide (WC): MakeItFrom.com. (n.d.). https://www.makeitfrom.com/material-properties/Tungsten-Carbide-WC

[80] What Are The Advantages And Disadvantages Of Graphite? Mastering High-Temperature Performance Vs. Contamination Risk. (n.d.). https://kindle-tech.com/faqs/what-are-the-advantages-and-disadvantages-of-graphite

[81] Fraunhofer IKTS. (n.d.). Zirconium carbide components for high-temperature processes: Powerful, reliable and cost-efficient.

[82] Inoue, R., Arai, Y., Kubota, Y., Kogo, Y., & Goto, K. (2018). Oxidation of ZrB2 and its composites: A review. Journal of Materials Science, 53(21), 14885–14906. https://doi.org/10.1007/s10853-018-2601-0

[83] Mallik, M., Kailath, A. J., Ray, K. K., & Mitra, R. (2012). Electrical and thermophysical properties of ZrB2 and HfB2 based composites. Journal of the European Ceramic Society, 32(10), 2545–2555. https://doi.org/10.1016/j.jeurceramsoc.2012.02.013

[84] Nakamori, F., Ohishi, Y., Muta, H., Kurosaki, K., Fukumoto, K., & Yamanaka, S. (2015). Mechanical and thermal properties of bulk ZrB2. Journal of Nuclear Materials, 467, 612–617. https://doi.org/10.1016/j.jnucmat.2015.10.024

[85] Zimmermann, J. W., Hilmas, G. E., Fahrenholtz, W. G., Dinwiddie, R. B., Porter, W. D., & Wang, H. (2008). Thermophysical Properties of ZrB2 and ZrB2 –SiC Ceramics. Journal of the American Ceramic Society, 91(5), 1405–1411. https://doi.org/10.1111/j.1551-2916.2008.02268.x

[86] Oberg, A., Kassman, A., Andre, B., Wiklund, U., Lindquist, M., Lewin, E., … Ljungcrantz, H. (2010). Conductive nanocomposite ceramics as tribological and electrical contact materials. European Physical Journal, 49(2). https://doi.org/10.1051/epjap/2009122

[87] Tsakiropoulos, P. (2023). A Perspective of the Design and Development of Metallic Ultra-High Temperature Materials: Refractory Metal Intermetallic Composites, Refractory Complex Concentrated Alloys and Refractory High Entropy Alloys. Alloys, 2(3), 184-212. https://doi.org/10.3390/alloys2030014

[88] Thermcraft, Inc. (2016). *Electrical resistance heating elements: An overview*. Thermcraft, Inc.

[89] Globar® heating elements—Kanthal®. (n.d.). https://www.kanthal.com/en/products/furnace-products/electric-heating-elements/silicon-carbide-heating-elements/#tab-characteristics

[90] Kanthal. (2018). Resistance heating alloys and systems for industrial furnaces (Product overview). Sandvik Materials Technology.

[91] Canarslan, N. S., & Canarslan, Ö. S. (2019). Combustion synthesis of SiC-MoSi2-Al2O3 composites. Ceramics International, 45(12), 14505–14509. https://doi.org/10.1016/j.ceramint.2019.04.125

[92] Carabat, A. L., Van Der Zwaag, S., & Sloof, W. G. (2015). Creating a Protective Shell for Reactive MoSi2 Particles in High-Temperature Ceramics. Journal of the American Ceramic Society, 98(8), 2609–2616. https://doi.org/10.1111/jace.13625

[93] Eichler, J., & Lesniak, C. (2008). Boron nitride (BN) and BN composites for high temperature applications. Journal of the European Ceramic Society, 28(5), 1105–1109. https://doi.org/10.1016/j.jeurceramsoc.2007.09.005

[94] Huang, J.-B., & Zhang, G.-H. (2023). Microstructures and performances of pressureless sintered MoSi2-Al2O3 composites. Corrosion Science, 224, 111514. https://doi.org/10.1016/j.corsci.2023.111514

[95] Matsuo S., & Kubo T. (1964). Sintering in the Binary System MoSi2-WSi2. Journal of the Ceramic Association, Japan, 72(821), 111–117. https://doi.org/10.2109/jcersj1950.72.821_111

[96] Shao, G., Wu, X., Cui, S., Shen, X., Kong, Y., Lu, Y., Jiao, C., & Jiao, J. (2016). High emissivity MoSi2–ZrO2–borosilicate glass multiphase coating with SiB6 addition for fibrous ZrO2 ceramic. Ceramics International, 42(7), 8140–8150. https://doi.org/10.1016/j.ceramint.2016.02.020

[97] Vasudévan, A. K., & Petrovic, J. J. (1992). A comparative overview of molybdenum disilicide composites. Materials Science and Engineering: A, Proceedings of the First High Temperature Structural Silicides Workshop, 155(1), 1–17. https://doi.org/10.1016/0921-5093(92)90308-N

[98] Xiao, L., Zhou, X., Wang, Y., Pu, R., Zhao, G., Shen, Z., Huang, Y., Liu, S., Cai, Z., & Zhao, X. (2020). Formation and oxidation behavior of Ce-modified MoSi2-NbSi2 coating on niobium alloy. Corrosion Science, 173, 108751. https://doi.org/10.1016/j.corsci.2020.108751

[99] Zhang, Y., Ni, W., & Li, Y. (2018). Effect of siliconizing temperature on microstructure and phase constitution of Mo–MoSi2 functionally graded materials. Ceramics International, 44(10), 11166–11171. https://doi.org/10.1016/j.ceramint.2018.03.136

[100] Zhang, Y., Zhou, X., Cheng, H., Geng, Z., & Li, W. (2023). Fabrication and Oxidation Resistance of a Novel MoSi2-ZrB2-Based Coating on Mo-Based Alloy. Materials, 16(16), 5634. https://doi.org/10.3390/ma16165634

[101] Sun, S. P., Li, X. P., Zhang, Y., Wang, H. J., Yu, Y., Jiang, Y., & Yi, D. Q. (2017). Prediction of the mechanical properties of MoSi2 doped with Cr, Nb and W from first-principles calculations. Journal of Alloys and Compounds, 714, 459–466. https://doi.org/10.1016/j.jallcom.2017.04.271

[102] Aguirre, T. G., Lamm, B. W., Cramer, C. L., & Mitchell, D. J. (2022). Zirconium-diboride silicon-carbide composites: A review. Ceramics International, 48(6), 7344–7361. https://doi.org/10.1016/j.ceramint.2021.11.314

[103] Ghadami, S., Taheri-Nassaj, E., Baharvandi, H. R., & Ghadami, F. (2021). Improvement of mechanical properties of HfB2-based composites by incorporating in situ SiC reinforcement through pressureless sintering. Scientific Reports, 11(1), 9835. https://doi.org/10.1038/s41598-021-88566-0

[104] Gupta, S., Mahapatra, M. K., & Singh, P. (2013). Phase transformation, thermal expansion and electrical conductivity of lanthanum chromite. Materials Research Bulletin, 48(9), 3262–3267. https://doi.org/10.1016/j.materresbull.2013.05.032

[105] He, R., Fang, D., Wang, P., Zhang, X., & Zhang, R. (2014). Electrical properties of ZrB2–SiC ceramics with potential for heating element applications. Ceramics International, 40(7), 9549–9553. https://doi.org/10.1016/j.ceramint.2014.02.029

[106] Mallik, M., Kailath, A. J., Ray, K. K., & Mitra, R. (2012). Electrical and thermophysical properties of ZrB2 and HfB2 based composites. Journal of the European Ceramic Society, 32(10), 2545–2555. https://doi.org/10.1016/j.jeurceramsoc.2012.02.013

[107] Mohammadzadeh, B., Jung, S., Lee, T. H., Le, Q. V., Cha, J. H., Jang, H. W., Lee, S.-H., Kang, J., & Shokouhimehr, M. (2020). Manufacturing ZrB2–SiC–TaC Composite: Potential Application for Aircraft Wing Assessed by Frequency Analysis through Finite Element Model. Materials, 13(10), 2213. https://doi.org/10.3390/ma13102213

[108] Monteverde, F., & Bellosi, A. (2004). Microstructure and Properties of an HfB2 -SiC Composite for Ultra High Temperature Applications. Advanced Engineering Materials, 6(5), 331–336. https://doi.org/10.1002/adem.200400016

[109] Song, S. T., Pan, H. Y., & Yang, B. (n.d.). Synthesis, Properties and Application of High Conductive LaCr03-Based Ceramic Materials.

[110] Carrillo-Heian, E. M., Carpenter, R. D., Paulino, G. H., Gibeling, J. C., & Munir, Z. A. (2001). Dense Layered Molybdenum Disilicide–Silicon Carbide Functionally Graded Composites Formed by Field-Activated Synthesis. Journal of the American Ceramic Society, 84(5), 962–968. https://doi.org/10.1111/j.1151-2916.2001.tb00775.x

[111] Zheng, J.-Q., Chen, J., Zhang, B.-H., Liu, X.-J., Chen, Z.-M., Wu, H.-B., & Huang, Z.-R. (2019). Electrical percolation and infrared emissivity of pressureless sintered SiC-MoSi2 composites tailored by sintering temperature. Journal of the European Ceramic Society, 39(14), 3981–3987. https://doi.org/10.1016/j.jeurceramsoc.2019.05.019

[112] Tapia-López, J., Pech-Canul, M. I., & García, H. M. (2023). Processing, microstructure, properties, and applications of MoSi2-containing composites: A review. Frontiers in Materials, 10. https://doi.org/10.3389/fmats.2023.1165245

[113] Percolation Threshold of the Thermal, Electrical and Optical Properties of Carbonyl-Iron Microcomposites - Scientific Figure on ResearchGate. Available from: https://www.researchgate.net/figure/Schematic-diagram-showing-the-percolation-behavior-in-an-insulating-matrix-conductive_fig1_349320083